Stiffness-tunable biomaterials to explore biophysical cues arising within contracting collagen microtissues

Carley Ort
Department of Chemical Engineering
McGill University
Montréal, QC, Canada

November 11, 2021

A thesis submitted to McGill University in partial fulfillment of the requirements for the degree of Doctor of Philosophy

Table of Contents

Chapter 4: Local mechanical profiling of collagen microtissue contraction using integrated biomaterial sensors……………………………………………………………………..66

Abstract

The mechanical microenvironment within a tissue drives fundamental cell behaviours including cell survival, proliferation, and migration, that ultimately direct healthy tissue homeostasis or pathologic progression. Cells sense a variety of biophysical cues, such as externally applied strain, extracellular stiffness, and surface geometry; all of which regulate more complex processes such as cellular contraction, a tissue relevant phenomenon important in both development and disease. Local cell contraction provides a set of cell-scale mechanical cues, including tissue strain and stiffness; but how these local mechanical microenvironments drive global tissue contraction is undefined. In this work, I (1) develop and characterize a stiffness-tunable microtissue bioprinting culture platform for increased-throughput study of mechanobiological contraction, (2) develop a technique to modify microtissue geometry, to study how tissue free boundary area affects global tissue contraction, and (3) investigate how initial tissue stiffness impacts the changing local strain, local stiffness, and local forces within contracting microtissues. Stiffness impacted cell morphology and high stiffness slowed global tissue contraction rates. High stiffness was not able to stimulate contraction as well as soluble molecule stimulants, demonstrating that this mechanical signal may not be a driving cue of 3D tissue contraction. Tissue geometry affected contraction, where high tissue free boundary area increased global strain rates. This suggests that cell phenotypes at the tissue perimeter, including the organized F-actin superstructure sheet encasing the microtissue, are crucial elements of tissue contraction. Initial tissue stiffness surprisingly did not impact local stiffness during contraction, suggesting that matrix properties are insignificant contributors to local stiffness following cell seeding. Instead, live, contractile cells appeared to dominate local tissue stiffness. Increasing baseline stiffness decreased local strain and local force generation within contracting microtissues. Moreover, local, cell-induced forces did not depend on real-time local stiffness. Instead, forces arising within tissues correlated well with local tissue strain, independent of initial stiffness, suggesting that tissue strain rather than tissue stiffness may be the dominant driver of 3D contraction. Finally, this work is discussed within the context of focal adhesion formation and cell spreading. The work conducted here is supported by recent studies demonstrating that microenvironment stiffness regulates ligand recruitment, driving focal adhesion formation and downstream contractile cell behaviours such as cell spread and F-actin structure formation. This suggests that local strain is necessary for focal adhesion formation within a 3D fibrous matrix, and is therefore a crucial mechanical cue that arises during tissue contraction. This work hence provides a robust platform for mechanical analysis of tissue contraction, and highlights critical signalling cues that drive niche, local microenvironments, thereby impacting global tissue contraction.

Résumé

Le microenvironnement mécanique au sein d'un tissu entraîne des comportements cellulaires fondamentaux, notamment la survie, la prolifération et la migration cellulaires, qui dirigent finalement l'homéostasie des tissus sains ou la progression pathologique. Les cellules détectent une variété d'indices biophysiques, tels que la contrainte appliquée de l'extérieur, la rigidité extracellulaire et la géométrie de la surface ; qui régulent tous des processus plus complexes tels que la contraction cellulaire, un phénomène important pour le développement et la maladie. La contraction cellulaire locale fournit un ensemble d'indices mécaniques à l'échelle cellulaire, y compris la tension et la rigidité des tissus ; mais la façon dont ces microenvironnements mécaniques locaux entraînent la contraction globale des tissus n'est pas définie. Dans ce travail, je (1) développe et caractérise une plate-forme de culture de bio-impression de microtissus à rigidité ajustable pour une étude à débit accru de la contraction mécanobiologique, (2) développe une technique pour modifier la géométrie des microtissus, pour étudier comment la zone de frontière libre des tissus affecte le tissu global contraction, et (3) étudier l'impact de la rigidité tissulaire initiale sur la déformation locale changeante, la rigidité locale et les forces locales au sein des microtissus en contraction. La rigidité a eu un impact sur la morphologie cellulaire et une rigidité élevée a ralenti les taux de contraction globale des tissus. Une rigidité élevée n'a pas été en mesure de stimuler la contraction aussi bien que les stimulants de molécules solubles, démontrant que ce signal mécanique peut ne pas être un indice moteur de la contraction des tissus 3D. La géométrie des tissus a affecté la contraction, où une zone de frontière libre élevée des tissus a augmenté les taux de déformation globaux. Cela suggère que les phénotypes cellulaires au périmètre du tissu, y compris la feuille de superstructure organisée d'actine F enveloppant le microtissu, sont des éléments cruciaux de la contraction tissulaire. La rigidité tissulaire initiale n'a étonnamment pas eu d'impact sur la rigidité locale pendant la contraction, ce qui suggère que les propriétés de la matrice sont des contributeurs insignifiants à la rigidité locale après l'ensemencement cellulaire. Au lieu de cela, les cellules contractiles vivantes semblaient dominer la rigidité des tissus locaux. L'augmentation de la rigidité de base a diminué la tension locale et la génération de force locale dans les microtissus en contraction. De plus, les forces locales induites par les cellules ne dépendaient pas de la rigidité locale en temps réel. Au lieu de cela, les forces apparaissant dans les tissus étaient bien corrélées avec la tension tissulaire locale, indépendamment de la rigidité initiale, ce qui suggère que la tension tissulaire plutôt que la rigidité tissulaire peut être le moteur dominant de la contraction 3D. Enfin, ce travail est discuté dans le contexte de la formation d'adhérence focale et de la propagation cellulaire. Les travaux menés ici sont soutenus par des études récentes démontrant que la rigidité du microenvironnement régule le recrutement de ligands, entraînant la formation d'adhérence focale et les comportements cellulaires contractiles en aval tels que la propagation cellulaire et la formation de la structure F-actine. Cela suggère que la contrainte locale est nécessaire pour la formation d'adhérence focale au sein d'une matrice fibreuse 3D, et est donc un indice mécanique crucial qui survient lors de la contraction des tissus. Ce travail fournit donc une plate-forme robuste pour l'analyse mécanique de la contraction des tissus et met en évidence les signaux de signalisation critiques qui entraînent des microenvironnements locaux de niche, ayant ainsi un impact sur la contraction globale des tissus.

Acknowledgements

This life chapter has been beautifully imperfect, with equal parts growth and hardship. Core personal characteristics, such as my life perspective, self confidence, and critical thinking skills have undergone valuable, yet dramatic reconstruction during these 5 years. I would not be standing at the finish line as the same person without these monumental individuals, who shaped my experience here and imprinted on my memory forever.

The most pivotally influential person to me during this adventure has been my supervisor Chris. Throughout my entire PhD, he has always known exactly what I needed to hear to achieve the most personal and academic growth. He did this by showing an artistic balance of sincerely understanding qualities on one hand, with subtly expressed, yet demanding expectations on the other, that together pushed me to reach my maximal potential. He was always there for me when I needed academic, or at times, emotional support, and I felt genuinely cared about as a student and human being. Whether he knew the extent of this or not, he navigated me through the empowering life lessons of (1) speaking up to acknowledge and defend myself, (2) finding internal validation, and (3) carefully communicating exactly what I mean. These learning experiences have changed my self confidence forever. Chris will, without a doubt, be written down as one of the most influential people of my entire life.

Another superstar to mention is Rachel Mot. This good-hearted girl became my closest friend in the city, and absolutely a friend that I now hold for life. She added so much hype and adventure to my otherwise research dominated weeks and I am so lucky to have crossed life paths with her.

A special acknowledgement goes to my epic office mates in 7210: Sonya, Christina, Julia, and briefly Nathália. These girls are a big reason that my day-to-day experience was warm and smiley. Sonya helped support my confidence when I first entered the lab and found myself drowning. She was my shining light in this challenging new world, and acted as my strongest lab ally. We also had plenty of fun outside of the lab with miniature painting, DnD, and dinner dates with Shawn. Christina is a magical human being. She is extremely helpful, intelligent, and caring, as well as an encouraging cheerleader with an attentive listening ear.

Our entire lab team is a neat design of stellar individuals and each person who I have shared this lab experience with is memorable. Gabe is full of energy and presence. It was always fun to discuss controversial happenings with her during a pipetting sesh. Ray has an infectiously chill vibe and is only ever positive and friendly. Steph is fiercely supportive you if you truly need her, and I grew to find her "no bullsh*%+" attitude wonderfully refreshing. Wontae played an integral role in my critical thinking development and worked with me for the two biggest papers in this thesis. Her mind is both immaculate and creative, and she was always willing to provide clear, concise help. Nik (the first one XD) has so much enthusiasm for everyone else's project that a person's heart can't help but smile to see it. Whenever I had to work late into the evening, Nik would be right there with me. We often dove into long life chats while listening to techno. Nick Lin has a sense of humour and authenticity that I will never forget. Successfully visualizing the pore structure of my microgels under SEM with him was one of the most tangibly exciting moments of my wet lab experience. Camille, Karthick, Sanya, Chen, James, Ben, Nick W, Nik S, Scott, Lucas, Arvind, Lisa, Sarah, Zhenwei, Vickie, Kim, Joann, Lidan, Sam, and Kirk are all very special people who I share fond memories with in the good old Moraes Lab.

Finally, I want to *super*highlight my family: Sarah, Andrew, Jeff, Andrea, Doug, Mom, Dad, Sheila, and Nicole. Although not as directly involved in my PhD experience as the community of people above, the special individuals here are my long-term, consistent rocks of comfort and love. They are my "forever people" regardless of the life chapter I find myself in.

Contributions to original knowledge

1. I optimized and characterized an increased throughput microtissue culture platform capable of controlling matrix stiffness between ~ 0.5- 2.5 kPa, representative of healthy to diseased connective tissue. My interpenetrating matrix networks of collagen-1 and alginate maintained physiological remodel-ability and contractibility following stiffening, and the aqueous two-phase system used for bioprinting allowed automated production of 1 μL tissue droplets, as opposed to the 10's of μL that typically require complex handling for standard 3D mechanical culture models. My innovation therefore provides a robust mechanical platform to explore contractile state-in-a-plate.

2. As proof-of-principle for broad utility, I applied this novel mechanical platform to two highly common and distinctly different culture assays: chemotherapeutic screening and fibroblast tissue contraction. With this, I discovered a biphasic relationship between matrix stiffness and chemotherapeutic efficacy, highlighting matrix stiffness and strain as two opposing cues that increased stiffness provides within a fibrous microenvironment. Additionally, I determined the individual contributions of matrix stiffness and soluble contractile stimulants to tissue contraction rates, recognizing that high stiffness promotes F-actin contractile structures, yet is not sufficient to induce global tissue contraction.

3. I engineered a thermally-based technique to tune microgel geometry and characterized the spatial contractile patterns that arise during tissue contraction, with prominent strains and cell organization at the tissue edge. Building upon this, I then identified free boundary area at the tissue perimeter as a crucial variable in tissue contraction assays, as high free boundary area increased global strains. This insight demonstrates the variability between contraction studies, which are commonly used and compared, and highlights the need for careful consideration of free boundary area before drawing conclusions.

4. I defined the local mechanics arising within dynamically contracting tissues and illustrated that high matrix stiffness is not a dominant driver of tissue contraction. I

showed surprisingly high stiffness in cell-seeded tissues, that did not increase as the tissue contracted 90% of its area, suggesting that mechanically active cells dominate tissue stiffness: a parameter currently attributed to matrix properties. I demonstrated lower local forces within stiffened matrices, with local forces correlating impressively with local strains, independent of initial tissue stiffness. This finding suggests that strain, rather than stiffness, may be the dominant signalling cue responsible for driving cell-induced forces within a fibrous tissue microenvironment, contributing further evidence to support this paradigm shift currently taking place in the field.

Contribution of authors

The work presented in this thesis was a collaboration between myself and key individuals who provided indispensable contributions to the research and ideas. Individual contributions of co-authors pertaining to this thesis are outlined below.

Chapter 1: Disentangling the fibrous microenvironment: designer culture models for improved drug discovery

I conceptualized, organized, and independently wrote the manuscript, with the exception of section *2.1: Microstructural features of the fibrous ECM*, to which I contributed a minor portion of the writing. I coordinated the first complete draft of the manuscript, produced all figures and was responsible for final editing of the manuscript, including the response to reviewer comments and completing the final proofreading and editorial requirements.

Wontae Lee assisted in the organization of the manuscript. She contributed to the writing of section *2.1: Microstructural features of the fibrous ECM*, and also contributed to editing the manuscript.

Nikita Kalashnikov assisted in the organization of the manuscript. He contributed to the writing of section *2.1: Microstructural features of the fibrous ECM*, provided expertise on section *1.2.2: Viscoelasticity*, and helped edit the manuscript.

Christopher Moraes assisted in the conceptualization and organization of the manuscript, and contributed to the editing. He was also responsible for providing the funding to support the manuscript.

Chapter 2: Bioprintable, stiffness-tunable collagen-alginate microgels for increased throughput 3D cell culture studies.

I lead the critical thinking and discussion surrounding the data presented in this chapter and helped conceptualize the final manuscript. I troubleshot and optimized biomaterial recipes and printing protocols, thereby contributing to the development of the methodology. I conducted the investigation of all experiments and analyzed all data, with the exception of the twisting magnetic cytometry measurements and analysis. I independently wrote the manuscript, produced all figures, and was responsible for final editing of the manuscript, including the response to reviewer comments and completing the final proofreading and editorial requirements.

Yimai Chen contributed to this chapter by engineering the biomaterial recipes and printing protocols, thereby developing the methodology. She also provided a significant amount of unpublished data to initiate the project.

Ajinkya Ghagre conducted all twisting magnetic cytometry measurements and analysis, providing the mechanical information surrounding biomaterial storage moduli, loss moduli, complex moduli, and phase angle.

Allen Ehrlicher supervised Ajinkya Ghagre, and provided access to the magnetic twisting cytometry equipment, along with critical comments during the manuscript writing process.

Christopher Moraes conceptualized the project, supervised all processes, managed and co-ordinated individual responsibilities, provided the resources and funding for the project, added critical thinking insights to all data presented within, and contributed to editing the manuscript.

Chapter 3: Free boundary area of collagen microtissues affects contraction strain rate.
I lead the critical thinking and discussion of the data presented in this chapter and helped conceptualize the overall project and the manuscript. I discovered the thermal-based printing technique, thereby developing the methodology. I conducted the investigation of all experiments and analyzed all data, with the exception of the local strain rate data in Figures 3.1E and 3.3. For this data, I instead was responsible for training Kimberly Seaman on tissue printing protocols and contraction imaging. I independently wrote the manuscript, produced all figures, and was responsible for editing the manuscript.

Wontae Lee produced the fiducial hydrogel markers, thereby contributing to the methodology, and trained Kimberly Seaman on the imaging methods for them.

Kimberly Seaman conducted the investigation and analyzed the data for determining local strain rate in Figures 3.1E and 3.3.

Christopher Moraes conceptualized the project, supervised all processes, managed and co-ordinated individual responsibilities, provided the resources and funding for the project, added critical thinking insights to all data presented within, and contributed to editing the manuscript.

Chapter 4: Local mechanical profiling of collagen microtissue contraction using integrated biomaterial sensors.

I lead the critical thinking and discussion of local stiffness and strain data presented in this chapter and helped conceptualize the overall project and manuscript. I also took a combined leading role together with Wontae Lee for all local force data seen here. I conducted the investigation of most experiments for this chapter. This includes all of Figures 4.4, 4.5, 4.6, 4.7, 4.11, 4.12, and 4.14. It also includes the majority of Figures 4.3 (with the exception of F,G), 4.8 (with the exception of E,F), and 4.13 (with the exception of D,E). I also analyzed much of the data, including all of Figures 4.4, 4.12, 4.13, and 4.14, along with Figures 4.1D,F, 4.6B, and 4.8D. I contributed to the remaining data by training both Kimberly Seaman and Zizhou Xiang on tissue printing protocols and contraction imaging. I took a leading role in the final organization of the chapter and figure production, independently wrote the manuscript, and was responsible for the editing.

Wontae Lee lead the critical thinking and discussion, together with me, for all local force data in this chapter, and helped conceptualize the manuscript. She also provided the MSGs, took a shared leading role in the organization of much of the chapter, analyzed the data in Figure 4.1H,I, contributed to figure production, and was responsible for training Kimberly Seaman on force sensing bead measurement and analysis. Modified versions of Figures 4.1, 4.3, 4.8, and 4.15 have been included in her PhD thesis, along with similar discussions of the work.

Kimberly Seaman conducted the investigation of much of the local force data, including all of the data in Figures 4.1, 4.2, and 4.3FG. She also analyzed all of the local force data in this chapter: all of Figures 4.2, 4.9, 4.10, 4.15, most of Figure 4.1, and Figures 4.3F,G, 4.8E,F and 4.13D,E.

Stephanie Mok contributed to the local stiffness data in this chapter by training me on the collection of the data, conducting the investigation for the cell-free stiffness measurements in Figure 4.6C, and analyzing all of the local stiffness data in this chapter: Figures 4.6C, 4.7, 4.8G, 4.11, and 4.12. She also contributed to the discussion of the stiffness relevant sections of this chapter.

Zizhou Xiang conducted the investigation of the experiment comparing local forces between initially soft and initially stiff tissues, that is presented in Figures 4.8E,F, 4.9, 4.10, 4.13D,E, and 4.15.

Christopher Moraes conceptualized the project, supervised all processes, managed and co-ordinated individual responsibilities, provided the resources and funding for the project, added critical thinking insights to all data presented within, and contributed to editing the manuscript.

Chapter 5: Comprehensive Discussion

I conceptualized, organized, wrote, and edited the chapter, producing both figures.

Christopher Moraes contributed to organizing the chapter as well as the editing.

Chapter 6: Concluding Remarks

I conceptualized, organized, wrote, and edited the chapter, with feedback from Christopher Moraes.

Thesis Introduction

General background

Many cell types contain intracellular contractile machinery, allowing them to apply force onto the surrounding extracellular matrix (ECM), straining and rearranging the matrix fibers [1]. This process of ECM contraction is critical for embryonic developmental morphogenesis [2] and adult tissue homeostasis [3]. Fibroblasts specifically, are key cells responsible for connective tissue homeostasis [3]. Wound repair depends on regulated fibroblast contraction to re-achieve tissue stability [4] and dysregulated fibroblast contraction is a principal component of tissue fibrosis and tumour progression [5] [6]. Understanding the fundamental cues that regulate fibroblast matrix contraction may therefore lead to improved culture models and disease therapies.

The mechanical microenvironment has arisen as a strong director of important cell behaviours. Tissue stiffness and geometry both regulate mechanical stress, or stress gradients in the ECM [7] [8]. Although the instructive signal responsible for cell response is unknown due to intrinsically tied stress and strain, tissue stiffness and interfacial geometry both drive contractile related cell phenotypes, such as stress fiber formation and smooth muscle actin expression [9] [10]. Most studies investigating the relationship between cell contraction with these two mechanical cues are conducted on flat, non-fibrous substrates, incapable of the dynamic tissue remodelling that occurs in human tissues. How tissue free boundary area and initial tissue stiffness modulate local cell phenotypes that then drive global tissue contraction is undefined.

Objectives

Central objective: define the local biophysical cues crucially involved in global tissue contraction.

1. Design and characterize a robust 3D tissue contraction platform capable of tuning initial tissue stiffness.
2. Modify the platform to explore how tissue geometry influences global tissue strain during contraction.
3. Characterize the importance of initial tissue stiffness in driving the local mechanics of stress, strain, and stiffness within a dynamically contracting tissue.

Thesis organization

This thesis is written in manuscript format, containing the following 7 chapters:

Chapter 1 provides a comprehensive literature review that deconstructs the major architectural and resulting mechanical cues that cells receive within a 3D, fibrous extracellular matrix, along with how these cues drive specific cellular functions, and engineering design strategies to independently modify these cues. The review is written within the scope of improved drug discovery: a potential application of the robust contraction platform developed here, highlighting a broadened utility of this engineered system.

Chapter 2 addresses the first thesis objective by developing a stiffness-tunable tissue contraction platform and broadly investigates how initial tissue stiffness regulates contraction relevant phenotypes of cell spread area, F-actin structure, and global tissue strain.

Chapter 3 addresses the second thesis objective by incorporating a novel thermal-based technique into the platform to tune tissue geometry, investigating how free boundary area influences global tissue strain during contraction.

Chapter 4 addresses the third thesis objective by integrating two different cell-sized mechanical sensors, enabling local stress and stiffness measurements during tissue contraction. Baseline tissue stiffness is tuned to uncover its role in both local force generation and local stiffness during contraction. Local forces are then compared to local strains, visualized by the local gathering of small, inert fluorescent particles. This chapter therefore characterizes how initial tissue stiffness controls the arising local stresses, stiffness, and strains within a dynamically contracting tissue.

Chapter 5 provides a unified discussion that focuses on focal adhesion formation and cell spread to explain cell phenotypes seen across each research chapter.

Chapter 6 closes the thesis with an overarching summary and conclusions illustrating the novel scientific contributions made towards *in-vitro* culture design engineering and fundamental cell-ECM biophysics.

Chapter 7 lists the complete thesis references.

List of Figures

List of Tables

Chapter 1

Background and Literature Review

Disentangling the fibrous microenvironment: designer culture models for improved drug discovery

The following chapter provides a comprehensive description of the major architectural and resulting mechanical cues within a fibrous tissue microenvironment that drive fundamental and disease relevant cell behaviours. This provides the necessary background needed before introducing the mechanically tunable fibrous culture platform engineered in this thesis. It then highlights successful engineering strategies to independently tune these signalling parameters, providing an overview of the strengths and weaknesses of alternative mechanical culture models. Finally, to demonstrate the value of the novel mechanical culture platform engineered here, this chapter is written from the perspective of high throughput screening: a strong future application of this work that addresses a critical need in both academic and industrial drug development. This work is published in Expert Opinion on Drug Discovery, and is reproduced with permission from Taylor & Francis. Citation information for this work is as follows: Ort C, Lee W, Kalashnikov N, Moraes C. Disentangling the fibrous microenvironment: designer culture models for improved drug discovery. Expert Opin Drug Discov. 2021 Feb;16(2):159-171. doi: 10.1080/17460441.2020.1822815.

Abstract

Introduction: Standard high-throughput screening (HTS) assays rarely identify clinically viable 'hits', likely because cells do not experience physiologically realistic culture conditions. The biophysical nature of the extracellular matrix has emerged as a critical driver of cell function and response and recreating these factors could be critically important in streamlining the drug discovery pipeline.

Areas covered: The authors review recent design strategies to understand and manipulate biophysical features of three-dimensional fibrous tissues. The effects of architectural parameters of the extracellular matrix and their resulting mechanical behaviors are deconstructed; and their individual and combined impact on cell behavior is examined. The authors then illustrate the potential impact of these physical features on designing next-generation platforms to identify drugs effective against breast cancer.

Expert opinion: Progression toward increased culture complexity must be balanced against the demanding technical requirements for high-throughput screening; and strategies to identify the minimal set of microenvironmental parameters needed to recreate disease-relevant responses must be specifically tailored to the disease stage and organ system being studied. Although challenging, this can be achieved through integrative and multidisciplinary technologies that span microfabrication, cell biology, and tissue engineering.

1.1 Introduction

Initially promising hits in high-throughput screening (HTS) drug assays that turn out to be "dead-ends" create costly inefficiencies in the drug development pipeline. These expenses must be absorbed by successful therapeutics. Hence, it cost an average of $648 million USD to develop a single new drug in 2017 [11], and these numbers are projected to continue increasing. Since 90% of drugs fail phase I clinical trials [12], an ability to identify dead-ends prior to expensive testing would significantly reduce the average costs of pursuing the most promising therapies.

Cells exist in extraordinarily complex environments, where they reside within a meshwork of supporting fibrous proteins. This extracellular matrix (ECM) both supports and drives cellular organization into complex structures, and relays a variety of biochemical and biophysical signals to regulate cellular response. The fibrous ECM meshwork can consist of ~100 different fibrous proteoglycans, polysaccharides and proteins (the most abundant of which include Type I collagen and elastin), and a further ~100 ECM associated proteins such as soluble factors that bind to this mesh [13]. The biochemical complexity of the ECM plays a critical role in driving cellular response [14] and has been shown to affect therapeutic response [15]. These features have been extensively reviewed elsewhere [16] [17] [18] [19]. More recently however, *biophysical* signals provided by the fibrous microenvironment have emerged as pivotal regulators of cell function. Changes in biophysical properties such as tissue architecture and mechanics are associated with disease progression in a wide variety of diseases including cancer, fibrotic disease, and osteoarthritis [17] [20] [21] [22], but the hard, flat, plastic surfaces of conventional drug screens do not capture this complexity. Thus, it is not surprising that cells do not respond to candidate therapeutics in a realistic manner. Developing biomimetic, disease-specific, and precisely-defined environments should therefore improve the translational potential of these assays. For example, simply including protein fibers in drug screening culture models significantly impacts observed drug efficacy [23] [24] [25] [26] [27]. Methods to recreate tissue complexity and architecture that occur at various stages of disease progression may therefore be a viable strategy in streamlining the drug development pipeline.

Although promising, this general approach presents two contrasting challenges. First, how do we decide which set of “microenvironmental” features are both necessary and sufficient to produce translational results in HTS platforms? Second, how do we implement these features in HTS drug screening systems? While the idealistic design strategy would be to recreate the entire tissue, current technologies limit our capacity to replicate this immense complexity, particularly for HTS applications that require robustness for intensive scale-up. Furthermore, tissue characteristics are both patient- and disease-specific, making it challenging to determine the generalized features needed to recreate a target disease. Finally, the specific features within a fibrous tissue that drive realistic drug responses remain unclear. Architectural parameters of overall cellular structure, along with fiber length, density, bundle size, organization, and crosslinking density all integratively contribute to mechanical characteristics such as bulk and localized stiffness, viscoelasticity, and plasticity (Figure 1.1). Each of these features progressively changes during disease evolution in a highly disease-specific manner [17 21]. These changes can direct diseased cell phenotypes [28], and in many cases, their effects on drug efficacy remain unclear.

Here, we review emerging strategies to isolate and manipulate specific parameters in the fibrous tissue microenvironment, and ultimately identify those cues important to disease progression and drug response. We limit the scope of this review to the emerging role of biophysical tissue features in driving cell behaviour, and consider the integrated effects of the highly localized tissue architecture, along with arising micro- and macro-scale mechanical tissue characteristics (Figure 1.1). To highlight the potential for designer culture strategies in improving drug screening, we then provide a disease specific context for these findings, by reviewing the impact of fibrous cues on our understanding of breast cancer, a disease for which improved HTS strategies are urgently needed. We conclude with an expert opinion on how these fundamental studies can contribute to developing the next-generation of HTS platforms.

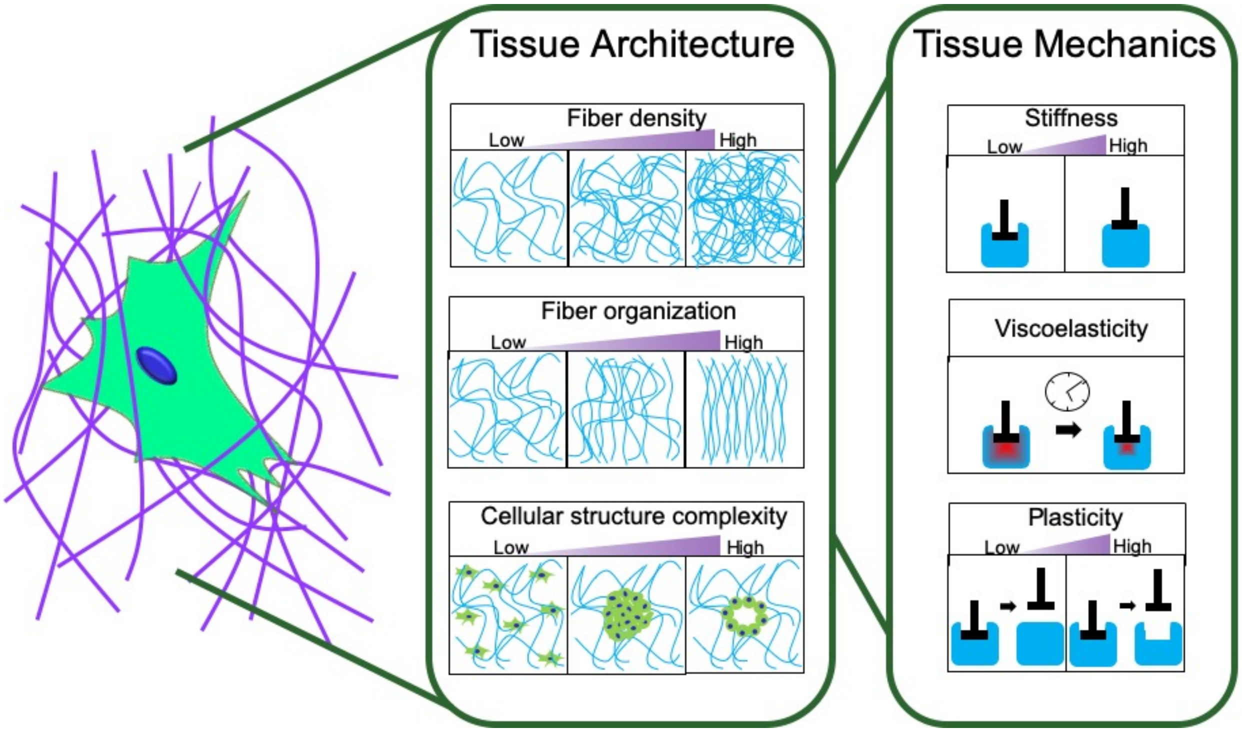

Figure 1.1 The cues presented by the fibrous microenvironment are widely varied. Here we consider the highly localized effects of tissue architecture on cell function, including features such as fiber density, spatial organization, and structural complexity. These features also influence local and bulk tissue properties including stiffness, viscoelasticity, and plasticity; each of which may be critically important to recreating disease-specific drug screening platforms.

1.2 Deconstructing Tissue Architecture

The need to include three-dimensional (3D) cultures in drug screening has been well-established [29] [30] [31] [32]. 3D culture provides critically important microenvironmental cues, and supports analysis of functional cell behaviours such as tissue branching, tissue permeability, and cell invasion [33] [34] [35] [36], that would not be possible in 2D. As multiple excellent reviews already support the importance of 3D cultures over 2D systems [37] [38] [39] [25] [31], here we focus on specific aspects of 3D tissue architecture, including microstructural organization of the surrounding ECM network, the importance of cellular structures within 3D tissues, and their interrelated roles in driving overall tissue function. We consider these characteristics in the context of dissecting and ultimately reducing the complexity of the environment needed for translational HTS.

1.2.1 Microstructural features of the fibrous ECM

Physical characteristics of tissue ECM at the microscale include fiber thickness, length, density, and organization, which vary substantially *in vivo*. These microstructures vary based on tissue location, with fiber diameters ranging from subcellular (<100 nm) collagen fibrils present in basement membrane [40], to 500-800 nm collagen fiber bundles [41] [42] in connective tissues, or larger micrometer-wide fibrils [43] [44]. Increases in ECM density, through increases in fiber thickness and/or quantity, are accompanied by a corresponding reduction in average matrix pore size. These changes have been observed in several diseases, including tumor desmoplasia and fibrotic plaque development [45] [21]. Finally, distinct degrees of fiber network organization and alignment are also associated with cell function and the progression of disease [46] [47]. Each of these features has emerged as a pivotal player in tissue organization and disease progression; and identifying their precise roles is an important step in determining which parameters must be replicated for HTS assays (Figure 1.1).

Architecture of the fibrous matrix can be tuned through a variety of biomaterial engineering strategies. For example, simply gelling natural collagen matrices at cooler temperatures can tune collagen fiber bundling and increase pore size without drastically affecting collagen content or overall matrix stiffness [48]. Incorporating small molecular weight polymers that do not interact with cells, can change fiber lengths and pore sizes [49] [50] [51]. Alternatively, designing dual hydrogels with interpenetrating networks may be used to decouple fiber density from bulk mechanical properties of the matrices [52]. More precise control over these properties may be obtained by electrospinning polymers, to control fiber geometry, density, and adhesive patterns of a synthetic polymer mesh [44]. Furthermore, these defined scaffolds can then be incorporated within various hydrogels, producing a fiber-reinforced composite [44]. Overall organization of fiber mesh can be tuned by incorporating a moving collector plate in the electrospinning process to bias the alignment of fibers [53]. More advanced methods have also been developed, including incorporating magnetically activated, cell-adhesive microgel rods to align a fibrous mesh [54]; a composite hydrogel system, where swelling of one hydrogel results in the uniaxial alignment of the second [46]; or using evaporation mediated flow [55] or external vibration [56] techniques to align fibers during matrix gellation.

These techniques focus on specific features of the fibrous environment, and the results demonstrate the important role of 3D fibrous matrix architecture on cell function. Breast cancer cells in matrices of short fibers (and correspondingly small pore sizes) appear circular with short-lived, weak protrusions [49], exhibit reduced cell contractility [51], and increased oxidative stress [49]. Larger pore sizes give rise to a spindle-shaped, mesenchymal-like phenotype [49] [51]. Although increasing fiber density generally appears to increase cell spread area, cells exhibit a biphasic change in morphology, depending on the number of fibers locally available for contact guidance [44]. Cells also generally align along fibers and extend protrusions in low fiber-density environments, but adopt a pancake-like spread morphology in high fiber-densities [44]. These observations suggest that there is a fiber length and density threshold, below which cell spreading and contractility is impaired [51] [49], factors which directly affect downstream cellular responses.

While each of these studies demonstrates significant architectural effects on a cellular behaviours, these approaches to modulate fiber parameters do not allow consistent and cellular-scale control of these features. Instead, cells experience a heterogeneous ensemble of stimuli, and read out an ensemble average of cellular responses. Furthermore, these approaches do not allow the precision to individually tune each fiber parameter. For example, increases in fiber width affects both adhesive ligand availability through increased surface area, as well as fiber spatial distribution, which may affect cells through distinct mechanisms. Finally, emergent larger-scale mechanical properties of the matrix (section 3) are also prone to change with many of these strategies. To better understand the specific influences of fiber features on cells, it is helpful to design experiments that consider the separate roles of three-dimensional, topographical structures and adhesive patterns on cell function, both of which may independently affect cell response.

Fiber-like topographies alone can be recreated by molding linear, nano-grooved substrates such as poly(DL-lactic acid) (PLA) [57], optical adhesives [58], or polyurethane [59], and independently drive uniaxial cell alignment, contact guided migration, and control over morphological phenotypes such as cell aspect ratio. Alternatively, the spatial distribution of adhesive cues that accompany fiber microstructure may drive cell function. To study these factors, several groups have devised methods to pattern adhesive proteins on topographically flat and otherwise non-adhesive 2D surfaces in fiber-like patterns. This can be accomplished by laser-based removal of a non-adhesive surface [60], exposing adhesive sites on a blocked surface by mechanical fracture of the non-adhesive layer [61] [62], microcontact printing [63], e-beam lithography [64], and electrospinning tunable fibers over open wells [65] [53]. Micropatterns have also been created along three-dimensional surfaces to study the effects of individual fiber tortuosity on cell morphology [66]. These approaches enable independent assessment of the role of fiber alignment (anisotropy), spacing (density), and contact area (fiber width) on cell behaviour.

Collectively, these studies have demonstrated that subtle characteristics of the supporting fibrous ECM mesh affect virtually every aspect of cell function. Cell shape is a well-established predictor of fate, function, and proliferative state [67] [68] [69], and is hence of crucial importance. Cells preferentially align with and migrate along pathways formed in the fibrous mesh of ECM proteins [47], and adopt elongated cell morphologies that closely correspond to the orientation of the underlying matrix [60] [66] [63]. This characteristic is independent of culture platform dimensionality, and has been consistently observed on 1D linear arrays, on flat [60] and topographically complex surfaces [66], and on aligned, fully 3D matrices [46], given sufficient contact area and spacing between fibers is maintained [66]. Fibroblasts cultured on 1D linear fiber arrays, as compared to unaligned surfaces, exhibit uniaxial cell spreading, polarization, and migratory behaviours that strongly resemble those cultured on 3D cell-derived matrices [60] [63]. This behaviour is independent of the ligand type and density, suggesting that the linear directional cue provided by the cell-ECM contact plays an important role in determining uniaxial phenotype [60].

1.2.2 Cellular structures within tissues

In contrast to cells constrained on flat tissue culture plates, cells in three-dimensions can be organized into a wide variety of structures that present cells with distinct cues, driving behaviour and overall tissue function. For example, healthy breast epithelial cells can be induced to grow from single cells to form hollow, polarized spheres resembling native breast tissue structures when cultured in 3D reconstituted basement membrane (rBM) [70] [71]. Indeed, these structural features also direct homeostasis of healthy tissue and tissue degradation during disease: when formed into hollow, polarized spheres, healthy breast epithelial cells are growth arrested and show high resistance to apoptotic signals compared to growth on a 2D dish [70]. In contrast, breast tumour cells that also begin as single cells in 3D matrices form a disorganized mass of aggregated cells that may ultimately shed cells into the surrounding matrix. These architectures are also cell-type specific: single fibroblasts will remain spaced apart in 3D matrices [44]. Each of these tissue structures present distinct microenvironmental cues to their component cells, including control over cell shape [67] [72] and tissue curvature, which provides stress gradients that affect invasion and migration [10] [35] [8] [73].

Recreating these tissue structures presents considerable challenges and opportunities for HTS platforms. Engineered tissues are generally achieved via three main mechanisms: precision assembly, guided assembly, and self assembly (Figure 1.2). In self-assembled tissues, cells themselves direct their formation through processes of growth, invasion, and matrix remodelling, as is the case with the acinar structures described above, and organoid models derived from stem-cell precursors [74]. While tissue self-assembly is relatively straightforward to implement at scale, there is no control over tissue architecture, and cells can often form undesired structures. For example, placental organoids form a fused syncytial mass within the organoid, rather than on the surface as in human placental villi [75], and this may not be desirable for the specific screening application being developed. On the other end of the spectrum, precision assembly involves precisely positioning individual cells in pre-defined locations within an encapsulating matrix [76] [77] [78]. Limitations in speed of precision-assembly strategies currently prevent scale up towards high-throughput drug screening, and are therefore not considered in this review.

An alternative and promising strategy is to provide cells with a pre-organized template that can support the formation of more advanced and controlled structures. For example, either the cells or the surrounding matrix can be pre-molded into a specified shape. Cells packed into these shapes are then allowed to self-assemble to create tight junctions with fine control over tissue structure. Multicellular aggregates or spheroids can be considered to form via this guided assembly, as they are formed by culturing cells in close proximity to each other, using techniques such as the hanging drop method for micromass culture, aqueous two-phase system (ATPS), or micropocket devices [79] [80] [81]. Such approaches are often used to generate three-dimensional tumour models that may be applied to screening [79 82 83]. While these approaches do increase handling complexity (Figure 1.2), they provide a potentially scalable route for designer high-throughput studies [84]. For example, tissues with hollow lumens are required to understand the role of blood vessels and ducts for systemically transported drugs, and it therefore becomes important to capture the lumenized morphology of these tissues. Lumens can be engineered into three-dimensional tissues using a variety of strategies. A simple and accessible method to achieve this is to polymerize ECM around a removable rod made of various materials such as needles, polydimethylsiloxane (PDMS) [33], gelatin [34], or even a highly viscous fluid [32 85]. These materials are subsequently removed to leave a hollow tube through the matrix. Endothelial or epithelial cells can then be seeded into these tubes. Similarly, more complex templates that mimic structures such as branches can also be used to micromold appropriately-shaped cavities, and many of these presented lumen-engineering strategies have been designed with increased throughput in mind [35 36 33 86 87].

In the context of HTS assays, every additional processing step introduces potential for reduced assay robustness and reproducibility. Hence, tissue engineering for HTS systems is akin to solving the “Goldilocks” problem: how do we reduce culture complexity enough to manage HTS standards, while maintaining adequate tissue complexity to produce translational results, thereby achieving a “just right” screening platform. Guided assembly culture models may provide a realistically attainable and sufficient solution.

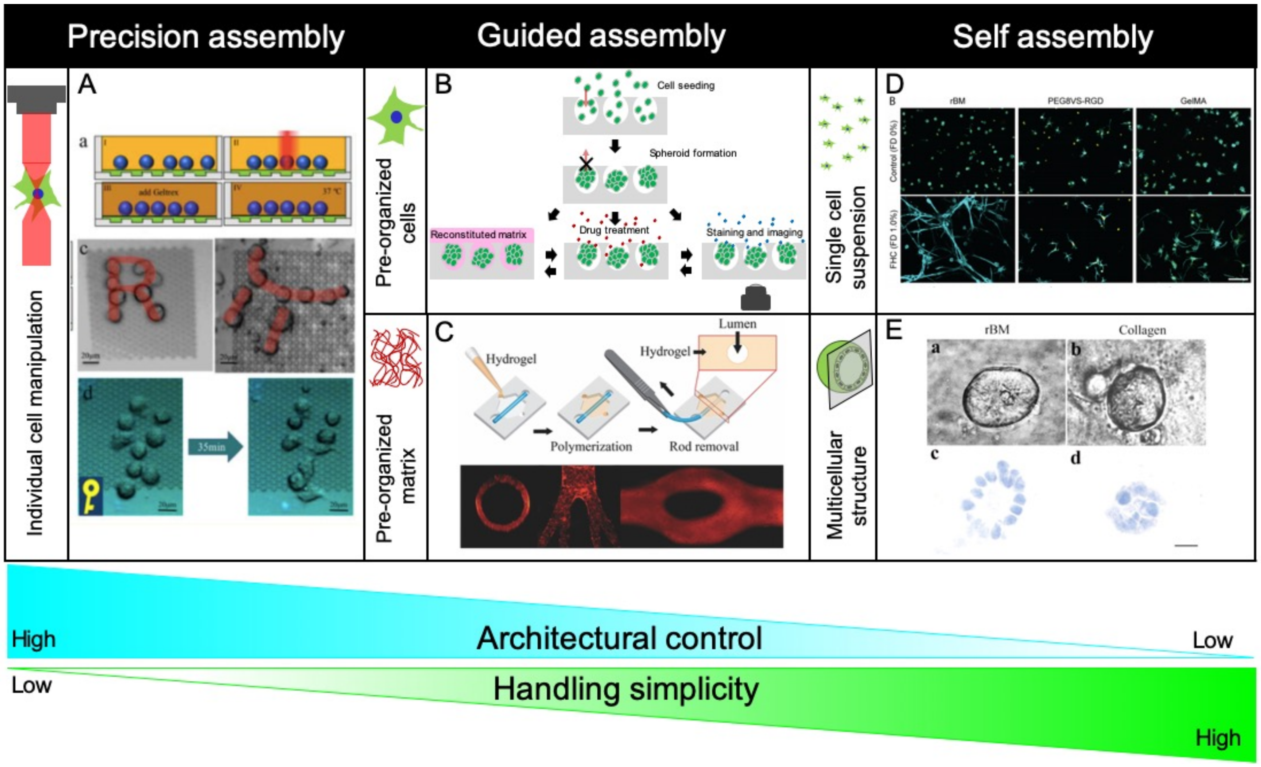

Figure 1.2 3D tissue engineering approaches for specific structural outcomes. (A) Precision assembly uses tools such as optical tweezers for fine cell placement within an overall tissue structure (Adapted with permission from [69] © The Optical Society). Pre-organizing either the (B) cells into spheroids [70], or (C) matrix into ducts are both examples of tissue guided assembly (reproduced with permission from [23] © John Wiley and Sons). Tissue self-assembly into structures includes (D) single cell suspensions of fibroblasts, with different spread morphologies depending on the ECM suspended in (scale: 100 µm; reproduced with permission from [33] © (2019) American Chemical Society), or (E) multicellular spheres containing either polarized cells with a hollow lumen or solid structures depending on the ECM suspended in (scale: 25 µm; reproduced with permission from [71] © The Company of Biologists Ltd.).

1.3 Deconstructing Tissue Mechanics

The mechanical properties of biological tissues arise from the highly local, microstructural features described in section 2, and these mechanics, felt at both a local and larger scale, have now been implicated as powerful regulators of cell functions. Changes in local tissue mechanics occur in a wide variety of diseases [88] [89] [90] [91], and since these changes play a fundamental role in cell response, it is likely of critical importance to include these mechanical parameters in drug screening applications. However, tissue mechanics can be quite complex, and distinct mechanical features are emerging as being differently important for various applications, making it important to identify the precise parameters needed to incorporate into a specific HTS assay.

Biological tissues exhibit elastic, viscoelastic, and plastic behaviours (Figure 1.3). Elastic properties of the material allow it to store energy in the form of internal stress while being deformed, and return to the original shape once an applied load is removed. In contrast, viscoelastic materials dissipate internal stress over time through internal reorganization, allowing the material to gradually flow under an applied load. Plasticity describes permanent deformation of a material, which does not return to its original shape after the load is removed. Although the impact of matrix stiffness has been established for over a decade [92] [93], the importance of viscoelasticity and plasticity have only recently emerged (reviewed in [94] [95]). However, manipulating these parameters individually can be quite challenging, and in this section, we review models and approaches to understand how complex tissue mechanics might influence cell function and drug response.

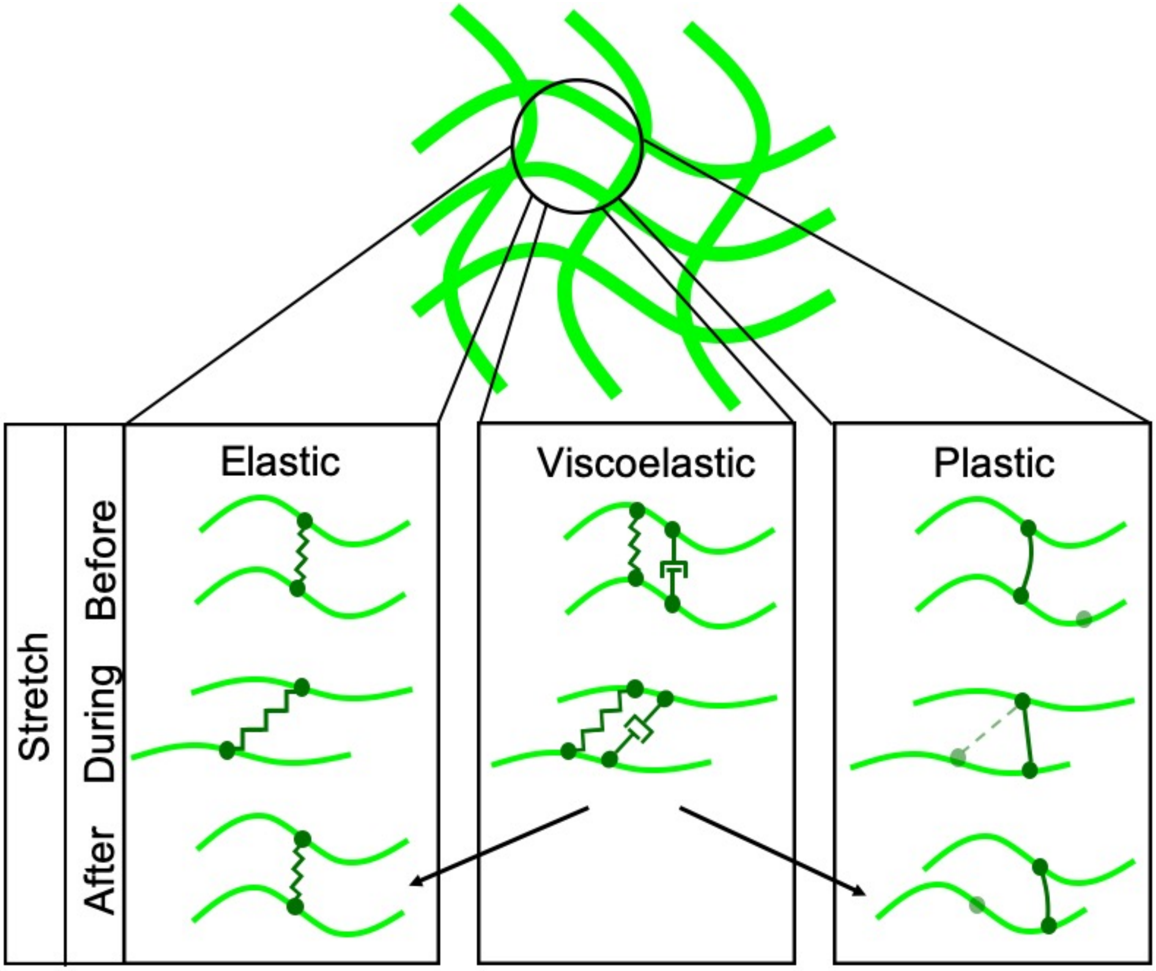

Figure 1.3 Elastic, viscoelastic, and plastic behaviors arise from unique mechanisms during ECM stretch. Elastic materials behave like rubber bands, where energy from an applied force is stored in the material deformation. Hence, when the force is removed, the material will rapidly return to its original shape. Viscoelastic materials display both elastic and viscous properties, and rather than the stress remaining stored in the material, a time-dependent stress decrease occurs. Viscoelastic materials may or may not return to their original shape when the force is removed, depending on elastic recovery force strength and the mechanism of viscous dissipation. Plastic materials display permanent deformation following an applied force, often due to new bond formations which are stronger than elastic recovery forces.

1.3.1 Elasticity

The mechanical elasticity (or stiffness) of tissues is a measure of how resistant the tissue is to applied deformation. Increases in tissue stiffness can be associated with disease progression in a wide variety of organ systems, including tissue fibrosis [96] [97] and breast cancer [20] [98] [99], amongst many others. To better understand how these disease processes arise, multiple biomaterial models with tunable stiffness have been developed, each presenting distinct advantages.

The simplest and most common strategy to tune stiffness in biomaterials is to increase crosslinking density in the hydrogel network. The earliest example of this is in polyacrylamide, a hydrogel material in which monomer and crosslinker components can be adjusted to create stiffness-tunable 2D culture surfaces [100]. Functionalization of polyacrylamide surfaces with an extracellular matrix protein or peptide allows precise definition of the adhesive molecules presented to cells, and this material has been broadly used in a variety of culture formats including within microfluidic channels [101], at air-liquid interfaces [102], and as a substrate in pseudo-3D "sandwich" systems [103] [104] [105]. However, the harsh crosslinking reactions required for gelation limit the use of this material as a true 3D culture system, and similar tuning strategies have been developed for synthetic polymers such as polyethylene glycol (PEG), which can be used for 3D applications [106]. These materials can also be functionalized with candidate peptides and dynamically stiffened or softened on exposure to light by incorporating photosensitive crosslinkers [107] [108].

An important consideration of these synthetic hydrogel systems is that they form with pore sizes smaller than individual cells, creating a cage that prevents cell spreading in 3D [109]. Therefore, they must be engineered with cell-cleavable crosslinks [110] to allow cell spreading within the matrix. How these cleavable sites affect the local rigidity surrounding individual cells is uncertain, and processing strategies such as gas foaming, freeze-thawing, and including porogens have been developed to tune pore size in these materials [111]. Alternatively, using naturally-derived polymers such as gelatin [112] [113] [114], collagen, or hyaluronic acid [115] [116] [117] resolves these issues, and can be chemically modified to stiffen by addition of crosslinkers, or interpenetrating networks of other hydrogels [118] [119] [120] [121] [122]. However, the use of natural biomaterials does come with a significant caveat, in that cells may remodel the matrix through enzymatic activity, ECM deposition, and fiber reorganization. Hence, when changes to fiber architecture occur, there is a corresponding change in fiber mechanics. For example, increased collagen fiber density and linear organization increase the stiffness, or stiffness anisotropy of the tissue [123] [124] [125]. Synthetic, elastic matrices on the other hand, can be engineered to present stable mechanical properties throughout the culture period [126].

The use of both synthetic and natural biomaterials do present some challenges in precisely decoupling stiffness from other variables, and cells still experience heterogenous matrix properties such as porosity (and associated stiffness), which are not precisely controlled throughout the materials. The overall strategy to tune stiffness, requiring changes in crosslink density and material microstructure, has also generated some controversy as to which features drive cell response [127 128], and microfabricated analogues may provide unique strategies to independently manipulate adhesion and mechanical stiffness. For example, micropillar arrays have been fabricated with precise control over pillar diameter and pillar height, to independently tune these features [129 130]. To capture fiber-like phenotypes, stiffness-tunable electrospun biomaterials have also been developed to independently manipulate fiber stiffness, geometry, and network architecture [131 53].

The above studies generally demonstrate that stiffness affects a wide variety of cellular processes. On 2D hydrogel surfaces, stiffer materials induce cell spreading and proliferation [129], provided that adhesion sites are spaced closely enough to allow spreading. In contrast, increased stiffness in 3D fibrous matrices decreases cell spread, migration, and proliferation [106 107 132 114 117 110 115 113119 120 133]. These responses are likely also dependent on cell type [134 135] and disease context, and must therefore be carefully considered in the specific context of the HTS assay being developed.

In order to properly consider microenvironment stiffness in HTS assays, the stiffness of healthy to diseased tissue of interest must first be characterized. Several techniques exist to measure material stiffness. At the subcellular scale, this can be accomplished using techniques such as microrheology and atomic force microscopy. Microrhelogy involves injecting fiducial particles within the nano and micrometer size range into either intra or intercellular spaces, and tracking their displacement with time. This displacement can either be due to endogenous forces such as Brownian motion, or externally applied forces from devices such as magnetic tweezers[136]. Atomic force microscopy is another technique commonly used to measure subcellular stiffness and involves pressing onto the surface of a cell or tissue with a fine tipped cantilever. The cantilever arm has well characterized mechanical properties; therefore, as the tissue is depressed under a controlled applied force, the indentation depth can be used to calculate highly local tissue stiffness[137].

At the bulk tissue scale, shear rheometry and ultrasound or magnetic resonance (MR) elastography are two examples of commonly used stiffness measuring techniques. Shear rheology requires larger samples of 3D tissue to be placed between 2 plates. A known strain is applied to one plate, while the shear stress within the tissue is measured[138]. Ultrasound and MR elastography on the other hand, use ultrasound or MR waves respectively to apply the external stress, and tissue strain is measured[139] [140].

The above subcellular and bulk tissue scale techniques are excellent for high resolution and average global measurements respectively, but they do not capture stiffness at the scale surrounding a cell. For this, techniques exist to measure cellular and local multicellular scale stiffness. First, micropipette aspiration involves placing a micron range sized pipette tip at the surface of the tissue, applying a controlled suction pressure, and visualizing how the tissue curves as it is aspirated into the pipette tip[141]. This technique is limited to measuring superficial stiffness at the cell or tissue surface, and is unable to capture internal tissue stiffness. Twisting magnetic cytometry involves subjecting magnetic particles, that can range between the nanometer to micrometer scale, to an external oscillating magnetic field and visualizing the displacement of the particles with time[142]. This technique often requires custom device installation and specialized equipment. Cell-sized magnetic oil droplets have also been designed to deform under a magnetic field, probing the surrounding tissue stiffness[143]. While able to capture evolving stiffness within a tissue, it is limited to highly soft tissues under 1kPa. Finally, µTAMs are thermally responsive stiffness sensors that swell following a slight drop from culture temperature[144]. After calibrating the sensors in polyacrylamide of known stiffnesses, the degree of µTAM swelling can be used to measure cell-scale stiffness within a dynamically evolving tissue.

1.3.2 Viscoelasticity

Viscoelasticity is a measure of internal stress dissipation (Figure 1.3). Changes in viscoelastic parameters accompany diseases such as osteoarthritis [145] [146] [147], tissue fibrosis [148] [149] [150], and breast cancer [151] [152] [153] [154] [155] [156] [157] [140] [158], and designing biomaterials to independently tune and capture the effects of both viscous and elastic properties is important in identifying relevant HTS parameters.

Two general strategies exist to incorporate viscoelasticity into materials. First, for stiffness-tunable materials, adjusting the concentration of crosslinkers to monomers can put the material outside a linear-elastic regime, as demonstrated in 2D cultures on polyacrylamide [159] [160] [161], gelatin [162] [163] and PDMS [164], due to the formation of defect structures in the poorly connected gel networks, [159] or inherent viscoelastic characteristics in crosslinked matrices. Since crosslinking must be carefully limited to produce these hydrogels, their fabrication and gelation often requires precise control over temperature and oxygen conditions. Alternatively, the viscosity of the gel's liquid phase can be modified with additives [165] [166] [167], without drastically affecting elastic properties, while the liquid phase provides the dissipative element. Although technically simple, these methods do not allow dynamic, on-demand changes in material properties, which have proven useful for many applications [163] [168] [169].

Customized crosslinkers can also be used to tune viscoelastic properties [7], and these approaches can be compatible with 3D culture formats. Reversible bonds including ionic [170] [171] [172], guest-host [173] [169], hydrazine/aldehyde [174] [175], or thioester [176] crosslinks are some examples. These crosslinkers exhibit half-lives of minutes to months, which enables well-defined control over stress-relaxation rates. However, manipulating crosslinks also effects elastic properties, making it quite challenging to fully de-couple elastic and viscous effects, without incorporating additional covalent bonds, as demonstrated in guest-host hyaluronic acid gels [169] and polyacrylamide [161] [160]. Alternatively, alginate hydrogels can be modified with spacers grafted onto the polymer backbones to sterically hinder crosslinking of the alginate chains, with higher spacer densities and lengths both leading to faster stress relaxation [177]; or developed with covalent binding sites and calcium-activated ionic binding sites, to tune how much stress dissipates from the material independently of stiffness [178].

In general, increased stress relaxation prompts increased cell spreading and proliferation for fibroblast-like cells [172] [177] [176], and myoblasts [175], but decreased spreading in hepatic stellate cells [169] and hMSCs [168]. Once again, these responses seem dependent on cell type, culture dimensionality, and disease context, suggesting that disease-specific experiments are necessary prior to designing appropriate HTS assays.

1.3.3 Mechanical Plasticity

While tuning viscoelasticity involves controlling the time-dependent properties, the degree of plastic deformation sustained by a material during these energy dissipation processes is also emerging as a key parameter to consider in designing biomaterial culture platforms. In real tissues such as excised human breast tumor masses, plasticity is observed [179], and mesenchymal cells produce stresses large enough to plastically deform these biomaterials [180] [181] [182]. Plasticity in real materials is dependent upon applied stress, stress relaxation times, and mechanical stiffness [94]. Hence deconstructing the specific role of plasticity in tissue response requires novel biomaterial designs. Alginate polymers have previously been crosslinked with rBM in an interpenetrating network, to tune mechanical plasticity. Changing the molecular weight of the alginate, in combination with the calcium crosslinking density has been shown to independently tune plasticity [179], as does changing the fraction of covalent crosslinks present in the matrix, using enzymatic crosslinking [183]. However, the degree to which this property is distinct from viscoelastic behaviour is unclear, as viscoelasticity also involves crosslink breakage and reformation. Viscoelasticity and plasticity thereby have overlapping mechanisms, and local permanent deformation of a material arises when the elastic portion of the hydrogel network is insufficient to enable the return of the material to its original position after unloading.

1.3.4 Cell-induced forces

During many tissue processes involved in developmental morphogenesis, tissue homeostasis, and disease progression, cells apply force onto their surroundings, during migration and ECM remodelling[17924]. For example, breast cancer cells apply force to tug on surrounding ECM as they invade their surroundings[179], and wound closure relies on fibroblast contractile forces[4]. These forces impact the cellular microenvironment through locally applied strains[53], and this signalling cue drives disease relevant cell behaviours such as smooth muscle actin expression[184] and increased ECM production[185]. Understanding these local, cell-induced forces in various tissue settings could therefore improve drug culture models.

Various techniques exist to measure cell-induced forces. Traction force microscopy involves embedding small fluorescent particles into a substrate, and measuring the displacement of the particles as the cell tugs on the substrate[186]. This technique can be done on 2D elastic surfaces, however, this non-fibrous, elastic environment is not representative of 3D fibrous, remodelling tissue. Since cells display unique behaviours in 3D fibrous tissue[187], measured forces may not be representative of forces *in vivo*. Traction force microscopy has also been applied to 3D fibrous tissues to gauge relative spatial forces within a matrix[188], however, the non-linear behaviour of protein fibers makes calculating forces complex. Moreover, this technique is not compatible within a cell dense setting where tracking the high density of individual particles becomes challenging. Another technique harnesses the use of Förster resonance energy transfer (FRET), where the emission wavelength of a donor probe is the excitation wavelength of a paired acceptor probe. When the two probes are within nanometers of each other, the emission wavelength of the acceptor probe is visible, known as the FRET signal. These two probes can be connected by a spring of known stiffness. If the probes become separated under the force of a tugging cell, the threshold tugging force is known[189]. This strategy is well suited for small forces leading to similarly small strains at the single cell level, and would be challenging to implement at tissue scale. Various unique microfabricated tissue devices are also used to measure single cell and bulk tissue forces[190] [191] [192] [193], such as tissue suspension between PDMS pillars, and pillar deflection measures tissue generated forces [191].

The above methods are useful to understand single cell or average bulk stresses; however, measuring local forces within dynamic tissues requires alternative innovations. To this end, various cell-sized force sensors have been incorporated into tissues. Oil microdroplets have been used to visualize anisotropic forces within remodelling tissue[194]; however, droplet deformation cannot measure isotropic stress magnitudes as oil is incompressible. Compressible sensors have also been designed from materials such as alginate[195], and polyacrylamide[196] [197] [198]. These sensors allow quantification of local force magnitudes within dynamic tissues.

1.4 Contributions to breast cancer research

Although the concepts of deconstructing various elements of the fibrous tissue microenvironment may seem academic, these fundamental observations of cell-environment interactions suggest important design strategies for future HTS drug platforms. While the deconstruction techniques have been applied in a variety of disease models, here we briefly review their impact on our current understanding of breast cancer, a disease that affects 1 in 8 women in North America, has a 15% mortality rate, and has seen no improvements in survival for women under 50 since 2007 [199]. Current HTS systems are not effective, suggesting the need for more advanced and realistic platforms.

3D culture of breast cancer cells has now been established to influence breast cancer drug screening results. Cells cultured in a fibrous matrix are much less responsive to accepted chemotherapies than in 2D systems [27 70 200 201 202], and culture in 3D spheroid models confers further resistance [203], perhaps due to differences in proliferation and consequently uptake, for drugs such as paclitaxel that selectively target rapidly-dividing cells [187].

During breast cancer progression, collagen fiber density and crosslinking increases, matrix pore size decreases, and fiber linearization increases [123 124]. Increased tissue density is generally considered a risk factor for breast cancer disease progression [91], and may also further influence drug uptake by limiting delivery of therapeutics [204] or altering cell function. Drug dosage is an important element of any drug discovery or screening study and must be considered carefully, further supporting the need to conduct testing in realistic environments. Moreover, decreased pore size confines cells to limit spreading and mobility, and when cultured within these confining 3D fibrous meshes, cells appear to compensate by upregulating cell-cell adhesion genes [51] and attaching to each other instead, forming multicellular tubular network structures [50]. Some interpret these structures as resembling lobules and ducts in normal breast tissue [51]; however, based on β1-integrin upregulation in these networks, others suggest this phenotype is more similar to vasculogenic mimicry, which is associated with poor prognosis for breast cancer patients. This suggests that confining architecture is important during metastatic disease progression [50], and should be considered in HTS assays. Fiber linearization is also influential, as directed cell migration is observed on aligned 3-D matrices which enhance the migratory behaviour of metastatic cells. This enhanced migratory behaviour was lost on isotropic matrices and with non-metastatic lines on pre-aligned matrices [46].

The above architectural changes must be accompanied by changes in fiber mechanics. Stiffer matrices have been demonstrated to drive an increase in proliferation and invasion amongst non-malignant cells [118], but seem to have the opposite effect on invasive breast cancer cell lines [119]. Of interest, invasive breast cancer cells may adapt to the surrounding mechanics. When cultured within high density, stiffened collagen, invasive speed is initially slowed [50] similar to their deceleration within synthetically stiffened environments [119]. However, following a cell cycle, the speed of cells greatly increases [50]. This suggests that breast cancer drug screening timelines should last longer than a cell cycle.

Interestingly, the dynamic stiffening of 3D matrices also influences drug response, and invasive breast cancer cell lines show greater chemoresistance within these dynamic cultures than cells cultured in static high-stiffness matrices [205], but no effect was noted on less aggressively invasive cell lines. These effects are not observed in 2D settings, further suggesting the need for disease-specific and stiffness-tunable 3D screens. The fact that dynamic stiffening is required also strongly indicates that viscoelastic and plastic behaviours that contribute to these changes may be important to consider.

Finally, invasive breast cancer cell lines display higher invasive behaviours in highly plastic matrices, such as higher cell spread, motility, and protrusions; even though other matrix properties remained the same [179] [183]. Plasticity may hence be an important driver of breast cancer specifically.

1.5 Expert Opinion

While the capacity to dissect the microenvironment and fundamentally understand cell-matrix interactions is certainly of academic value, we ask here whether these theoretical insights might allow us to bridge the gap towards practical gains in drug discovery. We believe that while such knowledge translation is both possible and highly desirable, implementing these approaches for next-generation HTS in particular presents unique challenges and opportunities for knowledge acquisition, development of insight, and technological innovation.

First, the technologies developed to disentangle the fibrous microenvironmental parameters simultaneously highlight the importance of these factors, as well as our relatively limited knowledge of their specific impact in various organ systems. The studies conducted to date demonstrate that common rules for all cell types are a myth. Precisely-defined microenvironmental cues appear to affect cells differently. For example, endothelial and glioma cells seem to be largely unaffected by the local presence of surrounding fibers [48 52], whereas fibroblasts and breast cancer cells exhibit different morphologies and phenotypes within matrices of different densities. Similarly, while the role of mechanical stiffness has now been well-established in a variety of tissues, the effects of viscoelasticity and plasticity have only recently been elucidated, and their importance is tissue-specific and requires further investigation. Moreover, whether temporary viscoelastic deformations are fundamentally different from permanent plastic deformation is unclear, and further fundamental studies are needed in tissue systems specific to the disease being screened.

Second, while these microenvironmental factors have an established impact, it remains unclear what the *in vivo* microenvironmental conditions actually are, particularly during disease progression. For example, breast tumors have demonstrated both greater and lower viscous behaviour than healthy tissue [153 158 152], and the factors that cause these changes remain unknown. Changes in fiber composition, density, organization, and crosslinking that lead to these viscous changes are largely speculative, although a few *in silico* and *in vitro* approaches have recently been developed to address this [206 181]. These differences may also arise from measurements made at different length-scales, and we therefore argue that it is important to characterize tissue biophysics at the length scale of individual cells within living tissues undergoing disease progression. To this end, the recent development of cell-sized sensors that can be embedded in human tissue for long-term measurements of force [198 207 208 209], stiffness [210 211], and viscoelasticity [212] may prove particularly valuable.

Third, while identifying the fundamental microenvironmental parameters underlying disease progression is a good first step, developing scalable culture systems that implement these specific features for HTS presents unique technological challenges. Running millions of assays in a typical HTS screen requires robustness, reproducibility, automation, and optimization of assay costs and time. In some cases, these fundamental studies immediately provide strategies to scale up screening: for example, the use of 1D and 2D adhesive patterns on substrates can prompt cells to behave as if they were in 3D [40 57 60 63], and this strategy can be directly applied to conventional HTS microscopes and data analysis workflows. Where fibrous 3D cultures are required, techniques must be developed to address difficulties in forming 3D structures with sufficient throughput, handling these structures during requisite wash steps, and 3D imaging.

Integrating microfabrication technologies with tissue engineering strategies may provide valuable tools to address these challenges. For example, arrays of micro-reservoirs have been developed on-a-chip, into which nanoliter volumes of prepolymerized tissue may be loaded, cultured, and assayed [213 214]. Liquid-in-liquid patterning techniques have been developed to "print" microscale tissue volumes in existing well-plates, using standard robotic pipetting infrastructure [215]. Similarly, 3D bioprinters now offer such capabilities [216]. Using a microfabricated hydrogel template, tissue engineered structures such as spheroids [81] and lumenized vessels [33 35] can also be rapidly formed, stimulated, and analyzed without handling issues. These techniques have added advantages of using small volumes of cells and reagents, which reduces assay cost and analysis time, and may ultimately enable precision medicine approaches on a patient-specific level. Finally, considerably more advanced microfabricated platforms (organ-on-a-chip systems, recently reviewed in [217]) are being actively developed by multiple research groups, and may eventually be scalable for HTS applications.

Collectively, these challenges and innovations demonstrate that while umbrella solutions for HTS were initially effective in identifying low-hanging fruit, the development of next-generation therapeutics will require targeted HTS strategies customized to mimic the microenvironment of the specific target disease. The diverse tissue structure in the human body, the variability that arises during disease progression, and the specificity of a cell's interaction with the microenvironment, each suggests that disease-specific HTS approaches are needed. Therefore, we conclude that understanding the tissue microenvironment, incorporating those cues most relevant to the disease of interest, and developing high-throughput microfabricated HTS assays will be required to strip away unnecessary costs and complexities in the drug development pipeline, and focus platforms towards identifying high-value therapeutic targets.

Chapter 2

Bioprintable, stiffness-tunable collagen-alginate microgels for increased throughput 3D cell culture studies

The following chapter addresses the first objective of my thesis by designing and characterizing a robust 3D tissue contraction platform capable of tuning initial tissue stiffness. Here, I explain the rationale behind the platforms design, describe the methods involved in platform production, validate the platforms utility within commonly used assays, and discuss the findings of how stiffness within a 3D fibrous model influences fundamental cell phenotypes such as cell spread, proliferation, and collagen matrix contraction. This work is published in ACS Biomaterials Science & Engineering, and is reproduced with permission from Ort C, Chen Y, Ghagre A, Ehrlicher A, Moraes C. Bioprintable, stiffness-tunable collagen-alginate microgels for increased throughput 3D cell culture studies. ACS Biomater Sci Eng. 2021 Jun 14;7(6):2814-2822. doi: 10.1021/acsbiomaterials.1c00129. Copyright 2021 American Chemical Society.

Abstract

3D culture platforms with tunable stiffness have the potential to improve applications such as drug discovery, organoid studies, and stem cell differentiation. Both dimensionality and stiffness regulate many crucial cellular processes. However, 3D culture models are often limited in throughput and difficult to adopt for widespread use. Here, we demonstrate an accessible 3D, stiffness-tunable tissue culture platform, based on an interpenetrating network of collagen-1 and alginate. When blended with polymers that induce phase separation, these networks can be bioprinted at microliter volumes, using standard liquid handling infrastructure. We demonstrate robust reproducibility in printing these microgels, consistent tunability of mechanical properties, and maintained viability of multiple printed cell types. To highlight the utility and importance of this system, we demonstrate distinct morphological changes to cells in culture, use the system to probe the role of matrix mechanics and soluble factors in a collagen contraction assay, and perform a prototype viability screen against a candidate chemotherapeutic, demonstrating stiffness-dependent responses.

2.1 Introduction

Three-dimensional biomaterial culture systems have emerged as critically important platforms for in vitro cell-based applications, as dimensionality is an important regular of cell function, influencing morphology, proliferation, and migration, amongst many other cell behaviours.[38] Technological innovations in biomaterial design now afford the ability to tune key microenvironment properties such as binding ligand density and stiffness; variables known to drive cellular function.[218] [52] [44] [118] This is particularly important in models of development, disease, and drug efficacy, as stiffness is now a well-established driver of important cellular processes connected to stem cell differentiation and the progression of many diseases.[93] [219] [135] [123] However, conventional culture technologies used in high-throughput applications such as petri dishes, and even spheroid and organoid cultures cannot be easily tuned to manipulate these parameters, as previously reviewed.[220] Hence, the ability to tune stiffness in engineered models may be particularly desirable to advance applications such as drug discovery, personalized medicine, and tissue engineering screening platforms.[25] [221] [222] [223] [224] [225] [220]

Applying these platforms beyond relatively artisanal fundamental studies, and towards industrial-scale screening applications is made difficult by the challenges associated with increased-throughput testing of mechanically-tunable 3D cultures. In general, 3D culture models require large volumes of expensive reagents, high cell quantities, and complex handling procedures; all major drawbacks in fields where cost, speed, and robustness drive culture adoption. Bioprinting is emerging as a useful technique to create simple 3D tissues[226] [227] [228] [229] and we have previously demonstrated the use of aqueous two-phase systems (ATPS) to print microliter volumes of cell-laden collagen hydrogels within a well-plate, using standard liquid handling tools.[215] Printing small volumes is particularly challenging with conventional printing methods, as they are highly sensitive to evaporation, often resulting in low cell viability.[215] This issue is circumvented in the ATPS-collagen system, where gelation of small volumes occurs while submerged, with no gel-to-air interface. Briefly, this is accomplished by inducing phase separation of a collagen pre-polymer during gelation, by incorporating immiscible dextran and polyethylene glycol (PEG) polymers into the two phases. The small-volume gels further allow rapid diffusion and equilibration of large molecules, simplified imaging, reduced reagent consumption, and easy adoption into existing high-throughput workflow infrastructures.

In this work, we build upon our previous studies and demonstrate the ability to precisely control stiffness independently from binding ligand density within this bioprintable collagen system. Interpenetrating networks (IPNs) of alginate with extracellular matrix (ECM) have previously been used to control stiffness of engineered cultures with great success.[218] [230] [118] [231] [232] [121] [233] [120] Alginates are biocompatible polysaccharide polymers that can be crosslinked using cell-friendly divalent ions such as calcium, and present no additional binding sites to cells unless specifically modified to do so.[234] Collagen-1 is the most abundant extracellular matrix protein present in tissue[13] and provides biochemical feedback for cellular processes such as survival and proliferation.[235] Blending these two gels into an IPN with the polymers necessary to induce phase separation should hence provide the ability to tune the mechanical properties of ATPS-bioprintable microgels.

To provide a robust system for increased throughput of 3D, mechanically-tunable cultures (Figure 2.1), we designed and characterize collagen-alginate IPNs as biomaterials for automated ATPS-based “printing” into microlitre droplets. We demonstrate reproducible microdroplet printing with precise control over storage modulus, and distinctive stiffness-driven morphological phenotypes for breast cancer cells and fibroblasts. As a first application for this platform, a chemotherapy screening assay of breast cancer cells demonstrated the role that stiffness plays in drug response and underscores its placement in high-throughput screening. Finally, contraction assays demonstrated the role of stiffness in these remodellable micro-matrices under contractile stimulating or suppressive conditions.

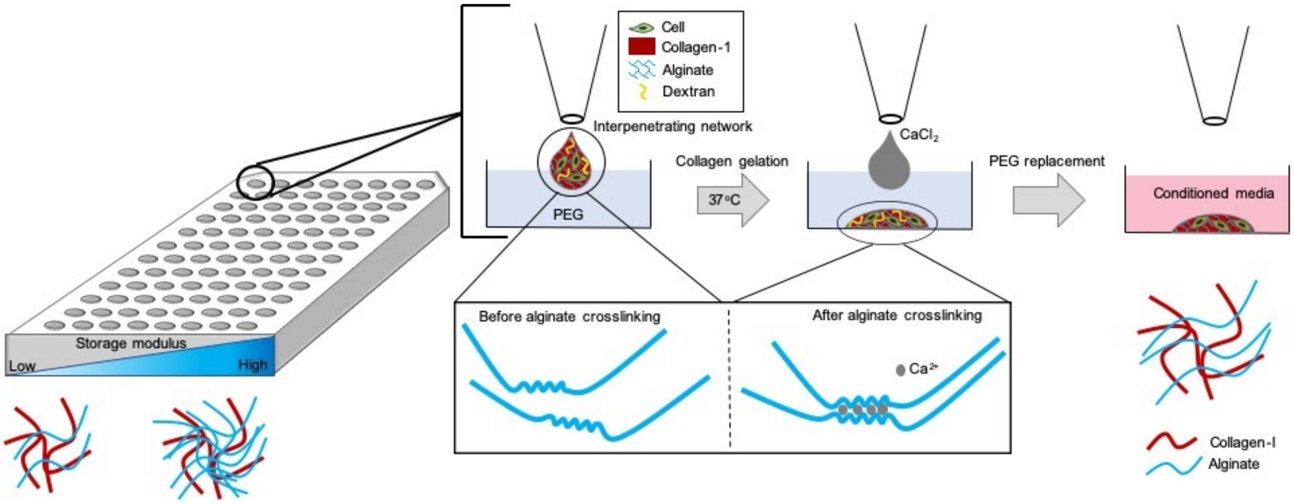

Figure 2.1 Schematic of the stiffness tunable microgel printing culture platform. Microgel matrices consist of a constant collagen-1 concentration for cell adhesion and increasing alginate concentrations for storage modulus control. Robotic liquid handling pipettes microlitre volumes of the interpenetrating network into PEG and the matrix is thermodynamically gelled. Alginate is ionically crosslinked with calcium ions and PEG is replaced with conditioned media as the final step.

2.2 Materials and Methods

2.2.1 Materials

Dulbecco’s modified eagle’s medium x1, acetic acid, sodium hydroxide, phosphate buffered saline, sodium alginate, poly(ethylene glycol) (PEG) (35K), calcium chloride, dimethyl sulfoxide

(DMSO), paclitaxel, pluronic F-108, paraformaldehyde, Triton X-100, Hoechst 33258, phalloidin, ultra-low attachment 96 well flat bottom plates, and goat serum were purchased from Sigma Aldrich (Oakville, ON). Antibiotic antimycotic, type I collagen (5mg/mL), Calcein AM, and ethidium homodimer-1 were purchased from Life Technologies (Carlsbad, CA, USA). HyClone fetal bovine serum, 0.25% trypsin-EDTA, HyClone phosphate buffered saline, cell culture treated 96 well flat bottom plates, and UltraPure distilled water were purchased from Fisher Scientific (Ottawa, ON). Anti-Ki67 antibody and goat anti-rabbit IgG were purchased from Abcam (Cambridge, UK). Dextran (500K) was purchased from Dextran.ca.

2.2.2 Cell culture

HS-5 human fibroblast cell lines and MDA-MB-231 epithelial adenocarcinoms cell lines (ATCC) were cultured in DMEM supplemented with 10% fetal bovine serum (FBS) and 1% antibiotics-antimycotics, and maintained at 37 °C, 5% CO_2. Cells were routinely passaged for seeding experiments or re-plating using 0.25% trypsin-EDTA.

2.2.3 Microgel printing

All handling was carried out under sterile conditions. A dextran-rich gel solution was prepared on ice by adding the following reagents in sequence to a 1.5mL Eppendorf tube: 3mg/mL collagen, diluted down from 5mg/mL in 20mM acetic acid, 1M sodium hydroxide, 10x PBS, 15% dextran dissolved in distilled water, distilled water, alginate of desired concentration, and cell suspension in PBS (see Table 1 for volumetric mixing recipes). Cells were added in a PBS suspension to prevent premature calcium addition and alginate gelation. The solution was mixed by pipetting, taking care not to create air bubbles. A PEG-rich mixture was also pre-prepared by diluting a 6 wt% PEG solution in PBS with distilled water at a 9:1 PEG solution: water ratio. A PIPETMAX® (Gilson) automated liquid handling system was loaded with reagents and programmed to dispense the PEG-rich mixture and dextran-rich droplets into plasticware. 96-well plates adhesive to adherent cells were used for standard culture experiments, and ultra-low attachment plates were used for collagen contraction experiments. PEG was dispensed into each well of a 96 well plate, followed by a drop of the dextran rich gel solution. Plates were then removed from the PIPETMAX® and gels were incubated at 37 °C for 45 minutes. Calcium chloride was added to all cultures for 5 minutes, at an ~1000x molar excess for alginate crosslinking (0.1 wt%) to saturate crosslinking sites. Calcium was allowed to diffuse for 5 minutes to allow complete alginate crosslinking. Given that maximal diffusion distances are less than 1 mm, small molecules such as calcium, equilibrate near-instantaneously, based on experimental results and computational models previously developed.[215] Samples were either aspirated by hand or serially diluted to replace the PEG media with supplemented media, and cultured at 37 °C, 5% CO_2 during experiments.

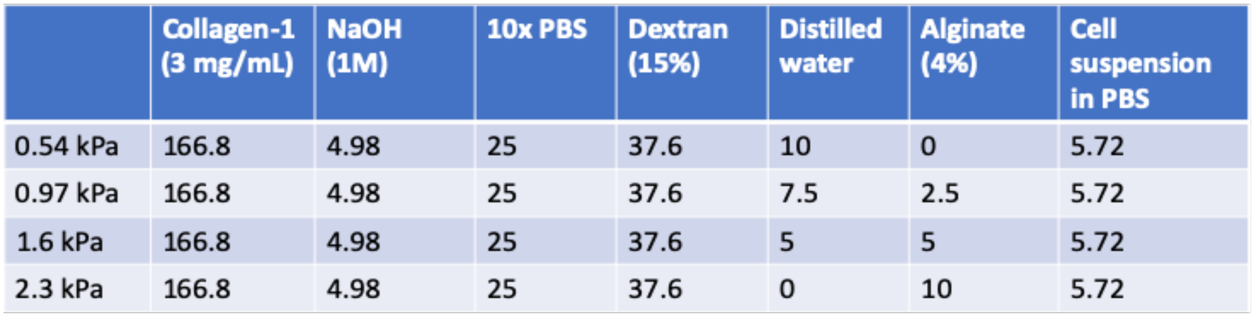

	Collagen-1 (3 mg/mL)	NaOH (1M)	10x PBS	Dextran (15%)	Distilled water	Alginate (4%)	Cell suspension in PBS
0.54 kPa	166.8	4.98	25	37.6	10	0	5.72
0.97 kPa	166.8	4.98	25	37.6	7.5	2.5	5.72
1.6 kPa	166.8	4.98	25	37.6	5	5	5.72
2.3 kPa	166.8	4.98	25	37.6	0	10	5.72

Table 1 Microgel recipes. Volumes are presented as µL.

2.2.4 Scanning electron microscopy

IPNs were gelled in 250 µLvolumes, rather than using the ATPS method to allow more surface area for handling and imaging. Gels were snap frozen in liquid nitrogen for 1 minute, and lyophilized overnight. Dehydrated ECM was then peeled back with tweezers to uncover more central gel architecture and imaged using a scanning electron microscope (SEM, SU3500, Hitachi Hi Technologies, Tokyo, Japan). Observations were performed under variable-pressure imaging mode (3.0 kV, 30 Pa).

2.2.5 Shear Modulus measurements

150 µL of gel prepolymer was dispensed into 35 mm glass bottom petri dishes containing 1mL of 6 wt % PEG and gelled at 37 °C for 45 minutes. Calcium chloride was then added at a final concentration of 0.1wt% to each dish for 15 minutes to crosslink the alginate. The PEG/calcium chloride suspension was replaced with 1 mL PBS, and left to swell overnight at 4 °C. To mechanically probe the hydrogel at length scales relevant to individual cells, twisting magnetic

cytometry was used to measure the micro-scale shear moduli of the gels and this method is discussed elsewhere. [142] Briefly, a ferromagnetic bead 4.5 µm in diameter was depressed into the surface of the gels and subjected to an external magnetic field. This magnetic field caused the beads to oscillate, and the displacement of the beads was used to calculate the shear modulus of the gel.

2.2.6 Cell viability

HS5 viability in 3D gels was examined at day 9 after seeding cells at a density of 250 cells/ µL and MDA-MB-231 viability was examined at day 5 after seeding cells at a density of 200 cells/µL. Viability was visualized by live/dead staining the cells with 2 µM calcein AM and 2 µM ethidium homodimer in supplemented media before image collection.

2.2.7 Cell morphology

To study 2D cell morphology on gel surfaces, 40 µL of cell-free hydrogel IPN solution was added to well in a 96 well plate, gelled at 37 °C, 5% CO_2 for 45 minutes followed by alginate crosslinking with 0.1 wt% $CaCl_2$ for 15 minutes. Subcultured HS-5 cells were suspended in supplemented media at low densities of 70 cells/µL, and 50 µL were added to each well. Cells were allowed to attach and spread for 24 hours. Gels were fixed in 4% paraformaldehyde, permeabilized with 0.1% Triton-X and stained with 0.5 µg/mL phalloidin and 1 µg/mL Hoescht to view the F-actin cytoskeleton and nucleus respectively.

HS5 and MDA-MB-231 morphology in 3D ATPS printed microgels was analyzed at day 3 after seeding cells at a density of 125 cells/ µL to view single cell morphology before gel contraction. HS5 morphology was also analyzed at day 9 after an initial seeding density of 1000 cells/ µL to view overall tissue architecture following contraction. Gels were fixed in 4% paraformaldehyde, permeabilized with 0.1% Triton-X and stained with 0.5 µg/mL phalloidin and 1 µg/mL Hoescht to view the F-actin cytoskeleton and nucleus respectively.

2.2.8 Microgel contraction analysis

HS-5 cells were printed into 1 µL microgel droplets at a density of 1000 cells/ µL and incubated with either FBS free media, FBS supplemented media, or FBS supplemented media containing 5 ng/mL of TGFβ-1 at 37 °C, 5% CO_2. Microgels were allowed to contract for 6 days and brightfield images of contracting microgels were taken every 24 hours. Media was exchanged every 48 hours.

2.2.9 Drug responsiveness and proliferation analysis

MDA-MB-231 cells were printed into the gels at a density of 200 cells/ µL and incubated with supplemented media at 37 °C, 5% CO_2 for 3 days to allow spreading. For drug responsiveness studies, gels were then treated with 0.1, 1 or 150 µM Paclitaxel in supplemented media. Control gels were given the matched volume of the vehicle (DMSO). After 48 hours cell viability was examined by replacing media with 2 µM calcein AM and 2uM ethidium homodimer in supplemented media. For proliferation studies, gels were fixed on day 3 in 4% paraformaldehyde, permeabilized with 0.5% Triton-X, blocked with 2.5% goat serum, incubated with 1/1000 dilution of Ki67-rabbit antibody, rinsed twice with PBS, blocked again with 2.5% goat serum, incubated with 1/100 dilution of goat-anti rabbit secondary antibody.

2.2.10 Image and Statistical analysis

Fluorescent, brightfield, and phase-contrast images were collected on an Olympus microscope (IX73, using Metamorph software). Percent void space was quantified by applying a consistent threshold value across all images, selected to visually separate the matrix from the background. Area fraction was then measured in ImageJ. All gel areas and cell spread areas were quantified by carefully tracing the outside of the gel or cell using the freehand selection tool in ImageJ software and collecting area from the measurements tab under "Analyze". Gel circularity was also retrieved in this manner. Cell aspect ratio was collected using the bounding rectangle measurement in ImageJ software. F-actin fluorescent intensity was quantified by sampling the mean gray value of $130 \mu m^2$ sections within each microgel using the ImageJ analyze tool, while maintaining consistent staining and imaging parameters. Cell viability and Ki67 staining were both quantified by applying a consistent threshold value across all images, inverting the image, and collecting analyzed particles.

Prism v8.2 (GraphPad Software, San Diego, CA) statistical analysis software was used to calculate one-way ANOVAs between treatment groups, followed by a Tukey post-hoc test, carried out at 95% significance. Each well was considered independent for all experiments.

2.3 Results

2.3.1 Characterization of printed collagen-alginate IPNs.

Microgel formulations with equivalent collagen content and alginate concentrations ranging from 0 to 1.6 mg/mL were printed at volumes ranging from 0.1 μL to 2 μL (Figure 2.2A). Volumes larger than 2 μL are also capable of being printed (data not shown). Holding the concentration of collagen constant across the gels controls for binding ligand availability, ensuring that only one variable (storage modulus) is changing at a time. This is important, as it allows the decoupling of stiffness and binding ligand density: two independent drivers of cell behaviour.[236] In using alginate concentration to tune stiffness, alginate crosslinking sites were saturated by exposing microdroplets to excess calcium ions. Due to outside-in alginate crosslinking as calcium ions diffuse, calcium crosslink instability over multiday culture periods,[234] and cell release of calcium into surrounding culture,[237] saturating alginate crosslinks should provide a uniform and stable mechanical profile within the gels. Printed droplets form consistently sized microgels, based on projected area and droplet circularity (Figure 2.2B,C). Occasional irregularities and gel folding occurs due to media movement during plate handling and can be avoided with careful plate transport before collagen gelation or by gelling on a thermally controlled stage. While the 0.1 μL droplets do demonstrate the low volumes possible with the ATPS technique, some variation was observed at 0.1 μL print volumes, likely because the Pipetmax printing platform is calibrated to reproducibly dispense print volumes greater than 1 μL. Uniformity can hence be improved even at these small volumes by using appropriately rated liquid handling tools. Further, microgels are able to either securely stick to the bottom of the well, or remain free floating in the media depending on the desired application by selecting appropriate plasticware. Bioprinting the microgels into standard plates used for adherent cell culture allows gels to remain adhered on the plastic surface, even after multiple washes in media. In contrast, microgels bioprinted into ultra-low attachment wells results in free floating gels. Plasticware can therefore be selected based on the desired application, allowing further flexibility in using this technique.

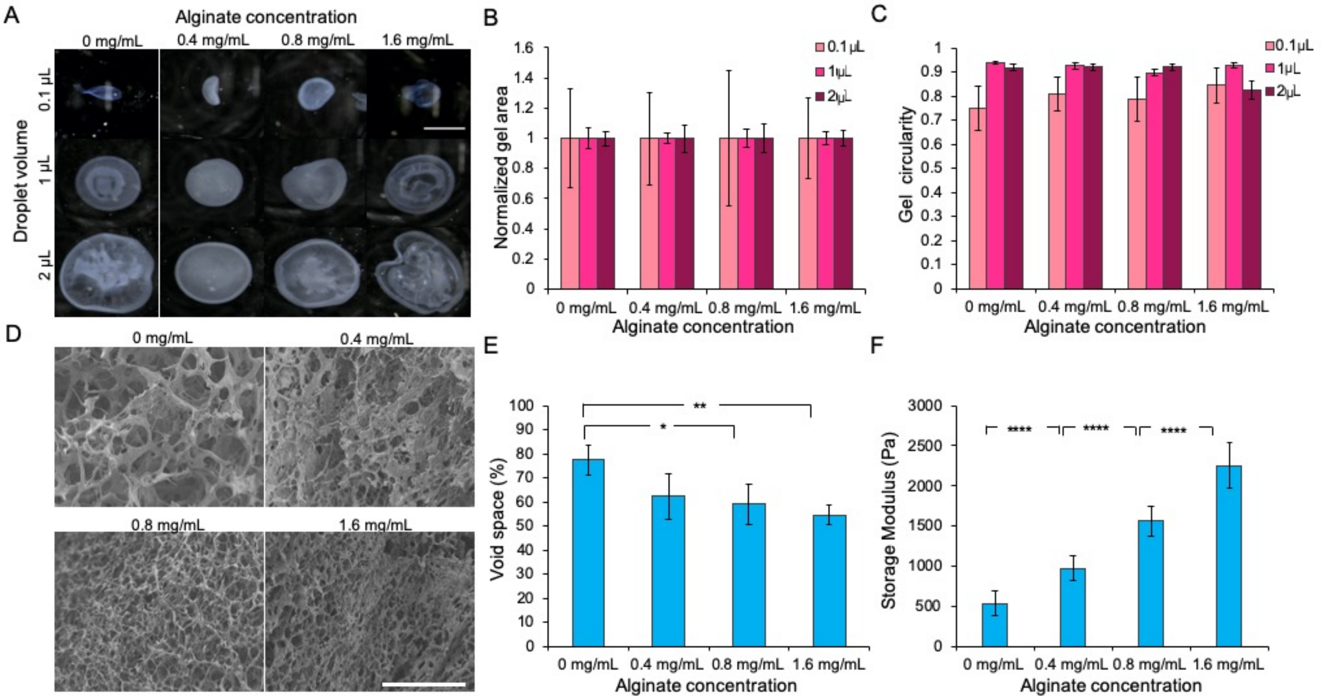

Figure 2.2 Characterization of printed microgels. (A) Microprinted droplets at different volumes and alginate concentrations; Scale: 1 mm. (B) Areas of microprinted droplets at different volumes and alginate concentrations. Areas have been normalized to the average area printed by each corresponding pipette head. (C) Circularity of microprinted droplets at different volumes and alginate concentrations. (D) Scanning electron microscopy images of matrices with increasing concentrations of alginate; Scale: 50 µm. (E) Percent void space of matrices, as a measure of porosity. (F) Storage moduli of matrices, as assessed by optical magnetic twisting cytometry. Data presented as mean +/- standard deviation; (E): n = 3; (F): n= 3 gels, minimum of 30 measurements per gel; * $p < 0.05$; ** $p < 0.01$; ****$p<0.0001$, by one-way ANOVA with Tukey post-hoc analysis.

As alginate concentration increases within the matrix, pore structure changes, causing total void space to decrease, as evidenced by SEM images of the printed hydrogels (Figure 2.2D,E). This is expected, as the total polymer concentration increases with increasing alginate content; but it is important to note that cell-adhesive collagen content remains constant across all conditions. We then verified that by changing the concentration of alginate in the IPN, the storage moduli of the microgels could be tuned. Storage moduli of cell-free IPNs ranged from 0.54 ± 0.15 kPa to 2.3± 0.28 kPa between 0 mg/mL and 1.6 mg/mL of alginate (Figure 2.2F). As storage moduli are subject to change during cell remodelling, only initial mechanical properties are referred to throughout this work. Loss moduli also increased with alginate concentration (Figure 2.3 B), resulting in a consistent elastic to viscous ratio (or phase angle; Figure 2.3C) between all microgel formulations. Phase angle influences gene expression and inflammatory secretion of mesenchymal stem cells,[178] and was hence controlled for in these experiments. The successful production of microlitre matrix volumes via robotic liquid handling, combined with the flexibility to provide robustly tunable mechanical properties suggests the possibility of a high-throughput 3D, stiffness-tunable culture platform through compatibility with existing high throughput liquid-handling infrastructure.

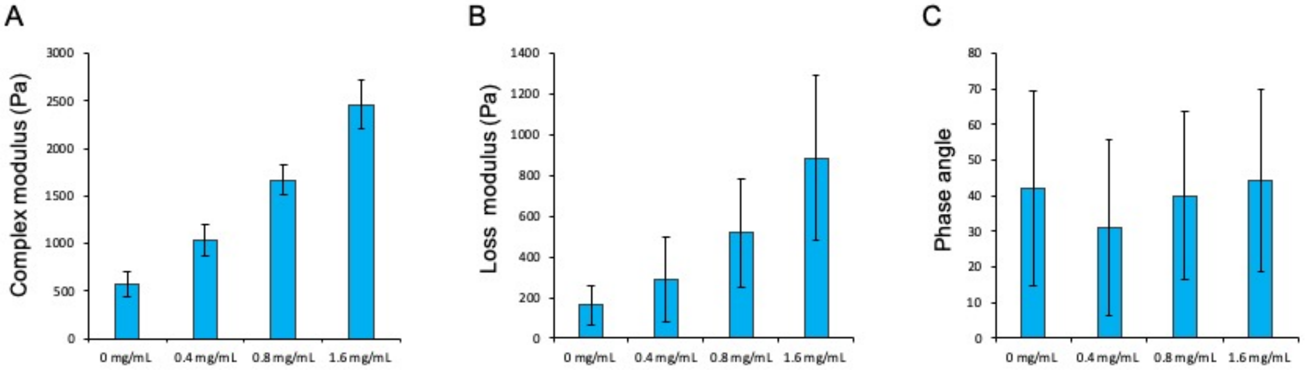

Figure 2.3 Complex moduli, loss moduli, and phase angle of the matrices. Assessed by optical magnetic twisting cytometry. Data presented as mean +/- standard deviation; n= 4 microgels per condition.

2.3.2 Microgel stiffness influences cell morphology

Cell viability of HS-5 fibroblasts immediately following bioprinting was over 95% (Figure 2.4). Cultured separately, fibroblasts and MDA-MB-231 breast cancer cells displayed high viability for up to nine and five days in culture respectively (Figure 2.5A,B), at both low (125 cells/ µL) and high cell densities (1000 cells/ µL), demonstrating the platforms utility for longer culture periods and versatile cell densities. The ability to print 3D cultures with as few as 10-100 cells in each sample may have strong potential in personalized medicine applications for which patient cells are both precious and limited.

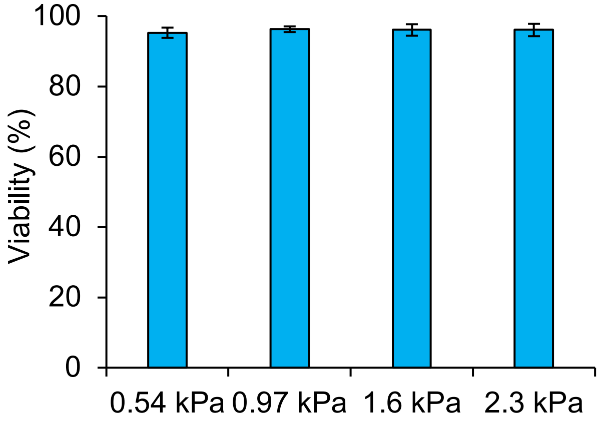

Figure 2.4 HS-5 viability on day 0 immediately following bioprinting. Data presented as mean +/- standard deviation; n =3 microgels per condition.

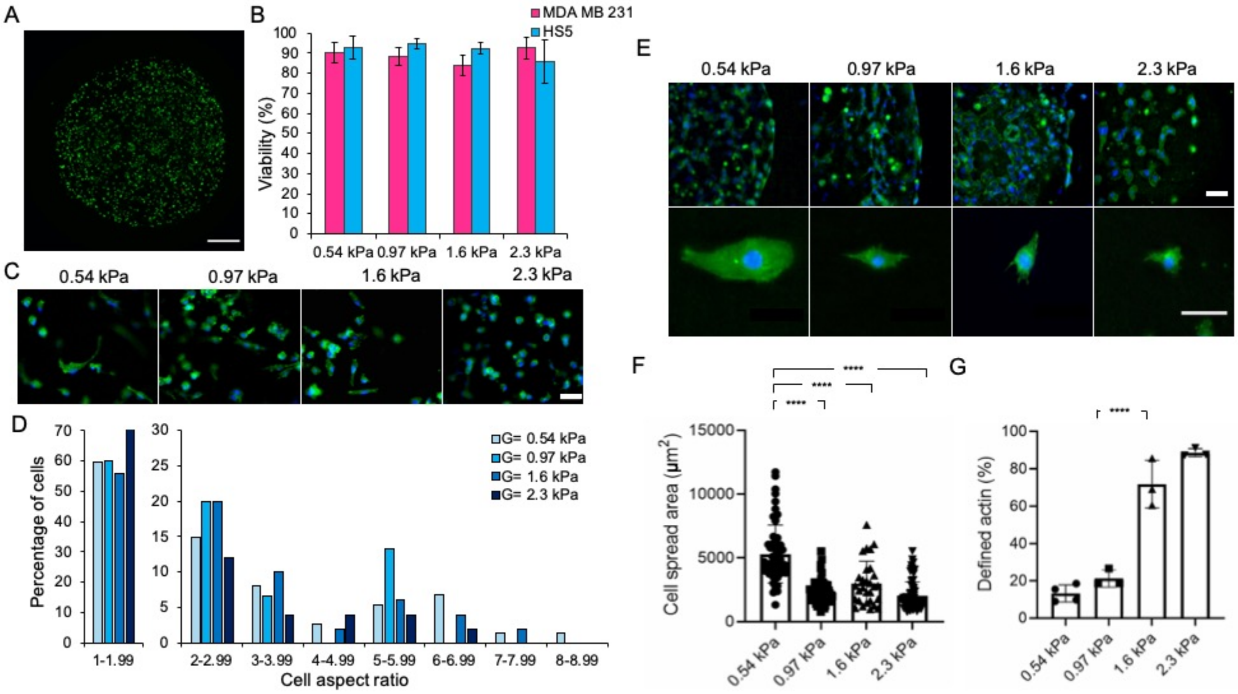

Figure 2.5 Morphological characterization of breast cancer cells and fibroblasts in stiffness-tunable microgels. (A) Representative calcein AM (live) and ethidium homodimer (dead) stain of a 0.97 kPa IPN containing HS-5 fibroblast cells on day 9. Green: live cell, red: dead cell; Scale: 500 µm. (B) Quantification of MDA-MB-231 breast cancer cell and HS-5 fibroblast viability within the microgels at 5 and 9 days in culture respectively. (C) Morphology of breast cancer cells on day 3 within the microgels of various stiffness and (D) quantitative results of cell aspect ratio. (E) Fibroblast actin architecture, within multicellular tissues at day 9 (top) and single cell fibroblast spread area at day 3 (bottom) of culture within microgels [green: F-actin, blue: nuclei, scale: 50µm]. Quantitative results of (F) single cell spread area and (G) average F-actin fluorescent intensity per 130µm^2. Data presented as mean +/- standard deviation; (B): n=3 microgels (D): n=3 microgels, 10-30 cells each (F): n=6-12 microgels, 28-84 cells each; (G): n=3 microgels, 3-4 areas each; $**p < 0.01$; $**** \ p < 0.0001$ by one-way ANOVA with Tukey post-hoc analysis.

The morphological behaviours of both HS-5 and MDA-MB-231 cell types are well-established, making them ideal candidates to investigate morphology within the microgels. Cell morphology throughout the microgels was readily measured using conventional epifluorescent imaging, as the droplets are sufficiently small to present no challenges in imaging using standard longworking distance objectives. Breast cancer cells displayed two major morphologies (rounded or spindle-shaped) within all four test conditions, giving rise to highly heterogeneous cell aspect ratios (Figure 2.6). The proportion of spindle-shaped versus rounded breast cancer cells skewed towards rounder cells with increasing initial stiffness (Figure 2.5C,D). Similarly, high initial microgel stiffness limited spread area of the fibroblast cell line (Figure 2.5E,F). Although fibroblasts often took on a spindle-shaped morphology (Figure 2.5E) with similar aspect ratios within the microgels of differing stiffness (Figure 2.7), the spread area decreased considerably in all gels stiffened with alginate (Figure 2.5F). This trend is also noted when fibroblasts are cultured on top of our gels (as in a 2D system), where initially stiffer gels give rise to decreased spread (Figure 2.8). Morphology also differed between 2D and 3D conditions, where fibroblasts cultured on top of the gels visually displayed higher aspect ratio with lower spread area as compared to 3D culture (Figure 2.9), further rationalizing the need for 3D culture when conducting morphological analysis.

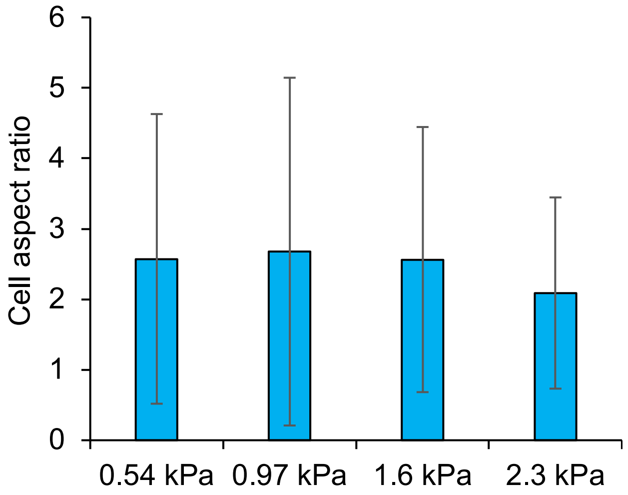

Figure 2.6 Cell aspect ratio of MDA-MB-231 breast cancer cells within the microgels at day 3. Data presented as mean +/- standard deviation; n=3 microgels per condition, 10-30 cells each microgel.

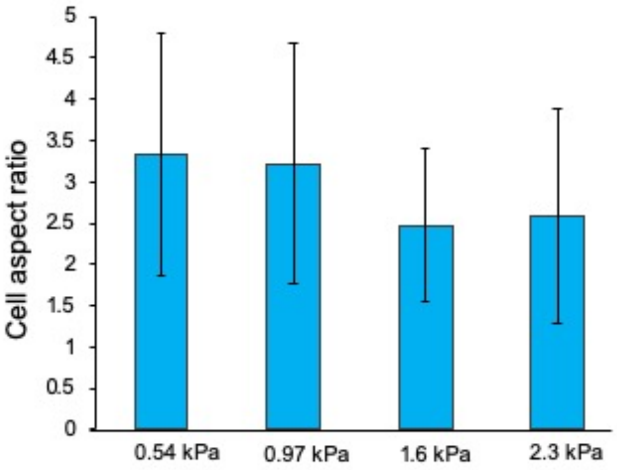

Figure 2.7 Cell aspect ratio of HS-5 fibroblast cells within the microgels at day 3. Data presented as mean +/- standard deviation; n=6-12 microgels per condition, 28-84 cells each microgel.

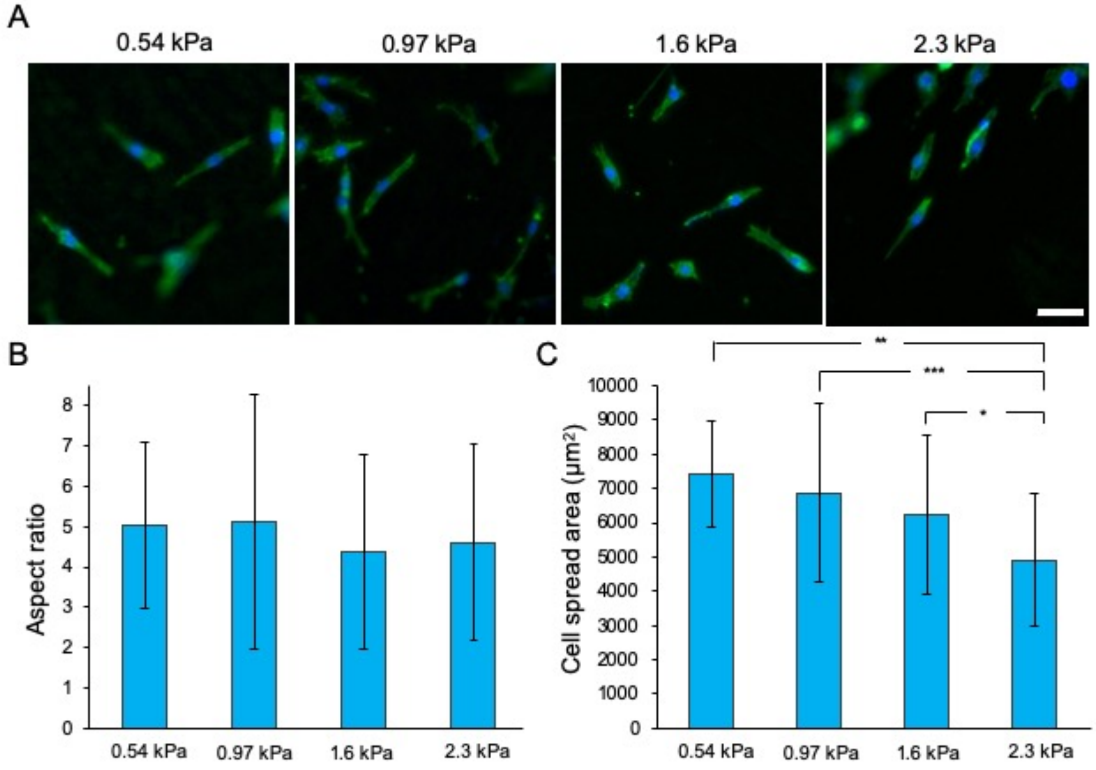

Figure 2.8 HS-5 fibroblast morphology cultured on top of the matrices in 2D. (A) Qualitative images, Green: F-actin, blue: nuclei; Scale: 50 μm. Quantitative results of (B) single cell aspect ratio and (C) spread area. Data presented as mean +/- standard deviation; n = 3 wells, 14-54 cells; * $p < 0.05$; ** $p < 0.01$; *** $p = 0.0001$ by one-way ANOVA with Tukey post-hoc analysis.

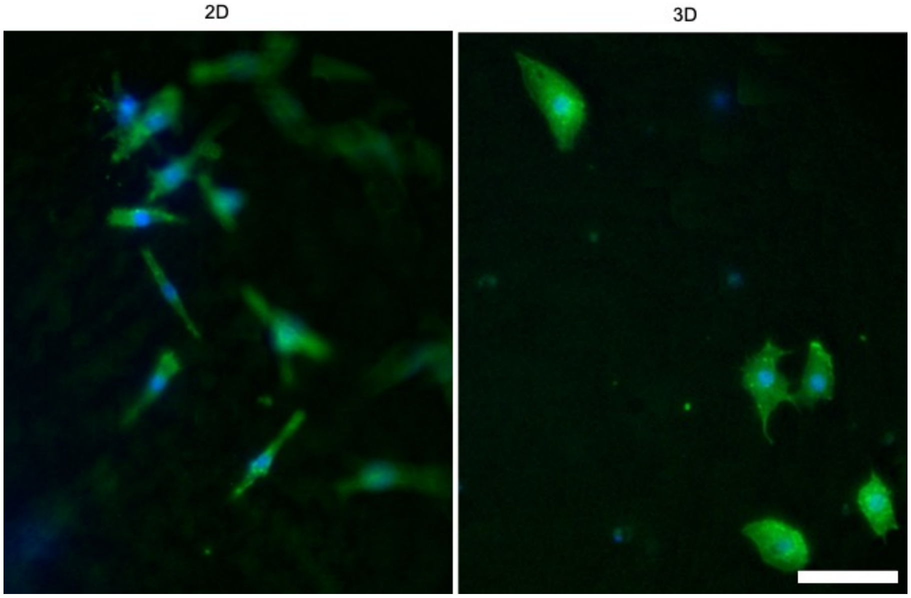

Figure 2.9 2D and 3D HS-5 fibroblast morphology. Cells were cultured on or within 0.54 kPa matrices and were allowed to spread for 24 hours in the 2D condition and 72 hours in the 3D condition, as cells spread faster in 2D. Green: F-actin, blue: nuclei; Scale: 50 μm.

Increased stiffness also promoted well-defined actin structures in fibroblasts, which were much more diffuse in softer microgels (Figure 2.5E,G) (Figure 2.10), consistent with known effects of stiffness on actin fiber formation,[9] [1] and suggestive of a more contractile and mechanically-active phenotype within stiffened matrices.

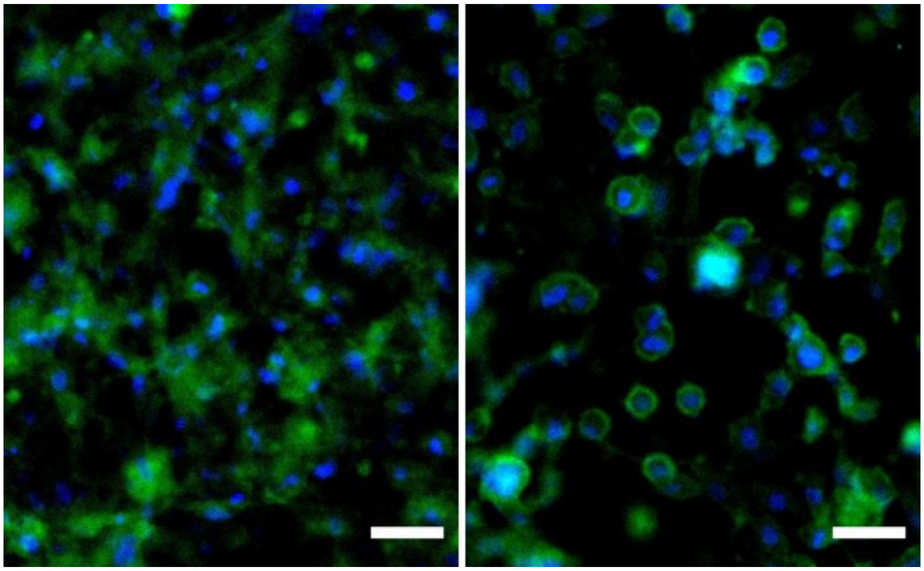

Figure 2.10 F-actin expression as a result of stiffness within 3D microgels. Fibroblasts within a 0.97 kPa microgel (left) and 2.3 kPa microgel (right). Green: F-actin, blue: nuclei; Scale: 50 μm.

2.3.3 Soluble factors can stimulate contractility even in stiffened matrices

Decreases in fibroblast spread area with simultaneous formation of defined architectures suggest opposing effects on contraction of the collagen matrix, a commonly-used assay to assess ECM remodelling.[1] We have previously demonstrated the utility of bioprintable collagen gels as a microscale contraction assay; and noted that small gels allow rapid equilibration of even large-molecular weight soluble factors throughout the gel volume.[215] We hence asked whether tissue contraction was influenced by initial matrix stiffness; and used the small-volume gels to simultaneously understand the effects of soluble cues on this contraction process, using FBS and TGFβ-1 as candidate stimuli, as both are well-established to stimulate cell-driven collagen contraction in culture.[1] In serum-free media, initially soft microgels contracted faster and to a much higher overall contraction within 6 days than initially stiffened microgels (Figure 2.11A), demonstrating that alginate stiffens tissues sufficiently to hinder contraction. However, supplementing the media with FBS was sufficient to induce higher contraction of stiffened tissues, but at a slower rate than initially soft tissues (Figure 2.11B). Further addition of TGFβ-1 prompted no additional contraction, suggesting that factors in serum are sufficient to drive maximal contraction (Figure 2.11C,D).

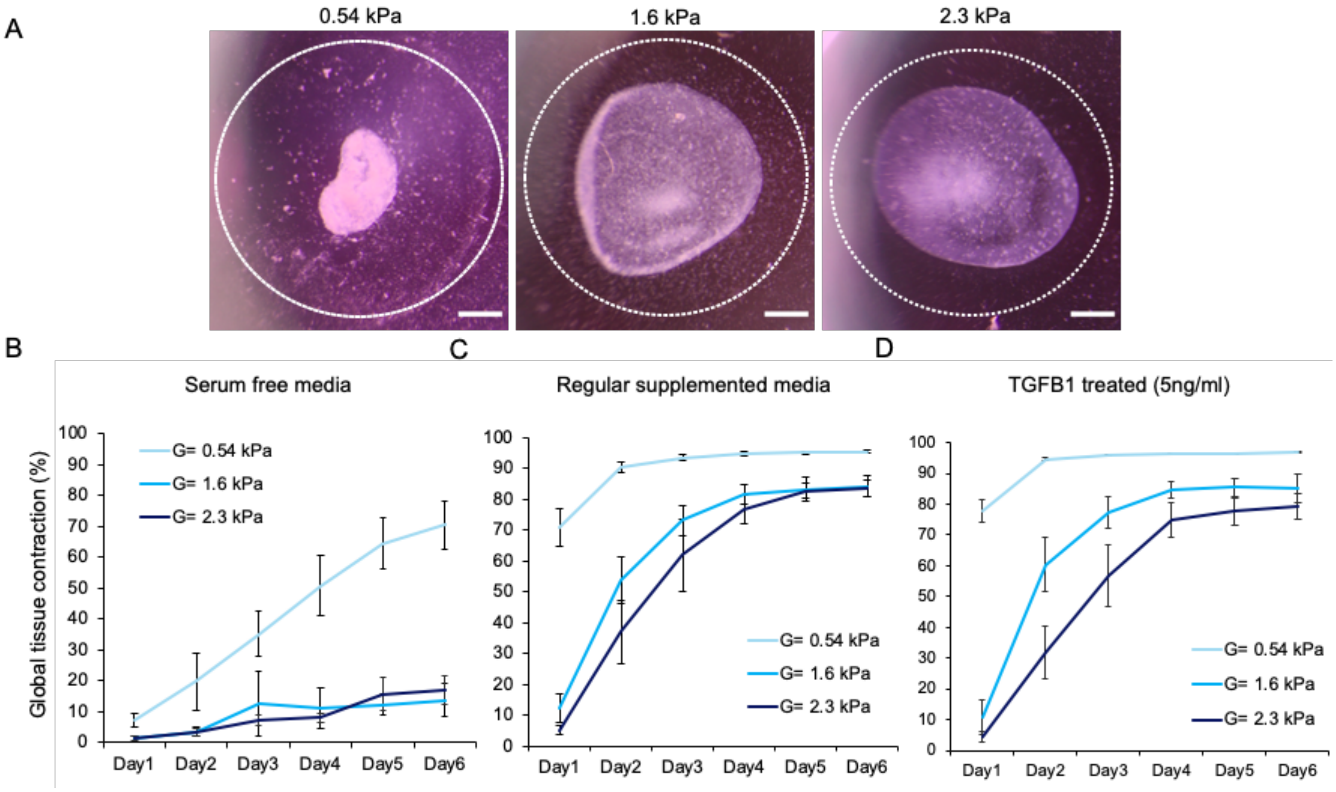

Figure 2.11 Microgel contraction as a function of time under various stiffnesses and soluble factors. (A) Representative contracted microgels at day 2 in regular supplemented media (white dashed line represents microgel at day 0). Overall global microgel contraction time course over 6 days in (B) serum free conditions, (C) FBS supplemented media conditions, and (D) FBS supplemented media + 5ng/mL TGFβ-1 conditions; Scale: 400 µm. Data presented as mean +/- standard deviation; n =6-12 microgels.

This data demonstrates that although the alginate-doped gels are stiffened, they still retain the capacity to be remodelled under appropriate stimulation. It also suggests that contrary to previous suggestions[9] increased tissue stiffness is not sufficient to drive contractile processes in these gels, and that soluble stimuli are still necessary to recreate this phenotype in culture. Whether this holds for a broader range of stiffness is unknown. Additionally, microgel stiffness increases across contraction.[238] As such, microgel stiffness is dynamic and can only be guaranteed immediately following gelation. The change in gel stiffness in real-time, along with how instantaneous stiffness influences cell behaviours such as contraction and proliferation are intriguing questions. More broadly, this experiment demonstrates the utility of the stiffness-tunable bioprintable microgels as a miniaturized collagen contraction assay to simultaneously probe the effects of matrix stiffness and soluble stimuli on this important developmental and disease-related process.

2.3.4 Microgel stiffness influences chemotherapy effectiveness

Given the responsiveness of this platform to soluble factors, we then sought to demonstrate the utility of stiffness-tunable microgels in a more conventional and industry-relevant assay. 3D culture has previously been demonstrated to have a strong protective effect against certain chemotherapeutics, compared to 2D cultures,[27] and 3D stiffness is known to have an effect on chemotherapeutic efficacy.[239] [240] Clinically, patients with low breast tissue stiffness also respond better to chemotherapy than those with high breast tissue stiffness,[241] suggesting that considering stiffness in early drug screening protocols would be an important factor in screening for the next generation of therapeutics. To determine whether stiffness may play a role in this process, and simultaneously demonstrate the utility of this platform for drug-screening, we designed a simple viability-based screen for MDA-MB-231 cells in stiffness-tunable gels against paclitaxel, a well-established chemotherapeutic agent. Breast tissue stiffness spans a shear modulus range from < 1 kPa in healthy tissue, to between 1 kPa and 3 kPa+ at the invasive front of disease.[20] The microgel formulations selected here may therefore model the stiffness evolution that occurs during breast cancer progression.

Breast cancer cells cultured in initially softer gels were more responsive to paclitaxel than cells in the initially stiffest gels, suggesting that increased stiffness has a small but statistically significant chemoprotective effect (Figure 2.12A) (Figure 2.13). Interestingly, this effect was not monotonic with stiffness.

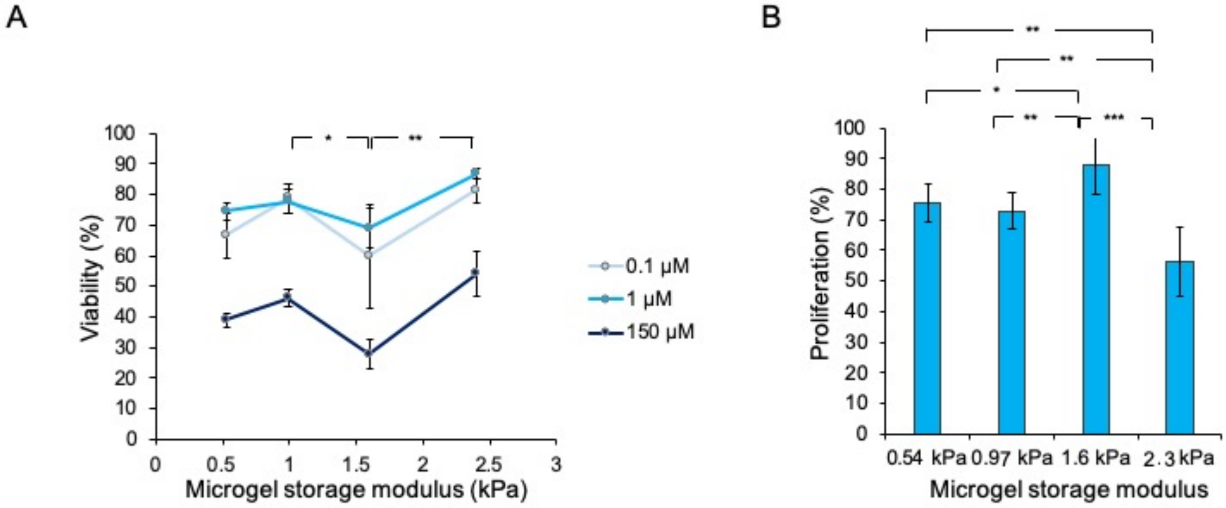

Figure 2.12 Breast cancer cell susceptibility to chemotherapy depends on microgel stiffness. (A) Live/dead analysis following 48 hours of exposure to Paclitaxel at a concentration of either 0.1 µM, 1 µM, or 150 µM. Presented significance reflects the lowest seen significance in 0.1 µM gels and all other concentrations display higher significance. For detailed significance, see Figure 2.13. (B) Ki67 staining of untreated tissues illustrates the total percentage of cancer cells undergoing active proliferation within each microgel. Data presented as mean +/- standard deviation; n =3-6 microgels; * $p < 0.05$; ** $p < 0.01$; *** p= 0.0001 by one-way ANOVA with Tukey post-hoc analysis.

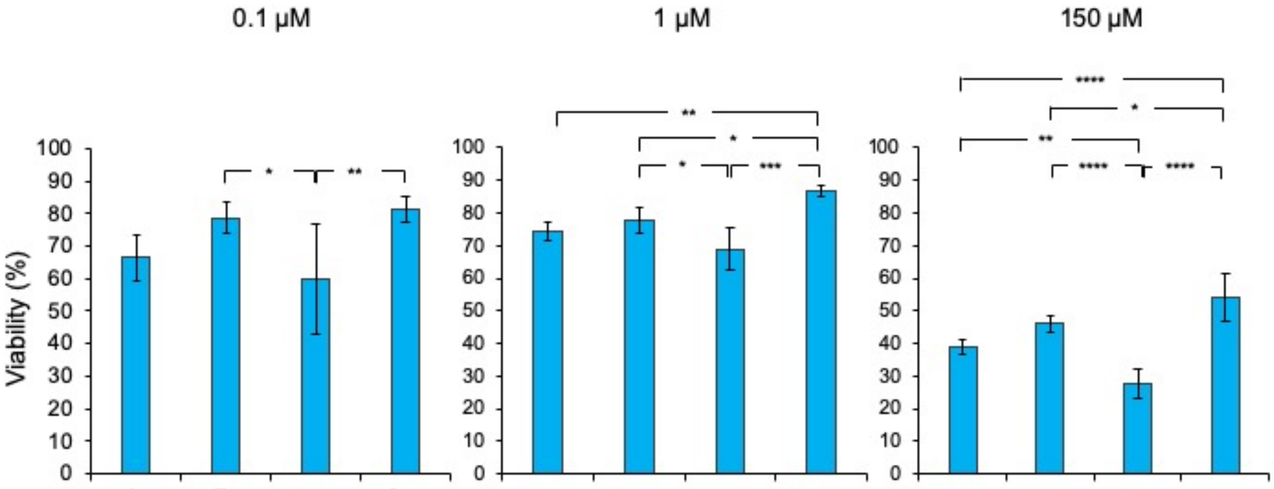

Figure 2.13 Breast cancer cell susceptibility to chemotherapy depends on microgel stiffness (Alternative graph displaying specific significances of live/dead analyses following 48 hours of exposure to Paclitaxel). Data presented as mean +/- standard deviation; n =3-6 microgels; * $p < 0.05$; ** $p < 0.01$; *** p= 0.0001 by one-way ANOVA with Tukey post-hoc analysis.

The initially mid-range 1.6 kPa gels were more sensitive to all concentrations of paclitaxel than were each of the other gels, suggesting that an optimal stiffness exists at which certain drugs can be more effective. Stiffness did not influence viability due to the chemotherapeutic vehicle for delivery (Figure 2.14). As paclitaxel is selectively taken up by proliferating cells,[242] and stiffness is a known factor influencing proliferation,[135] we reasoned that stiffness-induced changes in proliferation may be responsible for this response. We therefore characterized the relative proliferation of cancer cells in this system, and found that increasing stiffness generally is associated with decreased proliferation, except in the 1.6 kPa gels which notably demonstrate the highest proliferative rates of all cultures tested (Figure 2.12B). Hence, differences in proliferation likely underlie the observed phenotypes.

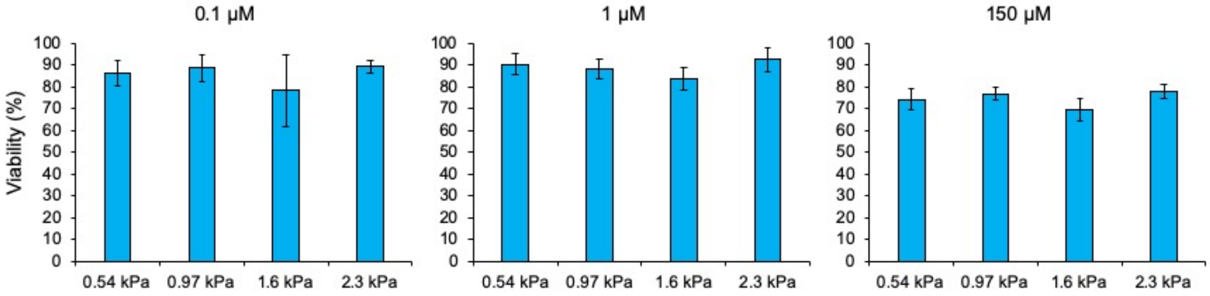

Figure 2.14 Breast cancer cell viability on exposure to chemotherapy vehicle. Live/dead analysis following 48 hours of exposure to DMSO at a concentration of either 0.1 µM, 1 µM, or 150 µM. Data presented as mean +/- standard deviation; n =3-6 microgels.

2.4 Discussion

Blending collagen-alginate IPNs with the PEG and dextran polymers to induce phase separation was shown to support bioprinting microvolumes of stiffness-tunable biomaterials, and was demonstrated here as a robust, increased-throughput method for 3D cell culture capable of multiple biological assays. We specifically focused on morphological analysis of multiple cell types, implementation of a functional collagen contraction assay, and a demonstration of a scalable live/dead viability assay against a commonly used chemotherapeutic. In each of these assays, low biomaterial volumes allow for decreased costs in terms of materials, reduced cell number requirements, and as previously determined,[215] can support faster diffusion and equilibration of soluble factors than bulk gels, allowing dynamic or long-term cell culture studies. Furthermore, both automatable handling using a desktop liquid handling robot, and compatibility with standard fluorescent and brightfield microscopy techniques indicate that these methods can be rapidly adopted by standard wet-labs with this basic infrastructure.

In addition to demonstrating the utility of this system, our experiments also present some interesting findings. As expected, increasing 3D biomaterial stiffness results in decreased cell spreading, but this relationship is not linear with stiffness. Instead, there is a small trend towards increased spread area at the mid-range of stiffness in alginate-doped gels (1.6 kPa), and although not statistically significant, this observation is consistent across multiple repeated experiments, and correlates with statistically significant increases in chemotherapeutic efficacy (Figure 2.12A) and proliferative percentage (Figure 2.12B). Given the well-known relationship between cell spread area and proliferation,[236] [135] and the proliferation-based mechanism of action for paclitaxel,[242] these results are internally consistent and suggest that the increase in spread area at the mid-range of stiffness is a genuine effect. Our observations of increased formation of well-defined F-actin structures due to increased stiffness (Figure 2.10) suggests that the increased matrix stiffness does allow enhanced tension generation at the binding site to increase spread area,[236] but a competing mechanism must be simultaneously restricting spread area, despite the formation of pro-spreading actin structures. This is likely due to recently developed descriptions of ECM fiber recruitment being required to increase local binding ligand density and therefore cell spreading.[53] [233] [44] [231] Hence, our observations support the idea of increased fibrous matrix stiffness hindering the ability of a cell to deform and therefore recruit fibers, while simultaneously providing tension at the binding complex to prompt increases in spread area. Notably, pore size also decreases as stiffness increases and cell confinement also attenuates cell spread.[51] Our data therefore suggests a “sweet spot” of ideal stiffness for maximal cell spreading and proliferation.

Some limitations should also be considered in the use of this culture technology. Although the phase angle is conserved over the range of alginate concentrations tested here, the viscoelastic storage and loss moduli of these matrices cannot be independently controlled. Since viscoelastic characteristics impart important and biologically relevant cues in culture, future work should consider incorporating the tunable viscoelastic properties of alginate in modifying the collagen mechanical properties. Second, although our OMTC measurements do provide a measure of cellular-scale rigidity within the materials, we only perform these prior to cell seeding. As collagen gels are well established to stiffen during contraction,[238] [243] [244] these remodelled matrices likely effect cell functions differently. The effects of cell spreading and contraction on highly local mechanical properties within the matrix are unclear, and studying the effects of these dynamic properties, particularly using a variety of novel techniques to characterize stresses and mechanical properties within 3D matrices at this cellular length scale,[198] [144] [245] could provide valuable future insight into cell-environment interactions. Finally, while the ATPS technique is compatible with standard liquid handling tools, adoption into standard workflows will require careful characterization of the effects of PEG and dextran on the specific biological assay being developed.

2.5 Conclusions

The present platform provides the ability to tune 3D culture stiffness, while bioprinting directly into well-plates for high-throughput screening applications using readily-available liquid handling tools. Hence, this platform may easily be adopted for a variety of applications requiring high-throughput culture, and may be particularly beneficial for those involving limited or rare cell populations, multiple culture conditions, and testing of secreted or soluble factors; such as drug screening, personalized medicine, organoid formation, and stem cell differentiation, each of which have significant stiffness-related effects. Our findings highlight the importance of using stiffness-tunable 3D culture models in fundamental biological discovery, and simultaneously provide accessible strategies to achieve this.

Chapter 3

Free boundary area of collagen microtissues affects contraction strain rate

The following chapter addresses the second thesis objective by adapting the tissue contraction platform engineered in chapter 1 to tune tissue geometry using a thermal-based bioprinting technique. It then explores how free boundary area along the tissue periphery influences global tissue strain during contraction. Here, I explain the rationale behind the technique's design, describe the methods involved in free boundary area control and biological readouts, and discuss the important research findings of tissue free boundary area in driving global tissue strain.

Abstract

Tissue contraction drives essential physiological and pathological processes such as embryonic development, wound healing, disease-associated tissue stiffening and fibrotic scarring. Contractile cells respond to their mechanical microenvironment and overall tissue shape creates unique mechanical niches within the tissue. Moreover, many cells have the capacity to sense tissue boundaries in both 2D monolayer and 3D fibrous cultures, and can orient themselves relative to these boundaries, demonstrating unique behaviours at the tissue interface. Here, we demonstrate that collagen tissue contraction is influenced by tissue surface effects and follows an outside-in contractile phenotype where the tissue edge densifies and exhibits local strain before compacting the tissue interior. To determine whether this process might be important in evaluating collagen tissue contraction, a new technique was developed using gelation temperature to tune microgel free boundary area, while keeping all other culture parameters consistent. These experiments establish that high free boundary area increases contraction strain rates, likely due to fibroblast organization along the tissue perimeter, elongating parallel to the interface and forming a concentric ring of F-actin around the circumference of the tissue. These results are important in demonstrating a fundamental biological aspect of contraction, and in identifying a novel parameter that should be considered in performing standard contraction assays as an *in vitro* biological test.

3.1 Introduction

Tissue contraction is a fundamental cellular driven process involved in various distinct events such as tissue development, homeostasis, and disease progression. Embryonic and later stage organ formation rely on contractile cells to remodel the extracellular matrix (ECM) during developmental morphogenesis [2]. Tensional homeostasis is required within many tissues in the body, and cellular contraction is a key mechanism for tension regulation and maintenance [246]. Wound closure relies heavily on myofibroblast contraction [247], and prolonged presence of contractile myofibroblasts is the major known cause of fibrotic disease such as lung and liver fibrosis [3]. Hence, understanding the cellular cues that drive and regulate tissue contraction could benefit *in vitro* model designs and downstream disease therapies.

Global tissue geometry determines tissue surface area and curvature of tissue edges, giving rise to mechanical stress and soluble signal gradients, as well as cellular contact guidance, that allow for unique microenvironments that drive cell morphology and behaviours [4 8 35]. For example, sheets of breast epithelial cells cultured on square islands show α-smooth muscle actin expression exclusively at the corners and edges, but not within the central regions when exposed to TGF-β [10]. Cancer stem cell markers are also preferentially expressed around the perimeter of micropatterned islands of various shapes, and in locations with simulated high stress [73]. Moreover, breast epithelial tissues within a 3D matrix show branching morphogenesis in exclusive locations within a global tissue shape, such as the ends of punctuated tubules [35] and invasive breast cancer cells will preferentially invade from these punctuated ends, associated with regions of high mechanical stress [8]. These interfacial effects are dependent on intracellular contraction, as treatment with contractile inhibitors often abolishes the patterns seen [10 8]. Regarding fibroblasts specifically, these cells are activated into a myofibroblast phenotype at the edges of tissue [248], demonstrating that surface effects are crucial within contractile tissues. However, the impact of these surface effects on global tissue strain is undefined.

Tissue stiffness is another mechanical cue with documented influences over cellular contraction [3]. We previously determined that stiffened 3D, fibrous microtissues contract slower [249]; however, how stiffness regulates surface effects during global contraction is unexplored.

To study tissue contraction using a stiffness-tunable increased throughput platform, we previously designed an aqueous two-phase system (ATPS) that allows microliter volumes of cell-seeded, alginate-doped, collagen-1 matrix to be autonomously bioprinted using robotic liquid handling and subsequently gelled [249]. Tissue baseline stiffness is tuned by changing alginate concentration within the interpenetrating network (IPN) [249], and by using calcium ions to crosslink the alginate, viscoelastic matrix properties are maintained, allowing the tissue to be remodelled and compacted [234].

To introduce a method for free boundary area control, while maintaining a consistent tissue volume, the use of temperature to control gelation speed was considered. Since liquids spread on flat surfaces, it was thought that controlling the degree of spreading would be possible by adjusting the surrounding temperature during gelation.

In this work, local remodelling was investigated during tissue contraction to view spatial differences in tissue densification as a result of contraction. Free surface boundary area of the tissue was then modulated within our previously designed and characterized platform using a thermal-based printing technique to view the roles of stiffness and boundary area on spatial contraction patterns and tissue contraction rates.

3.2 Materials and Methods

3.2.1 Materials

Dulbecco's modified eagle's medium x1, sodium hydroxide, phosphate buffered saline, sodium alginate, poly(ethylene glycol) (PEG) (35K), tetramethylethylenediamine (TEMED), fluorescein o-methacrylate, dimethyl sulfoxide (DMSO), calcium chloride, paraformaldehyde, kerosene, Triton X-100, Hoechst 33258, phalloidin, ultra-low attachment 96 well flat bottom plates, and Corning type 1 collagen (3mg/mL) were purchased from Sigma Aldrich (Oakville, ON). HyClone fetal bovine serum, 0.25% trypsin-EDTA, HyClone phosphate buffered saline, cell culture treated 96 well flat bottom plates, and UltraPure distilled water were purchased from Fisher Scientific (Ottawa, ON). Ammonium persulfate (APS), acrylamide, and bisacrylamide were purchased from Bio-rad Laboratories. Antibiotic antimycotic was purchased from Life Technologies (Carlsbad, CA, USA). Dextran (500K) was purchased from Dextran.ca. Polyglycerol polyrincinoleate surfactant (PGPR 4150) was purchased from Palsgaard. SulfoSANPAH was purchased from GBiosciences.

3.2.2 Cell culture

HS-5 human fibroblast cell line (ATCC) was cultured in DMEM supplemented with 10% fetal bovine serum (FBS) and 1% antibiotics-antimycotics, and maintained at 37 °C, 5% CO_2. Cells were routinely passaged using 0.25% trypsin-EDTA.

3.2.3 Microgel printing

Microgels were bioprinted following established protocols [249]. Briefly, a collagen-1 (2 mg/ mL final concentration) pre-gel solution containing either 0, 0.4, 0.8 or 1.6 mg/ mL of sodium alginate, as well as a high concentration of dextran (2.26 mg/ mL final concentration) was dispensed into a PEG rich suspension. The dextran and PEG rich mixtures maintain phase separation between the liquids and allow microtissue gelation with a liquid-liquid interface. A PIPETMAX® (Gilson) automated liquid handling system was loaded with reagents and programmed to dispense the PEG-rich phase and dextran-rich droplets into ultra-low attachment 96 well plates. Tissue droplets were bioprinted at 2 µL volumes. Plates were then removed from the PIPETMAX® and pre-gels were incubated at 37 °C for 45 minutes to gel the collagen. Calcium chloride was then added to all cultures for 5 minutes, at an ~1000x molar excess for alginate crosslinking (0.1 wt%) to saturate crosslinking sites. PEG was then aspirated by hand, replaced with supplemented media, and samples were cultured at 37 °C, 5% CO_2 during experiments.

3.2.4 Microgel free boundary area control

Microgels were bioprinted into 4 °C PEG on a chilled stage for large free boundary area prints, while room temperature PEG was used for low area prints. Large free boundary area microgels were printed first into cold PEG and then immediately incubated at 37 °C, 5% CO_2 after printing to gel, while the chilled stage was also placed at 37 °C for 10 minutes for rapid warming. Well plates containing room temperature PEG were then set on the stage of now mildly higher temperature and bioprinted. Low area microgels were then incubated at 37 °C, 5% CO_2 to gel.

3.2.5 Microgel contraction

HS-5 cells were seeded into tissues at a density of 1000 cells/ µL. Gels were then incubated with FBS supplemented media at 37 °C, 5% CO_2.. Microgels were allowed to contract for 6-9 days depending on the experiment. To measure local strain, fluorescent beads approximately 50 µm in diameter were added at a final concentration of 1 bead/ µL providing 1-3 beads per tissue on average. This low concentration allowed the displacement of individual beads to be followed over time with the large and heterogeneous strains seen. Brightfield images of contracting microgels were taken every 24 hours, along with matched fluorescent images of the beads. Cultures were then placed back into 37 °C, 5% CO_2 conditions for continued contraction.

3.2.6 Fiducial hydrogel marker fabrication

Fluorescent beads used were fabricated following established protocols [198]. Briefly, polyacrylamide hydrogel microspheres were formed by polymerizing polyacrylamide using a phase separation emulsion technique. Polyacrylamide pre-polymer was added to a kerosene suspension and immediately vortexed, producing the microspheres sensors. Sensors were washed multiple times, first with fresh kerosene and then with PBS. Sensors were allowed to swell to equilibrium overnight at 4 °C in PBS and were then functionalized with a 0.05 mg/mL solution of collagen I (3mg/mL). Polyacrylamide recipe used provided a sensor stiffness of 60 Pa.

3.2.7 Cell morphology

HS-5 morphology in 3D microgels was analyzed at day 9 to view F-actin tissue architecture. Microgels in this experiment were printed into cell-adhesive well plates, and as such, tissue contraction was slower. Gels were fixed in 4% paraformaldehyde, permeabilized with 0.1% Triton-X and stained with 0.5 μg/mL phalloidin and 1 μg/mL Hoescht to view the F-actin cytoskeleton and nucleus, respectively.

3.2.8 Image acquisition and analysis

Fluorescent and brightfield images were collected on an Olympus microscope (IX73, using Metamorph software). Tissue darkness line plots were produced using the line tool in Image J software and drawing a line from the tissue centroid to the tissue edge. Mean grey value along the line was then analyzed. Brightfield mean gray value is low when darker and high when lighter, therefore all brightfield values were inverted by applying the mathematical formula of (value-1)* -1, to provide a high mean gray value being equivalent to a dark location. Local strain was calculated by analyzing the displacement of fluorescent beads from day 0 to day 2. Bead locations within the tissue were measured in relation to their distance from tissue centroid, found by tracing the circumference of the tissue and using ImageJ software to calculate the centroid. Distances were internally normalized to the diameter of each specific microtissue. Microtissue areas were collected by tracing the circumference of each tissue and using ImageJ software to calculate the area. Global contraction analysis was calculated as a percent contracted area from day 0 for each individual tissue.

3.2.9 Statistical Analysis

Prism v8.2 (GraphPad Software, San Diego, CA) statistical analysis software was used to calculate one-way ANOVAs between treatment groups, followed by a Tukey post-hoc test, carried out at 95% significance. Each microtissue was considered independent for all experiments.

3.3 Results

3.3.1 Tissue contraction progresses from the outside edge towards the tissue center

During soft collagen microtissue contraction (0.54 kPa), tissue appears to densify along the peripheral edge first and as contraction continues, the periphery appears to remain the most heavily contracted location (Figure 3.1A). This effect becomes more dramatic when tissue is stiffened with alginate (Figure 3.1A). This may be due to tissue stiffening minimizing the highly heterogenous folding and straining that occurs in soft, malleable tissue. For example, local forces that are likely highly heterogeneous, would arise as sporadic tissue collapse more dramatically in soft tissue. Stiffened tissue on the other hand, requires more stable and persistent force for local collapse, and would therefore be less susceptible to collapse under random force perturbations. This would therefore emphasize stable, global contractile patterns over local, sporadic patterns.

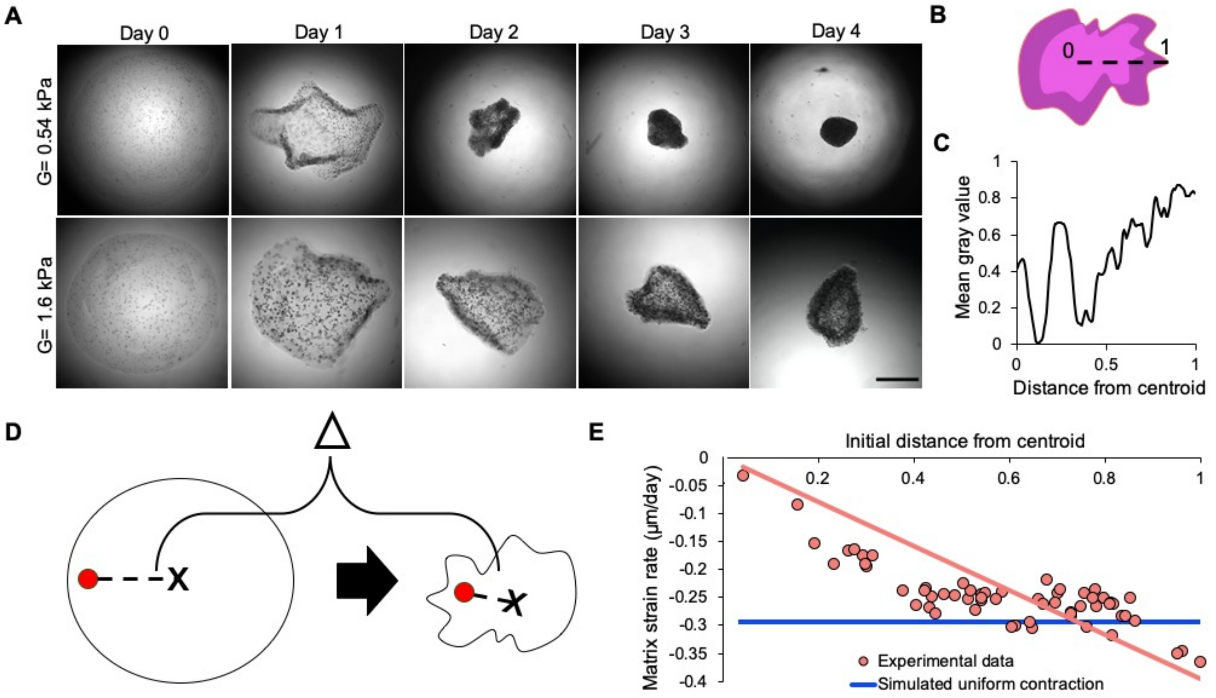

Figure 3.1 Spatial microtissue densification and strain during contraction. A) Brightfield images of soft collagen-1 (0.54 kPa) and stiff collagen-1/alginate IPN (1.6 kPa) matrices during matrix contraction by HS-5 fibroblasts. B) Schematic depicting mean gray value line plots through microtissue from centroid to perimeter. C) Representative mean gray value line plot of a 1.6 kPa microtissue on day 3 of contraction. D) Schematic depicting local strain measurements by measuring embedded fluorescent sphere displacements towards tissue centroid. E) Local strain as a function of day 0 spatial location within the microtissue. Both experimental data and simulated data, that represents even contraction irrespective of spatial location, are shown. Displacements are shown from day 0 to day 2 of contraction. Fit of experimental data is linear. R^2= 0.0101 and y= -0.3945x; Scale: 500 μm.

To quantify global patterns of densification, mean gray values along a line from tissue center to tissue edge were analyzed on day 3 of contraction (Figure 3.1B). In stiffened microtissues of 1.6 kPa, mean gray values increase from the central regions of the tissue to the outer edge (Figure 3.1C) (Figure 3.2). This therefore suggests that locations closer to the tissue edge are undergoing more dramatic densification than central regions.

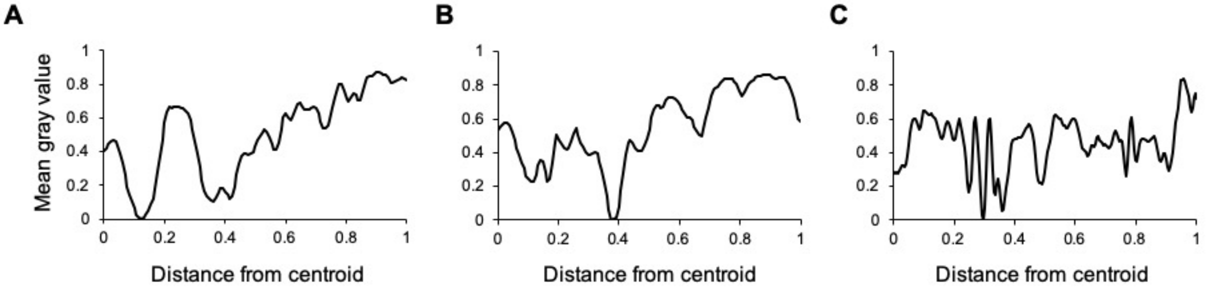

Figure 3.2 Tissue darkness as a function of spatial location within contracting microtissues. A-C) Line plots showing mean gray value from tissue center to tissue edge of 3 different 1.6 kPa microgels on day 3 of contraction.

If tissue is densifying predominantly near the edge, we reasoned that tissue strains were higher in this region. To view global tissue strain patterns, fluorescent spheres ~50 μm in diameter were seeded into microtissues at a low density, giving rise to 1-3 spheres per tissue. This low density allows easy tracking of individual beads over the large and irregular strains seen. Location of the sphere in relation to the global tissue was analyzed across 2 days of contraction, and sphere displacement from day 0 to day 2 was calculated (Figure 3.1D). Experimentally measured displacements in soft collagen tissue of 0.54 kPa demonstrate that locations closer to the edge of the tissue displace farther than locations closer to the center from day 0 to day 2 (Figure 3.1E) confirming that tissue strains are highest near the periphery and decrease towards the center. This pattern is also seen when considering strains from day 0 to day1 and day 1 to day 2 (Figure 3.3).

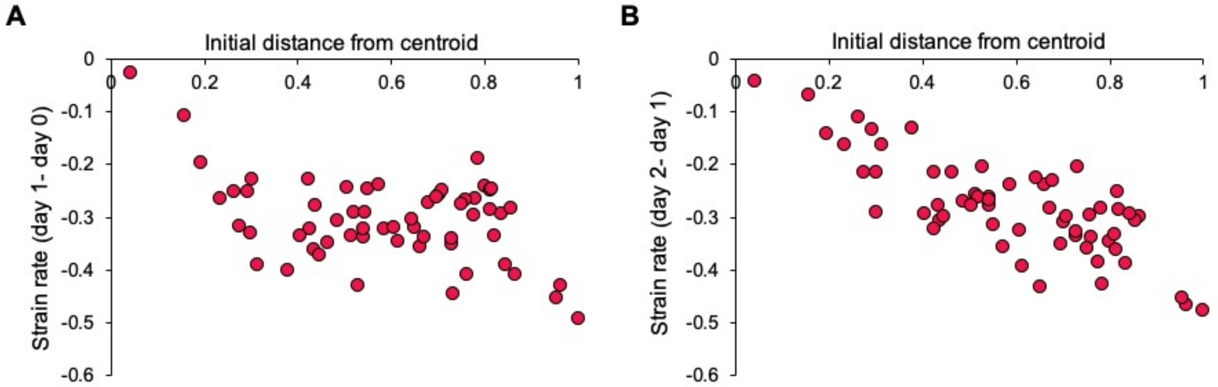

Figure 3.3 Local strain rates as a function of spatial location within the microgel. A) Strains seen from day 0 to day1. B) Strains seen from day 1 to day 2.

To verify that these patterns are distinct from a uniformly contracting gel, when uniform contraction was simulated, where tissue closer to the edge displaces an equal distance inwards as tissue closer to the center, all locations have an identical strain rate, with the exception of the very center, which does not strain (Figure 3.1E).

3.3.2 Microtissue free boundary area can be tuned by changing tissue stiffness together with bioprinting temperature

Since edge effects are playing a dominant role in tissue contraction, tissue free boundary area likely influences contraction. To test this, a technique was developed to tune microtissue free boundary area, while maintaining a consistent volume. Decreasing gelation speed was thought to allow IPN pre-gel more time to spread along the well bottom, thereby flattening the tissue. Since collagen-1 is a thermally gelling material, gelation speed can be controlled by exposing the liquid pre-gel to different temperatures. Therefore, to achieve microgel droplets with high free boundary area, collagen pre-gel was printed into well plates containing chilled PEG, maintained at 4 °C during bioprinting (Figure 3.4A,B). In contrast, printing into room temperature PEG produced lower free boundary area droplets (Figure 3.4 A,B), likely because the liquid began gelling as it contacted the PEG, attenuating spreading at the bottom of the well. This technique produces more dramatic differences in free boundary area when gels are cell-free (Figure 3.4C) than when gels are seeded with cells (Figure 3.4D). This is likely because cells pull the surrounding matrix with them as they sink under gravity, flattening a previously dome-shaped gel. Due to this phenomenon, soft 0.54 kPa microgels no longer showed statistical differences in free boundary area between warm and cold prints when seeded with cells (Figure 3.4D). To compensate for this, pre-gel viscosity was increased by adding alginate, and free boundary areas between warm and cold prints were again different (Figure 3.4D).

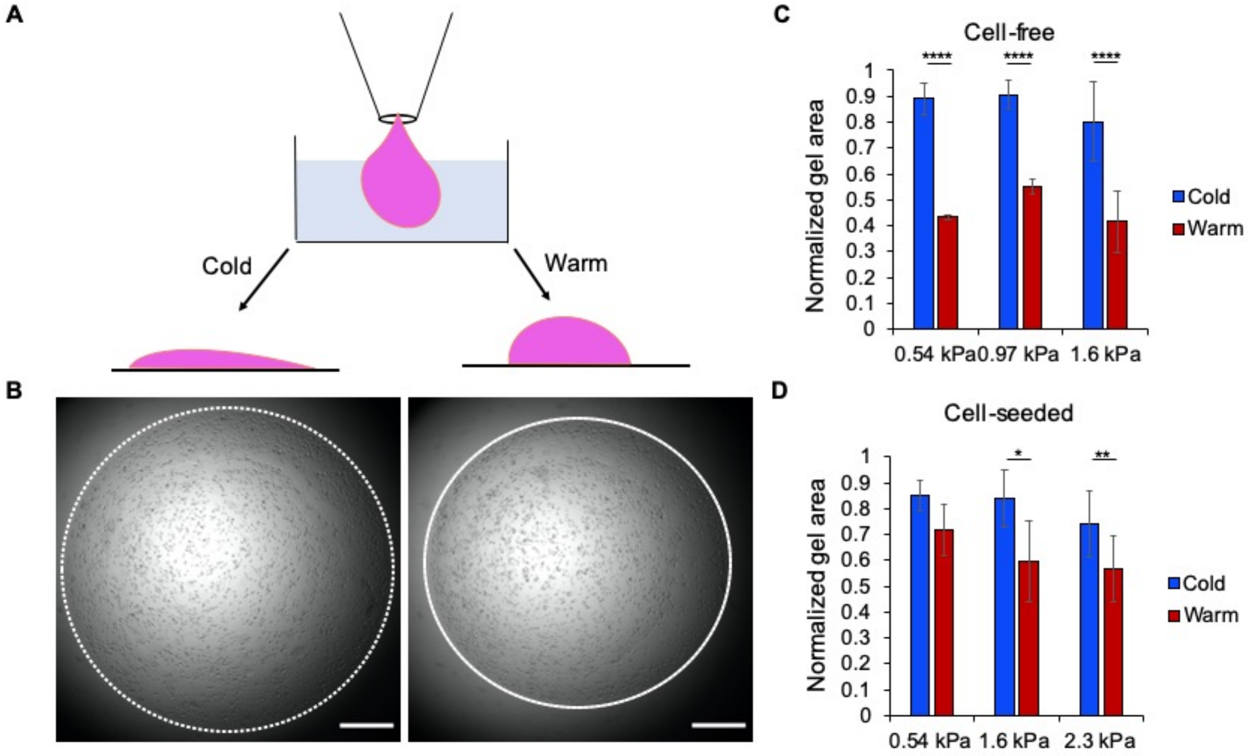

Figure 3.4 A thermal-based technique for free boundary area control. A) Schematic depicting technique to tune microgel free boundary area during microgel bioprinting. B) Representative brightfield images of 2.3 kPa microgels on day 0 following printing into cold (left) or warm (right) PEG. White dashed line outlines microgel area. C) Areas of cell-free microgels of various stiffness following warm or cold bioprinting. D) Areas of cell-seeded microgels of various stiffness following warm or cold bioprinting; Scale= 500 µm. Statistical analysis presented as mean +/- standard deviation; n =6-11; *$p<0.05$, **$p<0.01$, ****$p<0.0001$, by one-way ANOVA with Tukey post-hoc analysis.

3.3.3 High microtissue free boundary area drives faster global contraction

After tuning microgel free boundary area, edge effects on tissue contraction were investigated by following contraction over 6 days. In soft 0.54 kPa gels that showed no statistical difference in free boundary area between warm and cold prints, global tissue strain was highly similar between the two prints, with the only statistical difference occurring on day 2 (Figure 3.5A,C). In stiffened 2.3 kPa gels, where cold prints had significantly higher free boundary area than warm prints, high free boundary area prints showed much larger global strain on every day of contraction past day 1 (Figure 3.5B,C). The rate of microtissue area decrease is also faster with high rather than low free boundary area bioprints (Figure 3.6). Mild differences in free boundary area of ~25%, provide large differences in strain, of ~45% on day 2, demonstrating that edge effects are crucial aspects of tissue contraction.

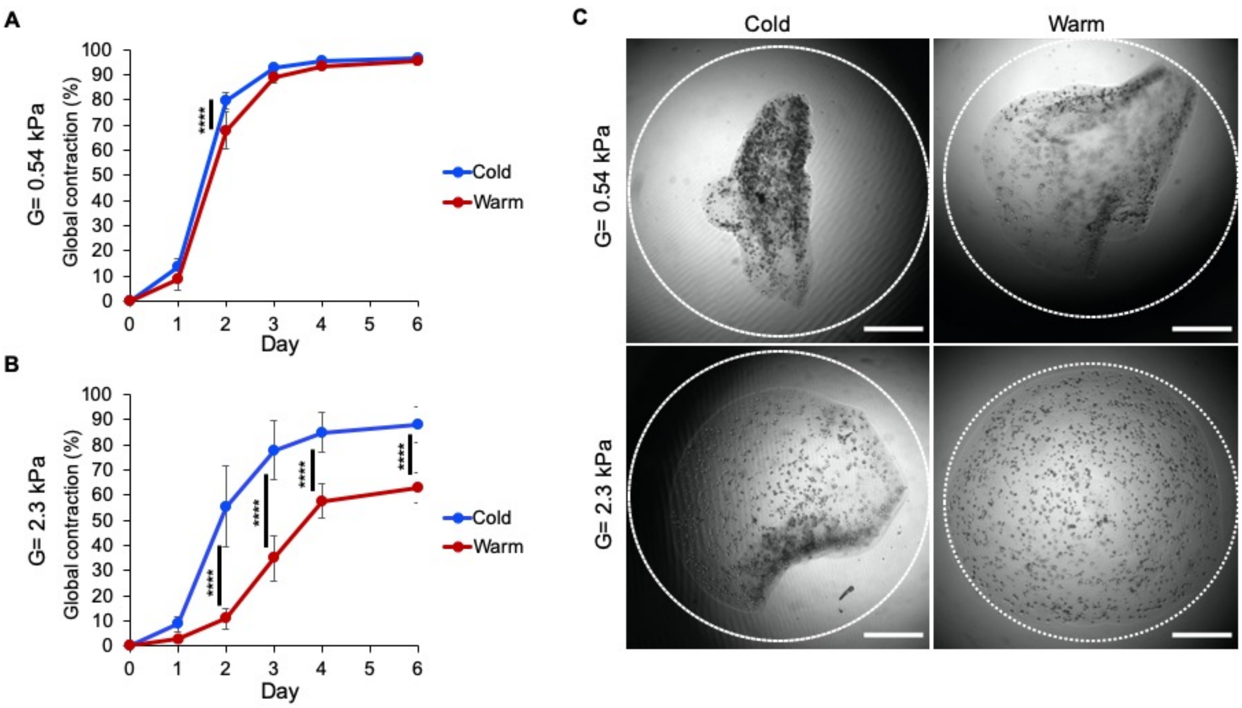

Figure 3.5 Global contraction comparisons between warm and cold microgel bioprints. A) Global contraction of soft (0.54 kPa) microgels when printed into cold or warm PEG. B) Global contraction of stiff (2.3 kPa) microgels when printed into cold or warm PEG. C) Representative brightfield images of 0.54 kPa and 2.3 kPa microgels on day 2 of contraction when printed into cold or warm PEG. White dashed line represents microgel at day 0; Scale= 500 µm. Statistical analysis presented as mean +/- standard deviation; n =9-11; ****p<0.0001, by one-way ANOVA with Tukey post-hoc analysis.

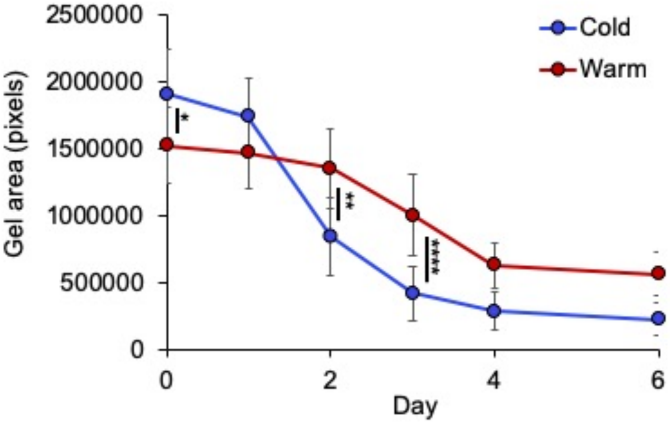

Figure 3.6 Contraction rates arising from cold versus warm bioprints. Graph displays areas of 2.3 kPa microgels by day when printed into cold or warm PEG. Statistical analysis presented as mean +/- standard deviation; n =9-11; *p<0.05, **p<0.01, ****p<0.0001, by one-way ANOVA with Tukey post-hoc analysis.

3.3.4 Cells organize to form global contractile structures along the tissue edge

Since small changes in tissue free boundary area had large impacts on tissue contraction, we reasoned that cells at the tissue edge were behaving differently than cells within the more central regions. F-actin is a cellular structure heavily implicated in contraction, and when tissues were stained for this contractile machinery, it was found that cells organize circumferentially around the gel perimeter, forming a thin, continuous sheet of F-actin (Figure 3.7). Cells immediately inside the perimeter did not organize themselves in this co-ordinated fashion, but rather showed random orientation and spread larger in all directions (Figure 3.7). This was true for both soft and stiffened microgels, although since spread area is limited in stiffened matrices [249] [233] some organized F-actin peripheries showed broken connections rather than one completely connected F-actin superstructure, as in soft tissues (Figure 3.7C).

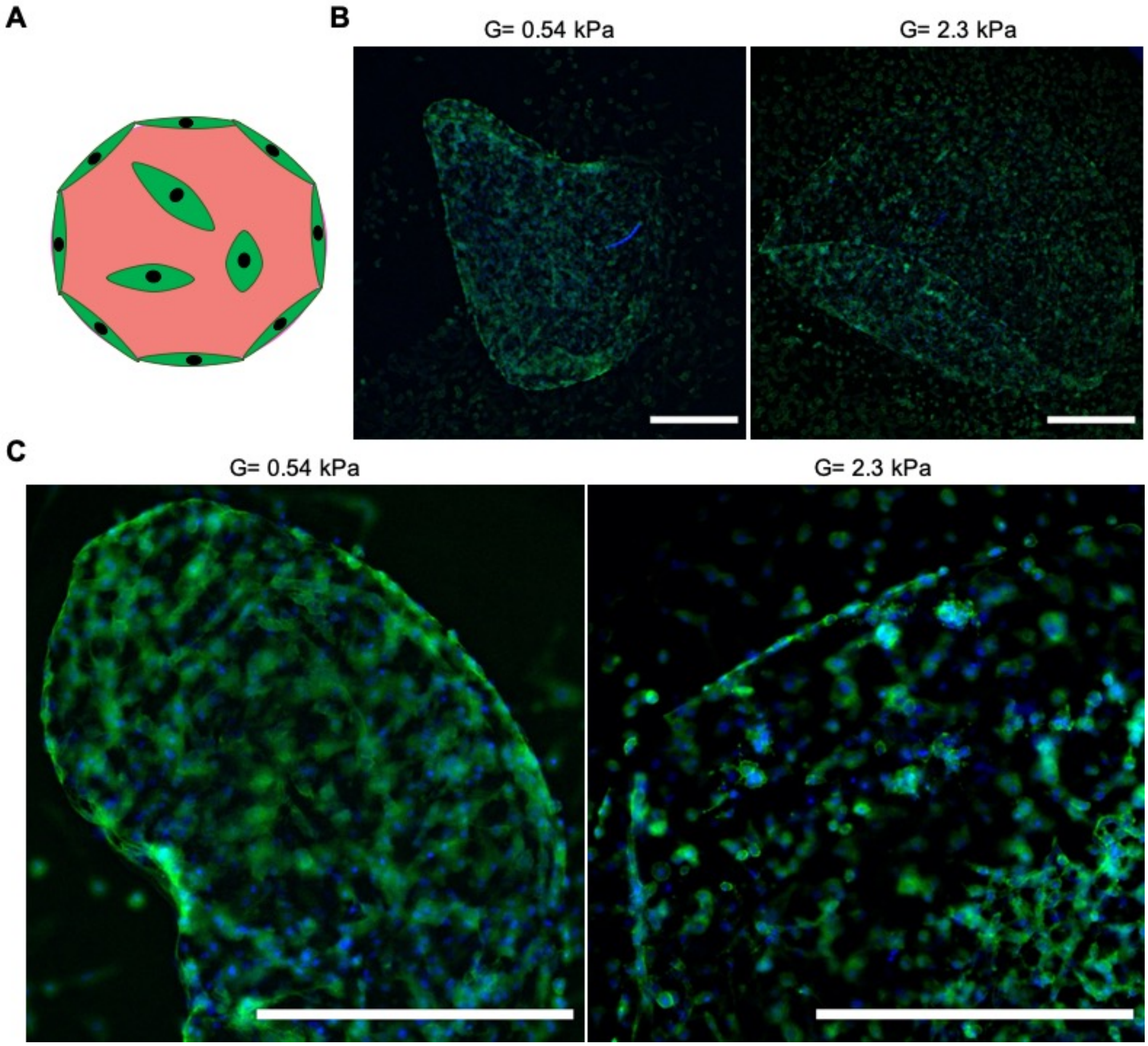

Figure 3.7 Fibroblast F-actin organization within soft and stiffened microtissues. A) Schematic illustrating cell morphology and orientation within microtissues. B) F-actin (green) and nuclear (blue) fluorescent staining within soft (left) and stiff (right) microtissues. C) Enlarged examples of F-actin (green) and nuclear (blue) fluorescent staining within soft (left) and stiff (right) microtissues; Scale= 500 μm.

3.4 Discussion

This microtissue contraction platform allowed visualization of an outside-in contraction phenotype, where the tissue edge appears to show the dominant contractile activity. This has been supported by others who show enhanced tissue densification along tissue edges [250] and preferentially activated fibroblasts along a tissue edge, with higher YAP nuclear localization and α-smooth muscle actin [248]. Moreover, wound closure is primarily mediated by fibroblast contraction [247], and fibroblasts immediate to a wound edge are necessary for wound closure, as selective death of these cells eliminates closure [4].

Using temperature and stiffness together to control microtissue free boundary area was a simple technique for shape control of collagen-based 3D tissues than can be accomplished using standard laboratory equipment. Overall tissue shape can provide distinct local microenvironments that influence cell shape and tissue curvature, which both drive important cell fates and functions such as survival, differentiation, invasive potential and branching morphogenesis [67 72 8 73 35]. This technique may hence prove useful for alternative tissue engineering applications in development and disease.

By tuning tissue free boundary area, distinct contractile phenotypes were seen, uncovering a new biological phenomenon that controls tissue contraction. Global tissue strains were significantly higher within high free boundary area tissues (Figure 3.5, 3.6), providing a need to control for this previously overlooked variable within a commonly used assay.

No strain differences were seen on most days within soft microtissues, as there was no statistical difference in free boundary area between warm and cold prints. Even without statistical differences, cold prints still showed higher strain on day 2 (Figure 3.5A). While this could be due to the very minimal, yet reproducible free boundary area differences seen, another explanation is the likely difference in pore structure between warm and cold prints. Changing the temperature during collagen gelation can change the highly local fibrous pore structure of the matrix. Lower printing temperatures may therefore give rise to more bundled fibers with larger pore sizes [48]. These bundled structures cause increased contractility of breast cancer cells [51]. Larger pore sizes may therefore be contributing to the increased contractility seen on day 2. However, since all other days displayed the same strains, overall contraction rates are therefore minimally impacted and highly contractile fibroblasts may be relatively insensitive to pore size. This is supported by other work demonstrating that scaffold pore size does not influence contraction by infiltrating fibroblasts following *in vivo* scaffold implantation [251]. Free boundary area therefore remains the dominant driver of strain differences seen here.

The likely mechanism for this phenomenon is that free boundary area determines global proportions of organized and activated cells. A tissue with higher free boundary area, as is the case with alginate-doped, cold printed microtissues, gives rise to a tissue structure with a higher overall proportion of cells located along a tissue periphery. Moreover, organized cell elongation was seen at the tissue periphery (Figure 3.7), thereby giving rise to a higher proportion of organized cells within high free boundary area tissues. It is possible that co-ordinated contraction at the tissue edge due to cell organization is more efficient than unco-ordinated contraction within the center, thereby resulting in higher strains with higher free boundary area. Cell organization was seen in both soft and stiffened microgels (Figure 3.7) demonstrating that limited spreading caused by matrix stiffening [249] does not prevent the ability of cells to sense the tissue edge and spread circumferentially. A continuous monolayer of cells at the tissue edge was still seen in many stiffened matrices because microgels were seeded at a high enough density to allow cell-cell interactions, even with a limited spread area. This therefore validates circumferential cell organization as a possible mechanism for the strain differences seen between high and low free boundary areas in stiffened microtissues.

This circumferential organization at the tissue edge has been seen in other fibroblast-based cultures [247] [248] and during wound closure, this mechanism has been described as “purse string” tissue closure [247]. This organization likely results from contact guidance, as cells at the tissue edge cannot spread into the surrounding media, thus must spread along the matrix boundary.

Higher mechanical activation of fibroblasts also occurs at the tissue edge, with enhanced α-smooth muscle actin and larger matrix strains as a result of cell contractility [248]. This enhanced activation may also be occurring within our platform, giving rise to a higher overall proportion of mechanically activated cells within high free boundary area tissues. Together, this data uncovers the importance of free boundary area within contracting tissues and further supports edge effects as strong drivers of tissue contraction.

A limitation arises with the presented findings. In this work free boundary differences demonstrate global strain differences in stiffened tissue, making conclusions drawn here only possible for stiffened tissue, often associated with diseased phenotypes[90] [88] [252]. It is therefore unknown if free boundary area influences global strain in soft tissues. However, with edge effects causing the seen differences, and soft tissues demonstrating more stable and consistent F-actin superstructure sheets at the periphery than stiffened tissues, it is therefore likely that soft tissue contraction is more affected by free boundary area than stiffened tissues.

3.5 Conclusions

Changing PEG temperature during bioprinting is an effective strategy to tune microgel free boundry area in this ATPS platform. When seeded with cells, this technique becomes less effective for soft collagen gels; however, becomes increasingly effective when microgels are stiffened with alginate. High free boundary area microtissues showed higher strains than low free boundary area tissues demonstrating that surface effects influence tissue contraction, likely due in part to cellular organization around the tissue perimeter. This work hence provides a new technique for 3D tissue shape control, and demonstrates that collagen contraction assays cannot be considered homologous between studies, highlighting a need for careful consideration of free boundary area for reliable comparisons of tissue contraction.

Chapter 4

Local mechanical profiling of collagen microtissue contraction using integrated biomaterial sensors

The following chapter addresses my final thesis objective by exploring how initial tissue stiffness drives local strain, stiffness, and cell-induced forces during fibrous tissue contraction. Here, I provide a final rationale highlighting the novelty of the work, describe the methods involved in strain, stiffness, and stress data collection and analysis, and discuss the important research findings supporting matrix strain as a dominant driver of 3D tissue contraction.

This chapter in particular, was a collaborative effort, and a detailed description of individual contributions can be found in *Contribution of Authors*. Wontae Lee contributed to the critical thinking and discussion of all local force data presented here, and modified versions of Figures 4.1, 4.3, 4.8, and 4.15 have been included in her PhD thesis. Dr. Stephanie Mok analyzed all stiffness measurements presented within. Kimberly Seaman conducted most experiments investigating local stress and analyzed all local stress data. Zizhou Xiang conducted the remaining experiments investigating local stress.

Abstract

Tissue contraction is a critically important process in developmental morphogenesis, tissue homeostasis, wound closure, tumour progression, and fibrotic disease. This biomechanical process is driven by forces generated by cells resident within the fibrous matrix and global matrix contraction would therefore be higher in compliant matrices. However, increased stiffness is also thought to increase cell force generation based largely on experiments on 2D elastic substrates; which suggests a positive feedback loop between force and matrix stiffness. Relatively little is known about this dynamic relationship in a physiologically realistic, remodellable 3D tissue. To gain insight into this process, cellular length-scale hydrogel sensors were used to map both evolving local forces and stiffness within a remodelling collagen microtissue. We find that cells increase their force output over time and do so in a spatially independent, highly heterogeneous manner. Local tissue densification during contraction increases similarly heterogeneously. Moreover, local tissue stiffness does not correlate with global tissue strain, but instead dramatically increases during the first day of contraction and remains constant thereafter as the tissue continues densifying. Increasing the baseline tissue stiffness with an alginate interpenetrating network slows global tissue strain. Local forces are distinctly different between initially soft and initially stiffened tissues throughout much of the contraction process; however, local stiffness does not differ between initially soft and initially stiff tissues at any timepoint. Contrary to results from 2D hydrogel culture models, greater forces occur in softer matrices that have undergone greater matrix strain. This surprising result suggests that stiffness is not the sole driver of local forces. Local forces from both initially soft and initially stiff tissues correlate together closely with local tissue remodelling. This work hence suggests that strain rather than stress could be a unifying process variable for mechanobiological feedback loops, particularly in biologically relevant 3D, remodellable matrices.

4.1 Introduction

Tissue contraction is a highly conserved and fundamentally important cell behaviour that is involved in both physiologic and pathologic processes [1]. Embryonic cells drastically strain and remodel the ECM during developmental morphogenesis [2] and fibroblasts, responsible for stromal maintenance, ensure ECM homeostasis during growth and adulthood as well as stromal recovery following injury, such as myocardial infarction or wound closure [3] [6] [253]. Dysregulated contraction is a standard characteristic of fibrotic disease [5] [3], capable of affecting many organ systems and is a predominant characteristic of diseases such as heart failure and tumour progression [253] [6]. It is therefore crucial to better understand this process so heavily implicated in tissue development and disease.

During tissue contraction, cells exert forces onto their surroundings. These forces can strongly influence neighbouring cell behaviour directly through externally applied matrix strain. Matrix strain is a known driver of many fundamental and disease related cell behaviours such as proliferation, smooth muscle actin expression, ECM synthesis, and TGF-β secretion [185] [184] [254] [255]. Matrix strain is especially relevant during tissue contraction, where cell-induced forces and corresponding matrix strains are high. Moreover, as tissue contracts, collagen becomes denser and stiffer [256]. High stiffness drives cellular contraction [9] [257] [258] and contractile related phenotypes such as cell spread on 2D hydrogels [236] [259] [53], which has been thought to further drive force generation in a positive feedback loop; however, contractile related phenotypes such as cell spreading and smooth muscle actin expression are decreased with high stiffness in fibrous matrices [131] [260] [107]. How matrix stiffness influences local force generation, matrix strain, and downstream local stiffness changes is largely unknown.

Contraction mechanics has predominantly been studied on 2D, elastic substrates that maintain stress under applied strain [9] [258]; however, human tissues contain a fibrous extracellular matrix (ECM) that molds and reorganizes under cellular traction forces. To address this, one study examined single-cell fibroblast contractile forces on top of collagen gels [261], while others have looked at 3D tissue contraction between solid pillars [262] [263] [192]. Boundary stiffness influences over bulk force generation has also been explored by suspending fibroblast seeded collagen between flexible, magnetic PDMS posts, and post stiffness was tuned by applying a magnetic field, thereby limiting post flexibility [257]. Each of these innovative works demonstrates that fibroblasts increase their bulk contraction over time, and pull harder against stiffened, elastic substrates, but how ECM stiffness influences local mechanics within a remodellable tissue has remained unstudied, and it is these local mechanics that drive cellular phenotypes.

Here, we capture cell-induced forces, stiffness and strains within contracting microtissues at the highly local scale of the cell, uncovering the mechanical information that resident cells receive. It is these local mechanics that then drive cellular phenotypes. Local forces and local stiffness were each captured with two unique, cell-sized, spherical force and stiffness sensors respectively, embedded within collagen-1 and fibroblast containing tissues. These separate sensors capable of measuring distinct mechanical environments were nested within fibroblast-containing microtissues. Microtissues of 2 μL that could be bioprinted into wells using automated liquid handling [249] allowed increased throughput of tissue production and therefore substantially higher numbers of mechanical measurements: an important consideration for complete tissue sampling when measurements are highly local. Finally, baseline tissue stiffness was capable of tuning by interpenetrating collagen-1 with alginate [249]. Collagen concentration was held constant and initial stiffness was tuned by changing alginate concentration and subsequently saturating alginate crosslinking sites with Ca^{2+}.

This platform therefore allows cell-scale force and stiffness profiling within live and dynamic tissue contraction. Here, spatiotemporal force patterns helped characterize tissue contraction and the impact of actively contracting cells to tissue stiffness was illustrated. By changing baseline tissue stiffness, the dependence of local forces, local stiffness, and local strain on this typically strong driver of tissue phenotypes could be seen in a remodellable 3D setting.

4.2 Materials and Methods

4.2.1 Materials

Unless otherwise stated, all cell culture materials and supplies were purchased from Fisher Scientific (Ottawa, ON) and Life Technologies (Carlsbad, CA, USA), and chemicals from Sigma Aldrich (Oakville, ON).

4.2.2 Cell culture

HS-5 human fibroblast cell line (ATCC) was cultured in DMEM supplemented with 10% fetal bovine serum (FBS) and 1% antibiotics-antimycotics, and maintained at 37 °C, 5% CO_2. Cells were routinely passaged using 0.25% trypsin-EDTA for seeding experiments or re-plating.

4.2.3 Microgel printing and contraction

Microgels were printed following established protocols [249]. Briefly, a dextran (500kDa; dextran.ca) and collagen-1 (2 mg/ mL final concentration) pre-gel solution containing either 0, 0.8 or 1.6 mg/ mL of sodium alginate was dispensed into a polyethylene glycol (PEG)-rich suspension to maintain phase separation and allow microtissue gelation with a liquid-liquid interface. A PIPETMAX® (Gilson) automated liquid handling system was loaded with reagents and programmed to dispense the PEG-rich phase and dextran-rich droplets into ultra-low attachment 96 well plates. Tissue droplets were bioprinted at 2 µL volumes. Plates were then removed from the PIPETMAX® and gels were incubated at 37 °C for 45 minutes. Calcium chloride was added to all cultures for 5 minutes, at an ~1000x molar excess (0.1 wt%) for alginate crosslinking to saturate crosslinking sites. Samples were either aspirated by hand or serially diluted to replace the PEG media with supplemented media, and cultured at 37 °C, 5% CO_2 during experiments. For all contraction experiments, HS-5 cells were seeded into tissues at a density of 1000 cells/ µL. Gels were then incubated with FBS supplemented media at 37 °C, 5% CO2. Microgels were allowed to contract for 2-10 days depending on the experiment. Global contraction was represented by quantifying microgel area percent change from day 0. It was analyzed using the freehand selection tool in ImageJ software, tracing the outside of the tissue, and collecting the area from the measurements tab under “Analyze”.

4.2.4 Microspherical stress gauge (MSG) fabrication and analysis

MSGs were fabricated following established protocols [198]. Briefly, 60 Pa polyacrylamide hydrogel microsphere sensors were formed by polymerizing polyacrylamide using a phase separation emulsion technique. A premixed solution of 3.0 wt% acrylamide, 0.06 wt% bisacrylamide (Bio-Rad Laboratories), 10% w/v fluorescein-o-methacrylate in DMSO (0.1% final concentration), and 0.15% v/v tetramethlylethylenedianine (TMED) was prepared, followed by addition of a 1% w/v ammonium persulfate (APS) solution in PBS to catalyze the polymerization. This mixture was then immediately added to a kerosene and 6% w/v surfactant solution (Polyglycerol polyrincinoleate; PGPR 4150; Palsgaard) and vortexed to produce polymerized microsphere sensors. Sensors were washed multiple times, first with fresh kerosene and then with PBS. Sensors were allowed to swell to equilibrium overnight at 4 °C in PBS and were then functionalized via UV-activated Sulfo-SANPAH (GBiosciences) with a 0.05 mg/mL solution of collagen I (3mg/mL).

To measure local forces within microtissues, MSGs were added at a final concentration of 1 bead/ µL of tissue, providing 1-3 beads per tissue on average. Brightfield images of contracting microgels were taken every 24 hours, along with matched fluorescent images of the MSGs. Cultures were then placed back into 37 °C, 5% CO_2 conditions for continued contraction. MSG analysis was conducted following established protocols [198]. Briefly, the circumference of the sensor was traced using ImageJ software and analysis of the major and minor axis length was determined using the bounding rectangle tool within "Analyze". Length change from day 0 was used to computationally determine stresses. Each MSG was traced 3 times, providing average axis lengths, with standard deviation used as the error. Force locations within the tissue were measured in relation to their distance from tissue centroid, found by tracing the circumference of the tissue and using ImageJ software to calculate the centroid. Distances were internally normalized to the diameter of each specific microtissue.

4.2.5 Microscale temperature-actuated mechanosensor (µTAM) fabrication and analysis

µTAMs were fabricated following established protocols [144]. Briefly, microspherical sensors were formed by polymerizing PNiPAAM with bisacrylamide crosslinker. During polymerization, the mixture was immediately vortexed while within a kerosene bath. µTAMs were then washed, centrifuged down, supernatant removed and, sensors resuspended several times, first with fresh kerosene to remove surfactant traces and then with PBS. µTAMs were allowed to swell to equilibrium overnight at 4 °C in PBS and sensors were then functionalized with a 0.05 mg/mL solution of collagen I (3mg/mL). µTAM recipe used was 3% NiPAAM/ 0.2% bisacrylamide giving an expanded sensor stiffness of 450 Pa.

To measure local stiffness, µTAMs were added at a final concentration of 2 beads /µL providing 2-5 beads per tissue on average. Brightfield images of contracting microgels were taken every 24 hours, along with fluorescent images of the sensors. Two sets of fluorescent images were taken, the first images were taken in a thermally controlled chamber, maintaining the cultures at 37°C. Cultures were then placed on ice for 4 minutes to allow a culture temperature drop to 24°C. Cultures were then left at room temperature for 30 minutes to allow µTAMs time to swell. Fluorescent images were then retaken of expanded sensors. Sensors were calibrated by embedding them within polyacrylamide of known stiffness (150, 400, 4250, 9200, 19500, 245000, and 271000 Pa) and calculating their expansion following the temperature change. A free-swell in PBS was also completed to view maximal expansion with a surrounding stiffness of 0 Pa. New cultures were used for each timepoint to ensure repetitive temperature transitions did not influence tissue contraction.

Stiffness sensor analysis described elsewhere [144]. Briefly, for sensors with defined borders, the image was auto-thresholded and the "Analyze particles" tool was used to collect Feret's diameter using ImageJ software. Sensors that did not provide reliable thresholding due to undefined borders were instead traced by hand using the oval tool, and Feret's diameter was again collected. Occasionally, sensor measurements were tested using both of the mentioned methods to ensure measurement consistency. Due to anisotropic compressional forces surrounding sensors, some sensors were not perfectly spherical. To compensate for this, sensor areas were used while assuming a spherical area and radius was calculated. This was done for both small and expanded sensor sizes. The change in radius was input into a previously developed computational model to calculate surrounding stiffness.

4.2.6 Tissue densification analysis

Microtissues were printed with a final concentration 0.5% (v/v) inert fluorescent particles (3.42 µm, 1% w/v stock concentration; Nile-red labelled; Spherotech) and both brightfield images, as well as multiple fluorescent images through the z plane of the tissue were captured of contracting microgels every 24 hours.

All fluorescent intensity data was taken from maximum projection Z projects of complete stacks through contracting tissues. Fluorescent intensity line plots were produced using the line tool in Image J software and drawing a line from the tissue centroid to the tissue edge. Mean grey value along the line was then analyzed. Fluorescent bead density was correlated to brightfield mean gray value by using the oval tool in Image J to draw 40 x 40 μm circles in 5 different locations of each contracted tissue and analyze the mean grey value of the micro-locations in the brightfield and corresponding fluorescent locations. Both brightfield and fluorescent values were normalized to the largest value across all days. Brightfield mean gray value is low when darker and high when lighter, while fluorescent mean gray value is the opposite, therefore all brightfield values were inverted by applying the mathematical formula of (value-1)* -1, to provide a high mean gray value being equivalent to a dark location.

4.2.7 Image acquisition

Fluorescent, brightfield, and phase-contrast images were collected on an Olympus microscope (IX73, using Metamorph software).

4.2.8 Statistical Analysis

Prism v8.2 (GraphPad Software, San Diego, CA) statistical analysis software was used to calculate one-way ANOVAs between treatment groups, for all data. Each MSG or μTAM was considered independent for stress and stiffness data respectively. Each local fluorescent intensity pixel was considered independent for local densification comparisons. A Kruskal-Wallis post-hoc test, carried out at 95% significance was implemented for all stiffness data, as stiffness data did not follow a normal distribution. A Tukey post-hoc test, carried out at 95% significance was implemented for all other data.

4.3 Results

4.3.1 Local forces increase heterogeneously and throughout the tissue during contraction

To measure local forces within live contracting tissues, force sensing beads termed microspherical stress gauges (MSGs) were dispersed into pre-polymerized collagen and fibroblast containing gels (Figure 4.1A) and microtissue droplets were bioprinted into well plates following a previously developed protocol [249]. MSGs are composed of polyacrylamide: an elastic material that deforms linearly with applied stress [198]. Sensor deformation then reliably illustrates force arising at that local position within the tissue. Local, cell-generated forces arising from cell contraction are therefore calculated (Figure 4.1B) [198].

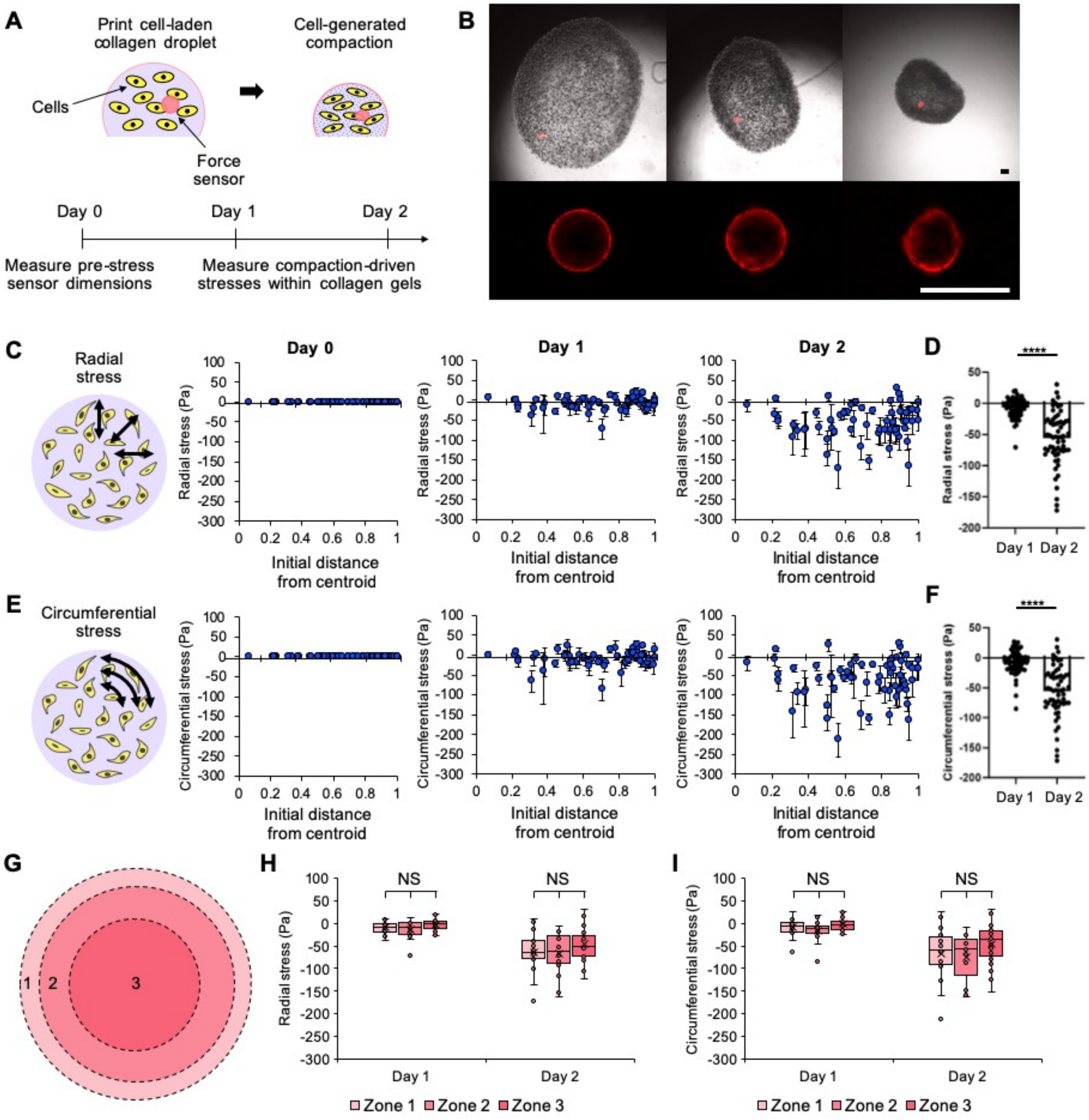

Figure 4.1 MSG force sensors show spatiotemporal local forces within contracting collagen microdroplets. A) Schematic of the contraction experiment involving MSGs within collagen-1 and fibroblast tissues. B) Brightfield and RFP overlaid (top) and RFP only (bottom) images depicting global tissue contraction and force sensor deformation respectively. C) Radial stresses arising in tissues by day, along with their location within the tissue . D) Comparison of radial stresses between days 1 and 2 of contraction. E) Circumferential stresses arising in tissues by day, along with their location within the tissue . F) Comparison of circumferential stresses between days 1 and 2 of contraction. G) Schematic depicting methods of splitting tissues into zones of equal area to compare forces within spatial tissue

zones. H) Comparison of forces within tissue zones; Scale: 100 µm. Statistical analysis presented as mean +/- standard deviation; (D,F,H,I): n = 21 microtissues, 60 measurements; ****$p<0.0001$, by one-way ANOVA with Tukey post-hoc analysis.

Both radial and circumferential orientations of force can be read by the sensors (Figure 4.1C,E), providing directional information on local tissue compression or tension. Positive forces correspond to tensional forces as a result of sensor stretching, while negative forces correspond to compressional forces as the sensor axis shrinks. Forces were plotted against their location within the contracting microtissue, providing spatial information on the local forces. Since tissues contract irregularly, but force sensor location within the overall tissue remains stable, forces were plotted against the initial location within the tissue on day 0 (Figure 4.1C,E) in order to more clearly follow individual forces with time. Local forces within contracting microtissues were measured across 2 days.

Forces within tissues were largely compressional, with only a few small tensional forces (Figure 4.1C,E). This is expected as the tissue globally contracts over 90% of its area [249]. Both radial and circumferential compressional forces increased from day 1-2 (Figure 4.1D,F) and did so in a highly heterogeneous manner, ranging from less than 10 Pa to over 200 Pa by day 2 (Figure 4.1C,E). Forces increased randomly throughout the tissue, with higher forces arising in inconsistent locations (Figure 4.1C,E) and when tissues were split into zones of equal area (Figure 4.1G) forces within each zone did not differ from each other (Figure 4.1H) suggesting that local contractile magnitudes are independent of spatial positioning. Forces followed a similar spatial organization when plotted against their current or instantaneous distance from the centroid, with more condensed forces on day 2 (Figure 4.2).

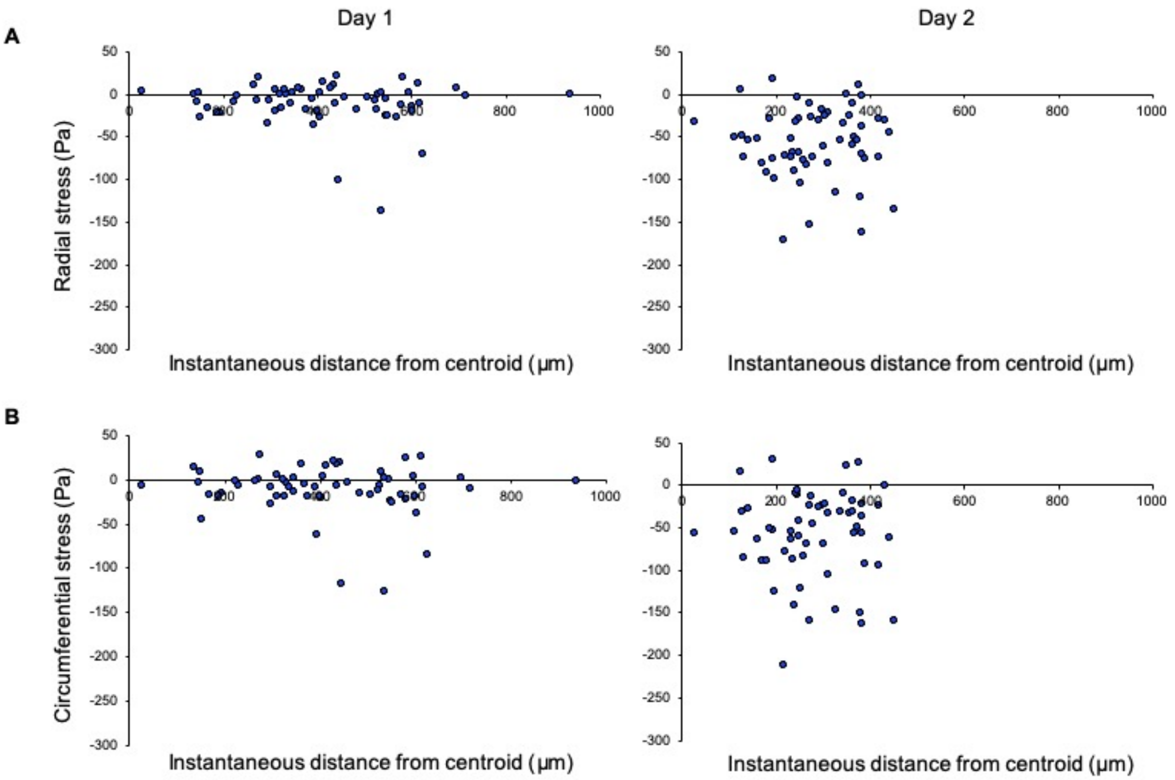

Figure 4.2 MSG force sensors show local forces as a function of current distance from tissue centroid. Both A) radial and B) circumferential stresses are shown across 2 days of contraction.

4.3.2 Local tissue densification increases heterogeneously and correlates with local forces

Since forces increase over time throughout the tissue, a local cellular cue may be responsible for driving this increase. Strain is a known driver of fibroblast smooth muscle actin expression [184], and the matrix is locally straining as it contracts. To visualize the local gathering, and therefore straining of tissue, inert fluorescent particles were seeded at a high density into microtissues. On day 0, particles are spaced relatively farther apart throughout the tissue thereby fluorescently appearing dimmer. As the tissue strains the particles densify and fluorescent intensity increases, showing global tissue densification (Figure 4.3A,D). At the local level, tissue densification is highly heterogeneous (Figure 4.3C,D) and fluorescent analysis (Figure 4.3C) is capable of visualizing this local heterogeneity more effectively than the matched brightfield images (Figure 4.3B). When quantifying the fluorescent intensity from microtissue centroid to a microtissue edge, heterogeneity of tissue densification becomes clear (Figure 4.3C,D). Fluorescence on day 0 begins relatively homogenous from microtissue centre to edge; however, once the tissue begins contracting fluorescent intensity becomes highly heterogenous, and remains so even as a fully contracted dense tissue ball (Figure 4.3D) seen only as homogenously black via brightfield imaging (Figure 4.3A).

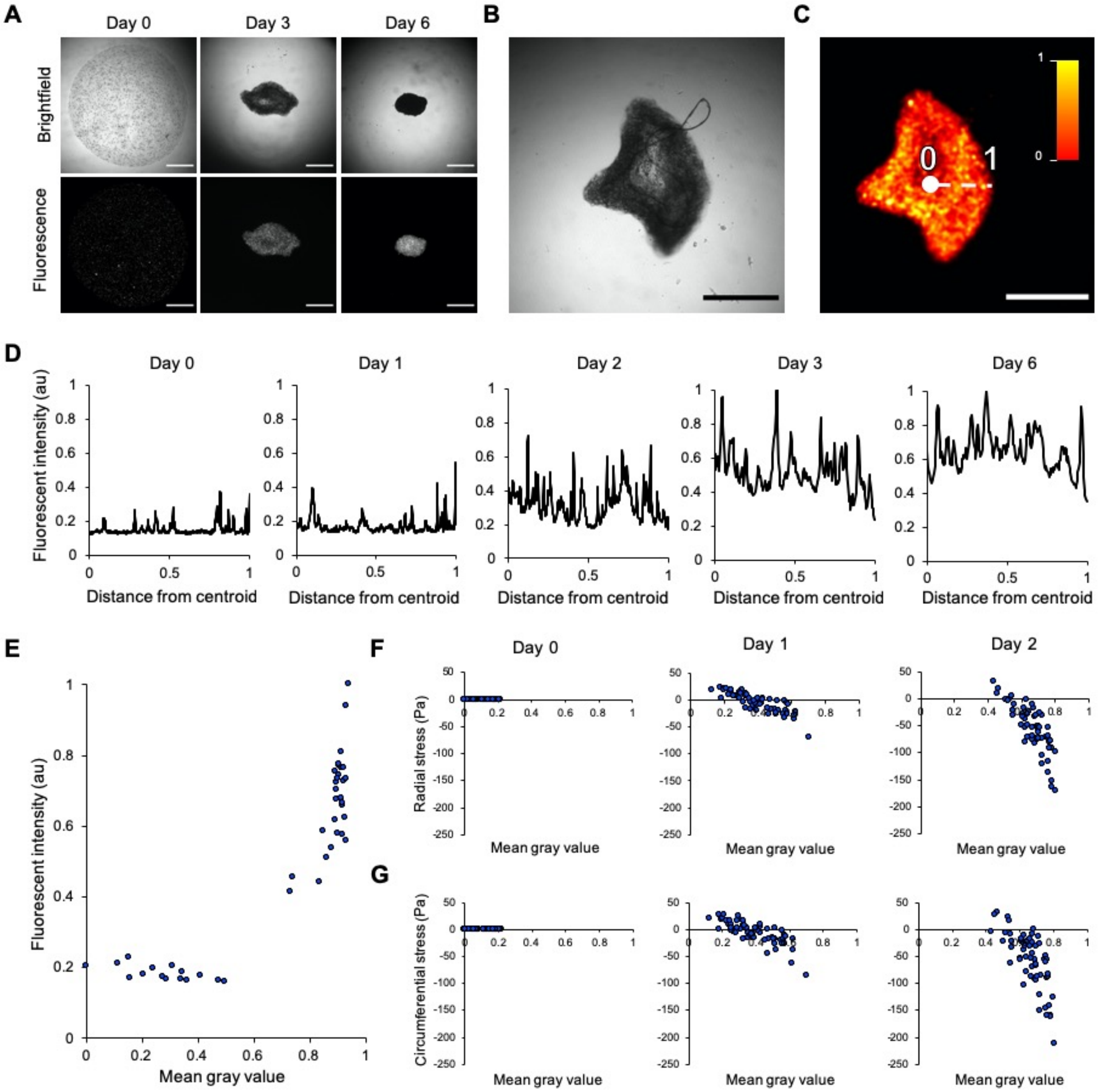

Figure 4.3 Correlation of local tissue densification with local forces during collagen microdroplet contraction. A) Brightfield (top) and corresponding fluorescent (bottom) images of inert fluorescent particle containing microtissues during contraction. B) Brightfield and corresponding C) fluorescent intensity heat map of a tissue on day 3 of contraction; scales: 500 µm. D) Representative line plots of local fluorescent intensity from tissue centroid to tissue edge, followed across multiple days of contraction. E) Plot of fluorescent intensity against matched brightfield intensity of local 40 x 40 µm circles sampled across 5 different locations within 3 different tissues on each of day 0, 3, and 6. F) Radial

and G) circumferential stresses plotted against the local mean gray values taken at the location of the force measurement; Scale: 500 µm.

As microtissues strain, local areas sporadically darken throughout the entire tissue when captured through brightfield microscopy. This darkening increases throughout the contraction process and was thought to be local tissue densification as a result of cells gathering the available collagen matrix. However, other factors such as cell clustering and proliferation, or new ECM deposition could contribute to the local darkness, so to confirm that tissue strain of existing matrix was occurring at these optically dense locations, local fluorescence was plotted against the matched local brightfield image. Local fluorescence shows a highly non-linear, yet strongly positive correlation with local mean gray value (Figure 4.3E). It was not possible for local force and local fluorescence data to originate from the same contracting tissues, as poor contraction was seen in microtissues containing both MSGs and fluorescent particles. Therefore, local tissue darkness was further confirmed to be tissue densification by additionally correlating local cell density (Figure 4.4) and local collagen-1 staining (Figure 4.5) with local mean gray value. When local mean gray value, used as a surrogate for local tissue densification, is then plotted against local forces, forces increase with radial (Figure 4.3F) and circumferential (Figure 4.3G) compressional forces suggesting that local tissue strain correlates with increased local forces.

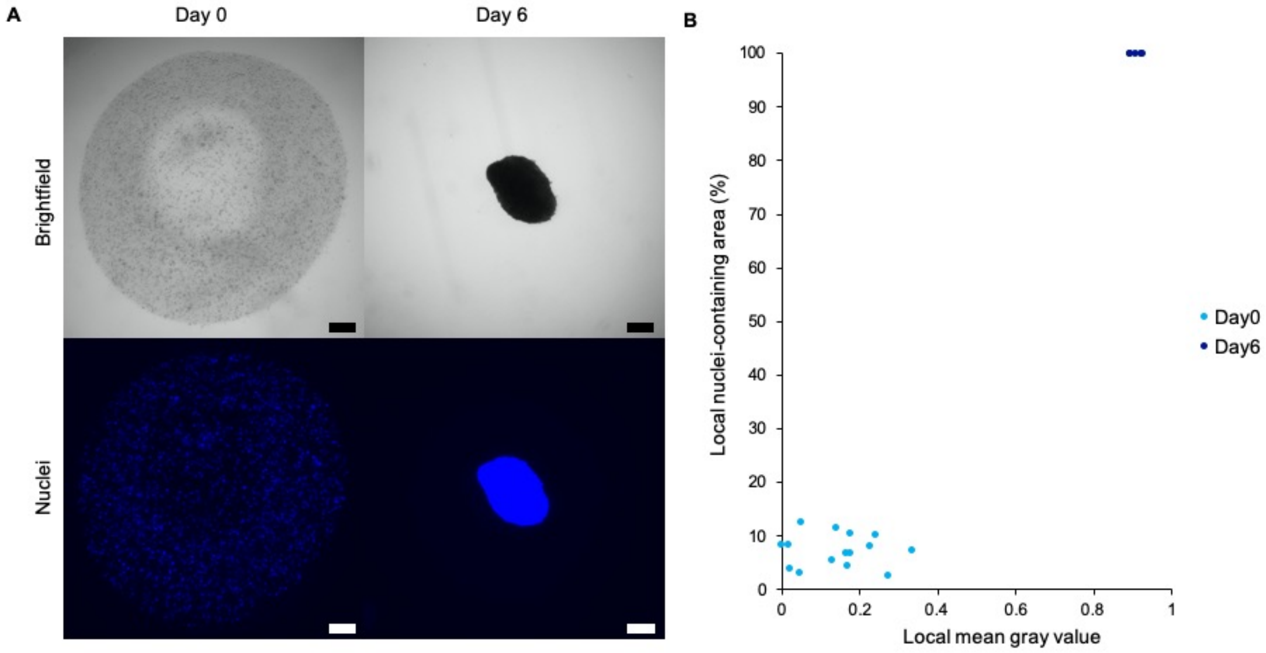

Figure 4.4 The relationship between local mean grey value and cell nucleus density within contracting microtissues. A) Brightfield (top) and matched nuclear staining (bottom) of a representative contracting tissue on days 0 and 6. B) The percentage of a local area containing cell nuclei plotted as a function of tissue darkness in the same local region of the matched brightfield image; n=3 microtissues, 5 local locations per microtissue; Scale: 200 µm.

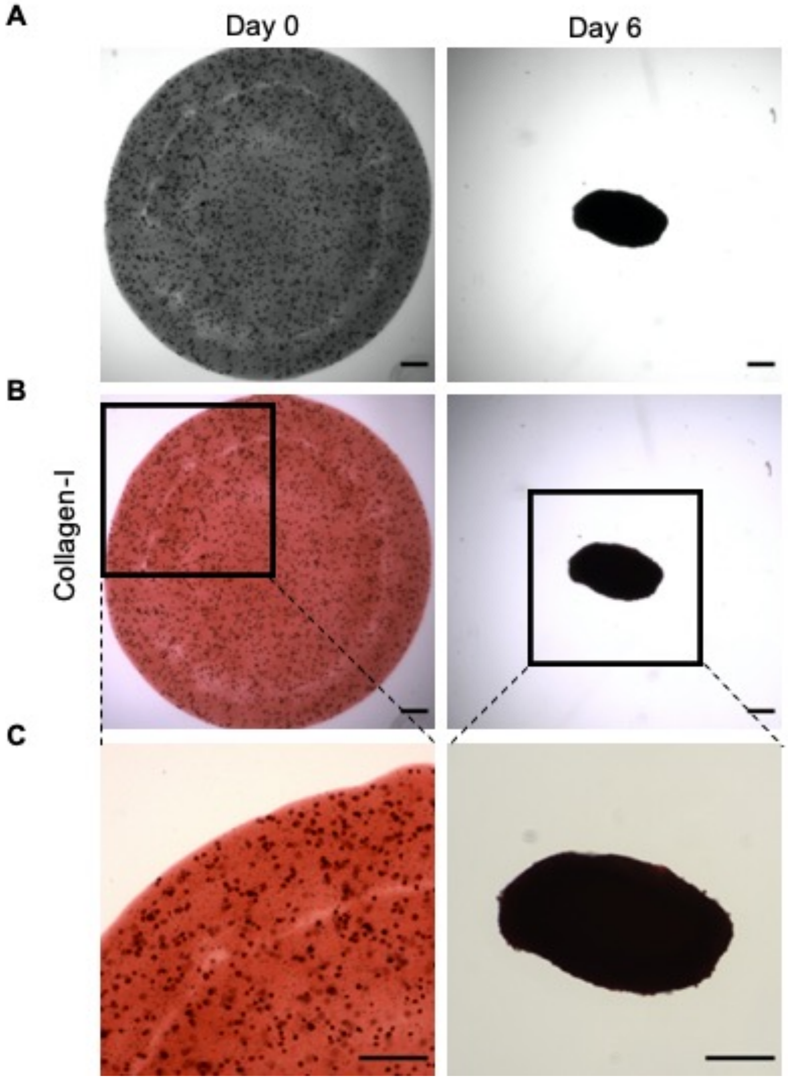

Figure 4.5 The relationship between brightfield tissue darkness and collagen-1 staining intensity within contracting microtissues. Representative A) brightfield and B) matched collagen-1 colour brightfield images on day 0 and 6 of contraction. C) Magnified images of the collagen-1 staining; Scale: 200 µm.

4.3.3 Local stiffness is dominated by cellular activity rather than globally contracted state

High stiffness has been shown to drive contractile forces [9 258 257], and since local tissue density increases during contraction, we reasoned that local stiffness is likely increasing during tissue contraction. Increasing stiffness could be an alternative explanation for the force increases seen. To measure local stiffness, µTAM stiffness sensing beads were dispersed into microtissues and local stiffness was calculated by measuring sensor expansion following a mild temperature drop. Details of sensor development are previously explained [144], but briefly, μTAMs are composed of poly N-Isopropylacrylamide (NiPAAM), a temperature sensitive hydrogel that swells below temperatures of ~34°C. It does so by undergoing a conformational change that reveals hydrophilic areas within the polymer [144]. When exposed to their transition temperature μTAMs will then expand as a function of surrounding stiffness. Soft local environments allow larger sensor expansion than stiff microenvironments (Figure 4.6A), and due to previous sensor calibration in gels of known stiffness, local tissue stiffness can be measured. Local stiffness within contracting microtissues was measured over 4 days.

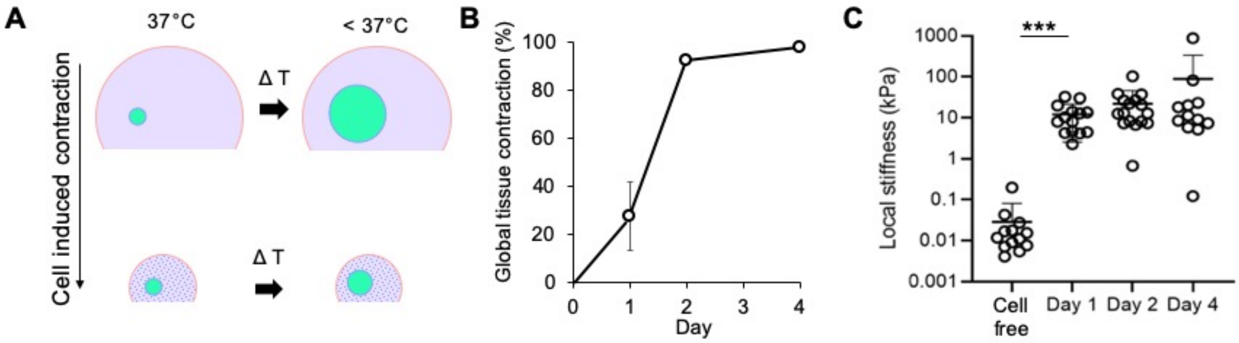

Figure 4.6 μTAM stiffness sensors show local stiffness changes within contracting collagen microdroplets. A) Schematic depicting μTAM stiffness sensors within contracting microtissues. B) Quantified global tissue contraction C) Local stiffness by day as collagen-1 microtissues contract. Statistical analysis presented as mean +/- standard deviation; n = 4 microtissues, 1-6 measurements per tissue; ***p=0.0006, by one-way ANOVA with Kruskal-Wallis post-hoc analysis.

Cell-free collagen local stiffness was measured to be between 0.01-0.1 kPa (Figure 4.6C). By day 1 of contraction, local stiffness dramatically increases to values between 2-30 kPa. Moreover, although local stiffness continues to trend higher past day 1, there is no significant increase in stiffness from day 1 to day 4. This was unexpected, as tissues continue densifying dramatically between these days (Figure 4.6B).

Another notable observation is the large stiffness values reported, with some reaching nearly 1000 kPa. Error increases with measured stiffness in this system (Figure 4.7); however, these unexpectedly high data points still represent values greater than 600 kPa, which is much greater than stromal stiffness reported by others [28] [20] [264] and reflects a tissue stiffness closer to cartilage [22]. The important difference here is that stiffness is being measured within a live and actively contracting tissue. It is likely that a high density of actively contracting fibroblasts provide stiffness values much higher than the surrounding soft matrix, and the contracting cells dominate tissue stiffness. This also explains why a significant increase in stiffness is not seen between days 1-4, as cells have already reached a spread and contractile phenotype by day 1, and the soft matrix simply molds down under the comparatively stiff and active cells.

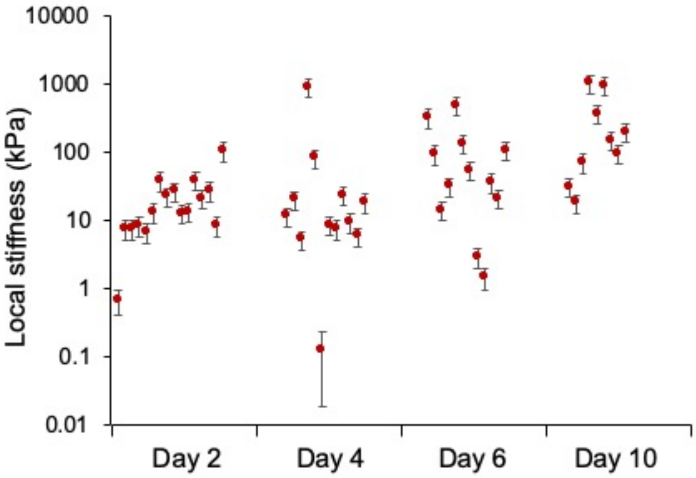

Figure 4.7 Error within each individual local stiffness measurement. Stiffness is plotted for initially soft contracting microtissues measured across days 2- 10; n= 16 microtissues, 1-6 measurements per tissue.

Of notable mention, although significant stiffness increases are not seen past day 1, stiffness does indeed continue trending upwards with global contraction (Figure 4.6C). This is logical, as tissue of higher density is stiffer. This does; however, highlight the minimal impact of the densifying matrix, as compared to the cell's cytoskeletal machinery in determining tissue stiffness, and underscores a need for stiffness measurements to be conducted on live tissue.

4.3.4 Local forces are independent of matrix stiffness

Both 2D substrate stiffness and matrix strain have been shown to promote contraction related structures [9] [258] [184]; however, with local forces correlating well to tissue strain, and local stiffness not correlating well to tissue strain, we wondered if tissue stiffness perhaps plays a minimal role in local forces. To test this, initial tissue stiffness was tuned. Microtissues were alginate-doped to produce interpenetrating networks (IPNs) of collagen and alginate (Figure 4.8A). Alginate concentration was used to increase tissue storage modulus (Figure 4.8B) and crosslinking sites were saturated in all IPNs by exposing tissues to a 1000x molar excess of calcium chloride following previously defined protocols [249].

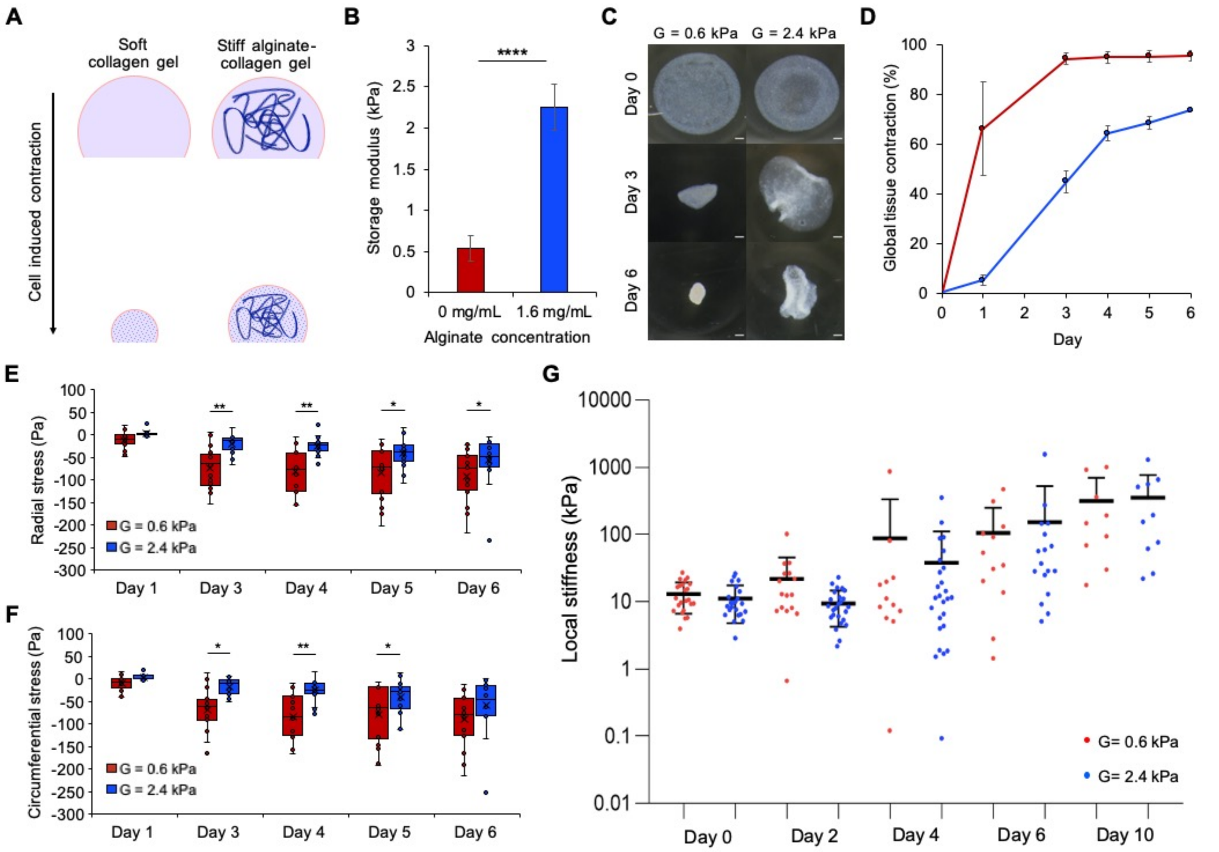

Figure 4.8 Initial matrix stiffness influences on global matrix strain, local forces, and local stiffness. A) Schematic illustrating initially soft and stiffened microtissue contraction. B) Storage modulus of cell-free microtissues with 0 and 1.6 mg/ mL of alginate. C) Representative stereoscope brightfield images and D) quantification of global tissue contraction across the days. E) Radial and F) Circumferential local forces within contracting microtissues. G) Local stiffness within contracting microtissues; Scale= 200 µm. Statistical analysis in B,E,F presented as mean +/- standard deviation; (B) n= 3 gels, minimum of 30 measurements per gel; (E,F) n= 10 initially soft microgels, n=9 initially stiffened microgels, 1-5 measurements per gel. * $p < 0.05$; ** $p < 0.01$; ****$p<0.0001$, by one-way ANOVA with Tukey post-hoc analysis. Statistical analysis in G presented as mean +/- standard deviation; n = 4 microtissues per condition, 1-6 measurements per tissue; by one-way ANOVA with Kruskal-Wallis post-hoc analysis. Figure 4B adapted with permission from Ort C, Chen Y, Ghagre A, Ehrlicher A, Moraes C. Bioprintable, stiffness-tunable collagen-alginate microgels for increased throughput 3D cell culture studies. ACS Biomater Sci Eng. 2021 Jun 14;7(6):2814-2822. doi: 10.1021/acsbiomaterials.1c00129. Copyright 2021 American Chemical Society.

Tissues of higher initial storage modulus strained slower than initially soft tissues (Figure 4.8C,D). While a soft matrix provides less resistance to contraction, it was thought that a stiffened matrix should stimulate contractile phenotypes and therefore increase local forces. On day 1 of contraction however, there are no differences in radial or circumferential forces between initially soft and stiffened matrices (Figure 4.8E,F). On all remaining days of contraction, local radial forces are higher in initially soft tissues compared to stiffened. This is also true for forces in the circumferential direction on days 3, 4, and 5, with the final day again showing no difference in forces between initially soft and stiffened tissues. This finding highlights the presence of an additional driver, other than stiffness, of forces felt at the cellular level within 3D fibrous settings.

Local forces increase from day 1 to day 3 in initially soft tissues, before reaching a plateau from day 3 onwards (Figure 4.9). This compliments global contraction patterns well, as tissues reach maximum contraction by day 3 (Figure 4.8D). Other work has shown 3D fibroblast contraction reaching a plateau [263] [262], suggesting a homeostatic state has been reached. Fibroblasts do indeed adjust their contraction force to maintain a homeostatic tension within the collagen matrix by increasing contraction following tension unloading [265]. Stiffened tissues instead display a slow and steady climb in local forces (Figure 4.9) while continuing to increase in global contraction throughout the 6 days (Figure 4.8D). Initially soft and stiffened matrices show similar spatial force patterns as they increase (Figure 4.10).

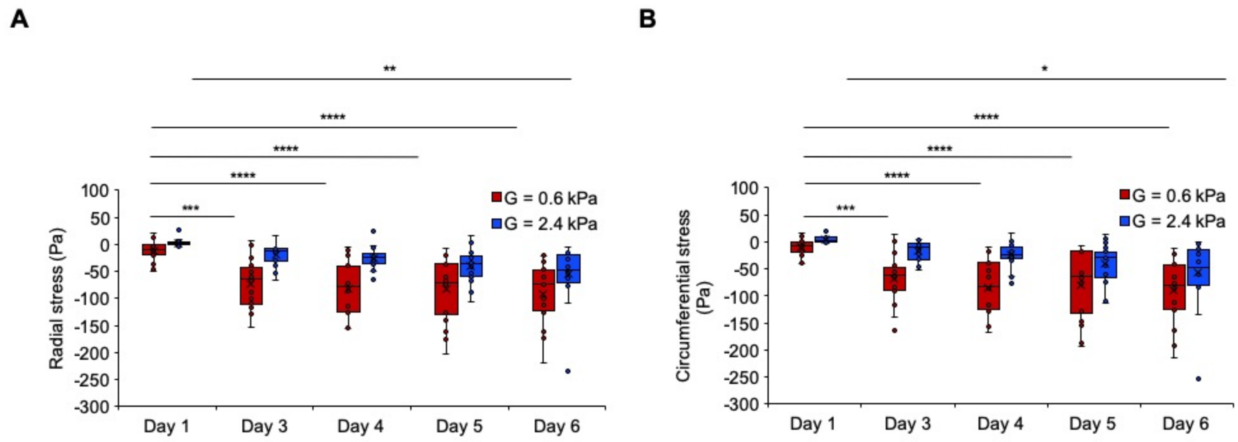

Figure 4.9 Significance trends of local forces compared from day to day within the same initial stiffness condition. Data presented for both A) radial and B) circumferential stresses. Statistical analysis presented as mean +/- standard deviation; n=10 initially soft microgels, n=9 initially stiffened microgels, 1-5 measurements per gel. *$p < 0.05$; ** $p < 0.01$; ***$p=0.0007$;****$p<0.0001$, by one-way ANOVA with Tukey post-hoc analysis.

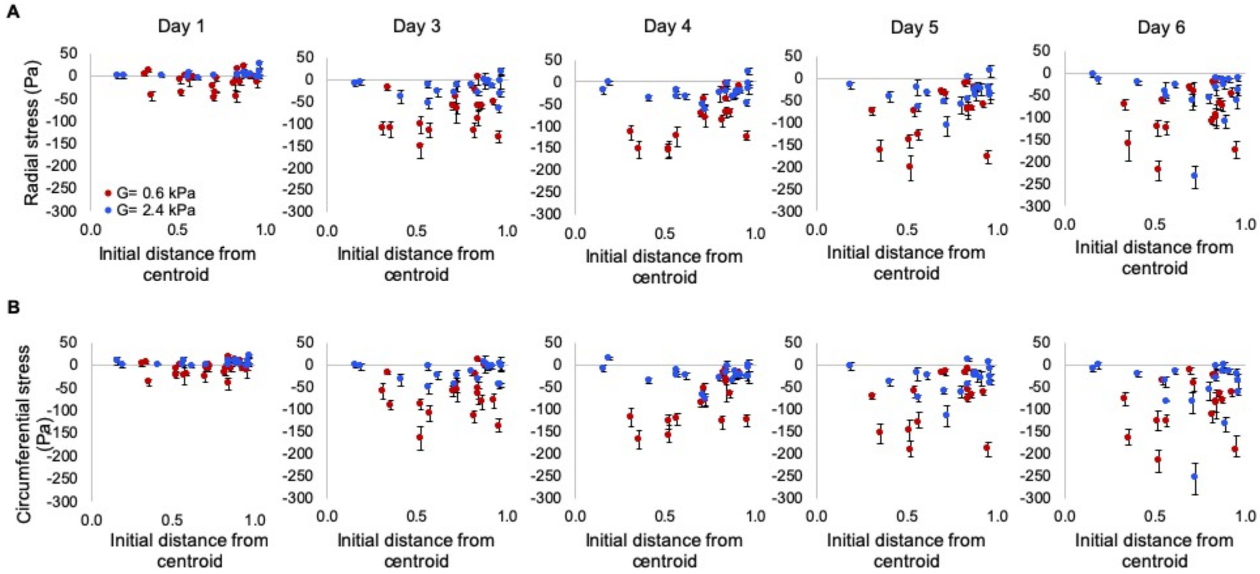

Figure 4.10 Spatial stress patterns arising within initially soft and initially stiff microtissues. Both A) radial and B) circumferential orientations of stress are shown; n=10 initially soft microgels, n=9 initially stiffened microgels, 1-5 measurements per gel.

Since cells have begun remodelling the matrix by day 1, initially measured, cell-free stiffness values can no longer be relied upon. To better understand the role of stiffness on local forces, local stiffness was followed throughout contraction in both initially soft and stiffened tissues. On day 0, immediately after cell seeding, local stiffness does not differ between initially soft and stiffened microtissues (Figure 4.8G). This unexpected result again demonstrates the strong and understated effects of cells in contributing to tissue stiffness: a quality largely attributed to matrix characteristics. Once cells are integrated into the matrix there are no longer significant differences in local stiffness between initially soft and stiffened tissues on any of the days throughout contraction. Intriguingly, local tissue stiffness that arises during contraction appears independent of the initial tissue stiffness. Although local stiffness is slow to significantly increase across contraction due to the high heterogeneity within each day, tissue stiffness is indeed higher when comparing early to late days of contraction (Figure 4.11). Moreover, there is a positive correlation between local stiffness and global tissue contraction (Figure 4.12). This is expected, as denser tissue is stiffer [20]. However, local forces are different between initially soft and stiffened tissues on days 3,4, and 5, while local stiffness is the same between conditions from day 2-6, suggesting that local stiffness is not a major driver of local forces.

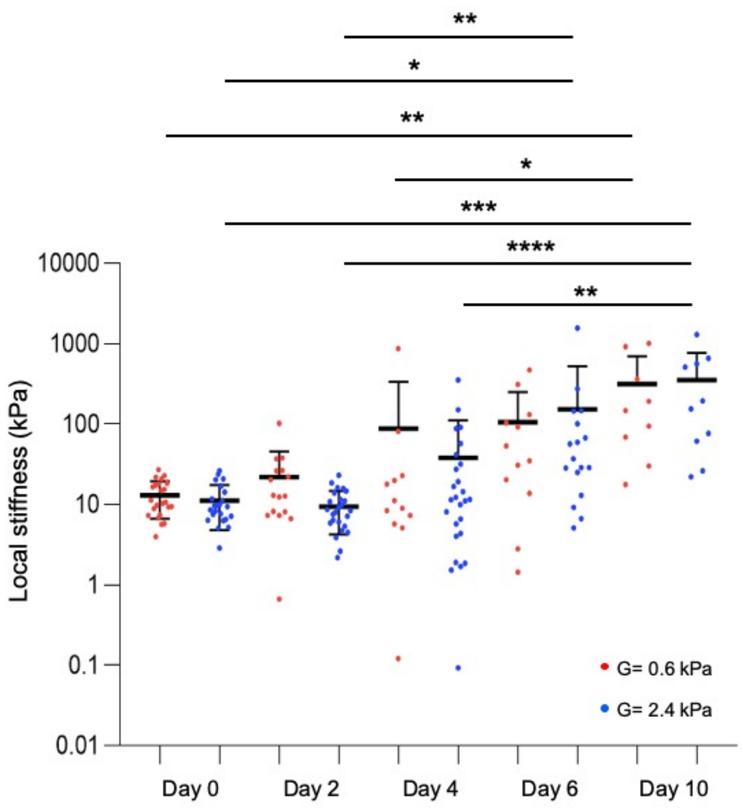

Figure 4.11 Significance trends of local stiffness compared from day to day within the same initial stiffness condition. Statistical analysis presented as mean +/- standard deviation; n = 4 microtissues per condition, 1-6 measurements per tissue; *p < 0.05; ** p < 0.01; ***p=0.0002; ****p<0.0001 by one-way ANOVA with Kruskal-Wallis post-hoc analysis.

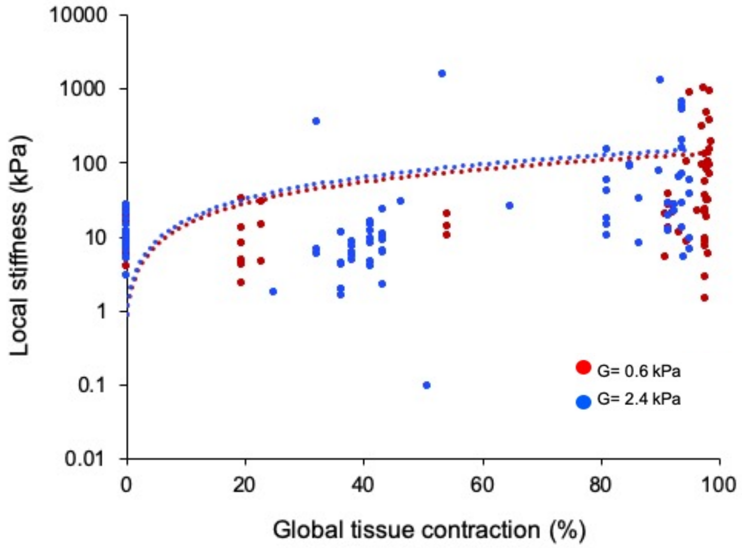

Figure 4.12 The relationship between local stiffness and global tissue contraction for both initially soft and initially stiff microtissues. Fits are linear to display positive correlations; R^2= 0.1026 and y=1.3743x + 0.8771 for G= 0.6 kPa; R^2= 0.0583 and y=1.597x + 0.9068 for G= 2.4 kPa; n= 20 microtissues per condition, 1-6 measurements per tissue.

4.3.5 Cell-induced forces in both soft and stiff matrices correlate with local tissue densification

Since local stiffness does not appear to be driving local forces, this then re-instates the idea that local strain could be driving local forces and possibly cell contractility in a 3D fibrous system. Local forces had previously corresponded well with local tissue densification in initially soft matrices, so this relationship was further compared between initially soft and initially stiff matrices.

By day 1 of contraction, local forces for both initially soft and stiffened tissues are low (Figure 4.8E,F) and local tissue densification is correspondingly low (Figure 4.13A,B,C). By day 3, local tissue densification has greatly risen in initially soft tissues (Figure 4.13A,B,C), and local forces reflect this rise (Figure 4.8E,F). Initially stiffened tissues however, have not yet undergone local remodelling to the extent of the initially soft tissues (Figure 4.13A,B,C) and local forces again reflect this, remaining lower than initially soft tissues (Figure 4.8E,F). By day 6, local densification of stiffened tissues has increased although has not yet reached the same level as initially soft tissues (Figure 4.13A-C), and radial forces reflect this, remaining statistically different between the two (Figure 4.8E,F). Although fluorescent intensity line plots are heterogeneous, they remain relatively consistent within each condition (Figure 4.14).

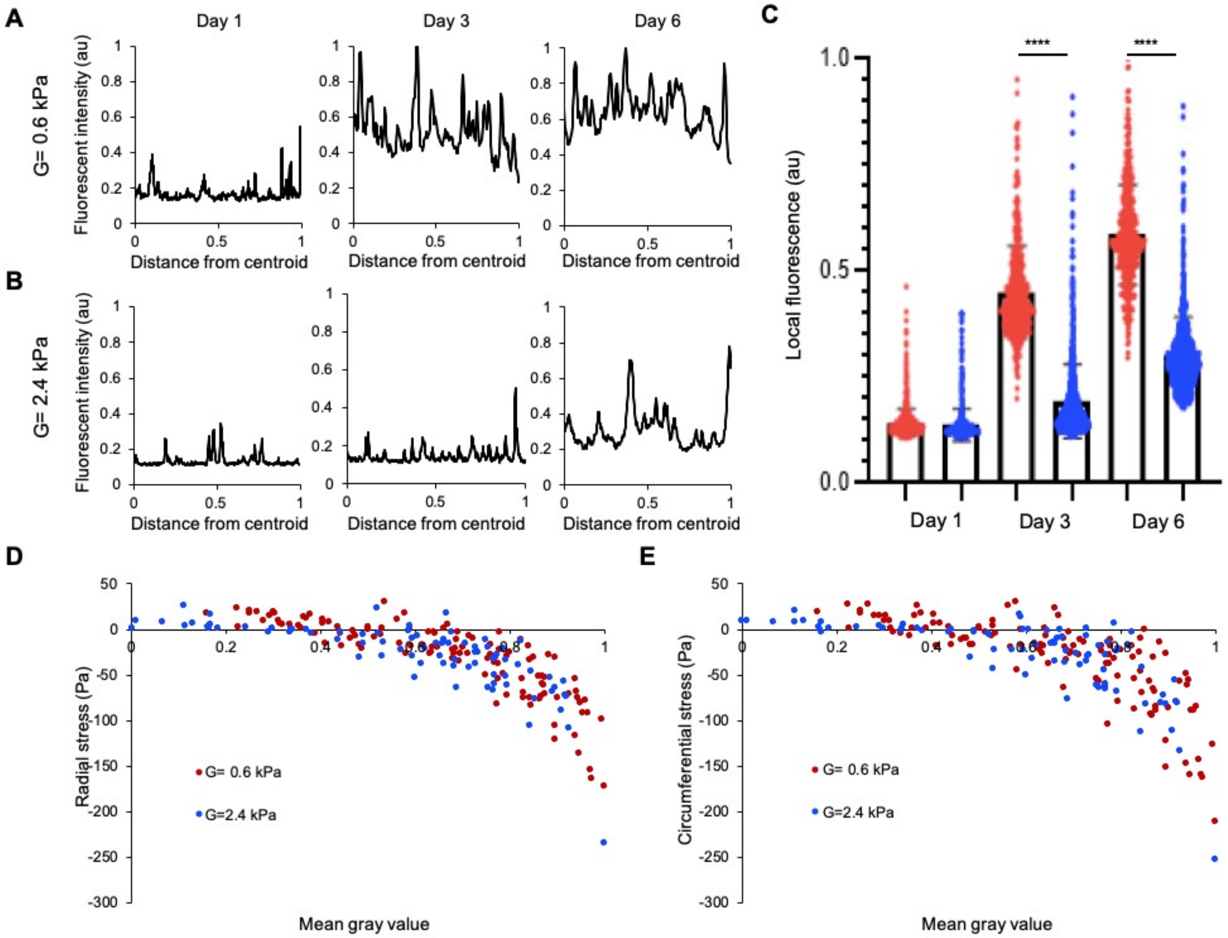

Figure 4.13 Local tissue densification in initially soft and stiffened microtissues during contraction and their correlation with local forces. A) Representative fluorescent intensity line plots through A) initially soft and B) stiffened contracting microtissues. C) Comparison of averages of fluorescent intensity within initially soft (red) and stiffened (blue) microtissues throughout contraction. Correlation of D) radial and E) circumferential stresses plotted against the local mean gray values for both initially soft and stiffened microtissues. Statistical analysis in C presented as mean +/- standard deviation; n = 4 microtissues per condition, 540-1530 measurements per tissue; ****$p<0.0001$, by one-way ANOVA with Tukey post-hoc analysis.

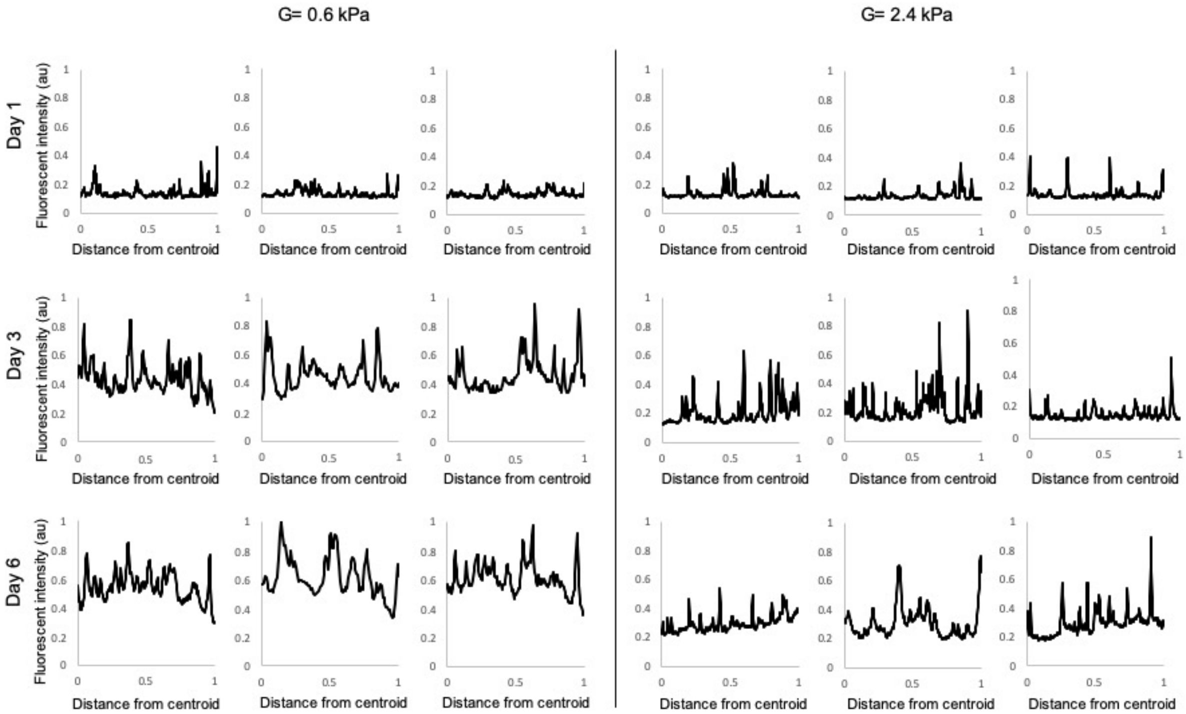

Figure 4.14 Fluorescent intensity line plots through 3 different contracting microtissues of both initially soft (left) and initially stiff (right) mechanics. Data is presented for days 1 (top), 3 (middle), and 6 (bottom).

Because stiffened tissues contract slower than initially softer tissues, we wanted to eliminate this time variable and plotted local forces against local tissue darkness: our surrogate for local tissue density. Strikingly, both initially soft and initially stiff tissues fell along nearly identical curves (Figure 4.13D,E), demonstrating that local forces are dependent on local tissue densification and independent of initial tissue stiffness.

Trends of global tissue strain follow similarly those of local tissue densification, with the exception of early days of contraction. In initially soft tissues, local densification has only begun at the tissue edge by this timepoint (Figure 4.3D). As the tissue edge comprises the highest surface area, densification of the edge gives rise to the large change in area reflected in global contraction (Figure 4.8D). Notwithstanding this, global contraction also correlates well with local forces within both initially soft and stiffened tissues (Figure 4.15). Forces from the two tissues again collapse together along highly similar lines with near identical slopes. Here, a linear fit was chosen simply to demonstrate the increasing forces with increasing global tissue strain. Together, this data suggests a strong dependence of local force on tissue strain, both at the local and resulting global level, irrespective of initial stiffness.

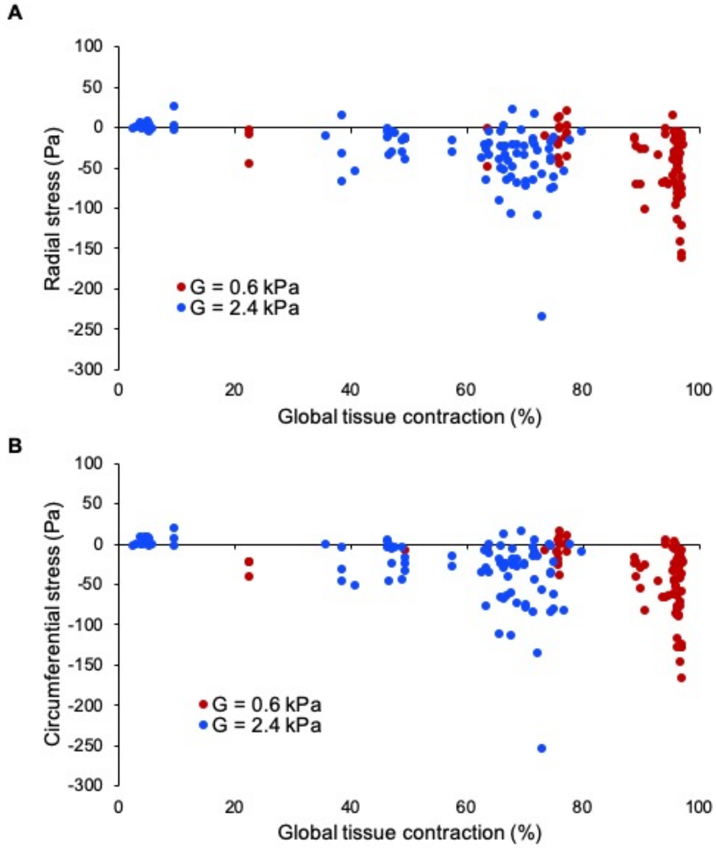

Figure 4.15 The relationship between local forces and global tissue contraction for both initially soft and initially stiff microtissues; n=10 initially soft microgels, n=9 initially stiffened microgels, 1-5 measurements per gel.

4.4 Discussion

This first look into the local cell-generated forces and simultaneous local stiffness within dynamic tissue contraction illustrated the extreme heterogeneity in an otherwise relatively homogenous system. This demonstrates that minute differences in features such as local cell or collagen fiber arrangement may give rise to large differences in locally felt forces. The activity of surrounding cells can also contribute to the heterogeneity seen, as local forces within spheroids lacking substantial collagen content are also heterogeneous [266] [198] and fibroblasts contract with periodic fluctuations of force [267].

Forces increased across the days which could be explained by three tied cellular cues in this system: matrix strain, local cell density, or local collagen-1 density. External strain on fibroblasts causes higher myofibroblast populations [268], with smooth muscle actin expression [184], and stimulates activated phenotypes such as TGF-β and ECM secretion [185]. A higher cell density could also be contributing to the higher forces, as a sensor sized area transitions from receiving the contractile forces of about 3 cells, to that of being completely surrounded by cells, thereby increasing contractile forces locally. Finally, large strains cause higher collagen density in our system, and could also give rise to the increase in forces seen. In a fibrous matrix, cell-induced strain can lead to long-term changes in local fiber architecture [180] [206], thereby changing local ligand density. Binding ligand availability is a driver of focal adhesion formation, promoting cell spread, and actin structure growth [44] [269] [270] [53] [236].

Spatially, there were no differences in contractile forces from the center to the outside of the tissues. This result was particularly interesting, as contraction assays showed a reproducible outside-in contraction phenotype where the external edge of the tissue densified first. Tissues also appeared to warp around a stationary center (data not shown), which should only occur with force differences between central and outer locations. Moreover, literature demonstrates fibroblasts being more activated at tissue edges [248]. To explain this discrepancy, there is a slight trend of decreasing forces from the outside to the inside of the tissue, although statistically insignificant. The heterogeneity in forces may mask significant differences and could explain the documented phenotype of edge activation in fibroblast systems. Moreover, fewer measurements were possible at the most central region of the tissues, which may bias the spatial mapping.

Surprisingly large stiffness measurements that do not significantly correspond with day-to-day global contraction rates suggest that active contractile cells dominate local stiffness rather than the local collagen density. This is consistent with AFM measurements of local collagen fibers, around 0.9 kPa [271] and fibroblast stiffness reaching 45 kPa in highly local areas [272]. Moreover, once cells are present within a matrix, there are no longer stiffness differences between initially soft and initially stiff tissues on any day, when comparing the same timepoint (Figure 4.8G). Compellingly, this includes stiffness on day 0 when cells have not yet had time to spread. In fact, initially soft matrices increase in stiffness by almost 3 fold with cells embedded, as compared to cell-free matrices, suggesting that once adhered, cells of contractile origin have prepped actomyosin machinery that can withstand external forces. Cell-induced contractile forces have been shown to increase from zero immediately after seeding, with measurable forces present even within 1 hour [262], demonstrating that cellular machinery contributing to stiffness is already active.

Exploring the influence of stiffness over contraction, on most days of tissue contraction, initially soft tissues contain larger forces than initially stiffened tissues. It is likely that a decreased cell spread area that arises from a stiffened fibrous 3D matrix [249] contributes to this dampened contraction. Stiffened tissues have also not undergone the same degree of tissue strain as the initially softer tissues at this timepoint. However, when local forces are compared against local tissue densification at the sensor site, initial matrix stiffness does not impact either radial or circumferential forces at a given local tissue density. When investigating the relationship between local forces and local stiffness, forces are again independent of stiffness. Others have shown fibroblast contractile forces to be time dependent and non-mechanosensitive [273]. This study followed PDMS pillar deflection by cells across various PDMS pillar stiffnesses and found that multiple different cell types displace the pillars to the same degree as a function of time, irrespective of pillar stiffness. Together, this evidence suggests that stiffness is not a dominant driver of local forces, particularly within a fibrous tissue, and has implications in fibrotic disease, as high matrix stiffness may be less important to a contractile myofibroblast phenotype than previously thought.

Rather than local stiffness, local tissue strain appears to play a dominant role in local forces, as local densification correlates well with the local forces arising in each respective matrix (Figure 4.13). This is especially relevant in a cell dense setting, where cells are exposed to strains from the contractions of neighbouring cells. Strain upon cells drives smooth muscle actin expression, and does so independently of matrix stiffness [184]. Matrix strain also promotes inflammatory cell migration into tissue [274], further exaggerating fibrotic disease. Further, high matrix strain allows fiber recruitment to a cell's immediate local setting and increases local binding ligand availability. Fiber recruitment has also arisen as a strong driver of focal adhesion formation and behaviours relevant to contraction such as cell spread and stress fiber presence [53] [269] [275] [270].

This culture system has some limitations that should be considered. First, local force measurements could be a result of two different contractile scenarios. Force sensors are functionalized with collagen-1, allowing direct contact and wrapping of fibroblasts around the beads and thereby providing a direct measure of contractile forces. However, local measurements may also be indirect if collagen fibers are positioned between the sensor and the cell during the measurement. The force measurements here likely reflect a combination of both scenarios. An analogy for the system can be a soft ball, representing the sensor, surrounded by a loose mesh, representing the matrix. While squeezing this mesh encased ball, some fingers easily contact the ball directly, while some must compress the mesh in order to compress the ball. Due to this, measurements may not be exclusively measuring contractile forces of the cells themselves, as the surrounding matrix may resist bead deformation and also has nonlinear properties, therefore stress cannot be calculated from the strain. However, these measurements do reliably represent the force microenviroment felt by cells, which drives cell phenotypes.

Another limitation within our system is that tensional readings may be more impacted by the surrounding collagen matrix than compressional readings. Using a similar analogy, stretching a soft ball in a relatively stiffer matrix may prevent full expansion of the ball. On the other hand, compressing a soft ball in a stiff matrix is possible because the matrix is not limiting the size change. This limitation is not a concern for the conclusions drawn here, as most measurements are compressional. Only the few tensional stresses that arise during early days of contraction should be viewed as potentially under reported.

Some limitations also arose with the µTAM stiffness sensors. Anisotropic stiffness is present within this culture setting at highly contracted tissue states. Since µTAMs were not designed to measure anisotropic stiffness, isotropic stiffness was assumed, adding error to the measurements.

While this error challenges absolute stiffness readings, it does reliably allow the relative comparison of stiffness from one location to another, validating the conclusions made here. Moreover, this error can be corrected for future studies by developing a model specific for anisotropic measurements. Finally, the expansion of the beads during transition swelling may affect the cells themselves, and cells may contract back against the expanding sensor, giving rise to higher stiffness measurements. This may not be a disadvantage to the system however, as the average bead expands about 20 µm over 30 mins [144], representing the migration of an adjacent cell [269] and maintaining relevance in the findings.

4.5 Conclusions

Tissue contraction is a highly heterogeneous mechanical process in terms of local forces, local tissue densification, and local stiffness. Local forces increase across the contraction timeline until a plateau is reached, and local tissue densification correlates with these forces. Local tissue stiffness appears to be dominated by active contractile cells, rather than extracellular matrix density. Moreover, stiffening tissues with alginate causes lower local forces day-by-day than initially softer tissues. Local stiffness does not differ between initially soft and initially stiff tissues on any day throughout contraction. Stiffness is therefore not a dominant driver of local forces within a 3D fibrous live tissue. Instead, local tissue densification for both initially soft and initially stiff tissues correlate together along the same curve with local forces, highlighting that local forces arising within 3D fibrous tissues are intrinsically tied to local strain.

Chapter 5

Comprehensive Discussion

To begin a comprehensive discussion on cell spread, an overarching cell phenotype important to each of my research chapters, I first orient the reader by providing a brief background describing how matrix stiffness and strain independently drive focal adhesion formation and ultimately cell spread. I then discuss cell spread within the specific mechanical context of each research chapter, and describe how the dual importance of these two unique mechanical cues may be the driving mechanism behind stable cell spread and the pronounced contractile phenotypes seen here.

5.1 Matrix stiffness and strain together regulate cell spread

Across each research chapter presented, focal adhesion formation and cell spread are two intrinsically tied cell reactions to the surrounding microenvironment that can be used to cohesively discuss and explain each major cellular phenotype seen. Cell spread is a standard readout in engineered culture models because it is often a measure of cell health and attachment, and is also upstream of many important and fundamental cell functions. Tissue contraction specifically, is fundamentally coupled to cell spread in the matrix. Contraction of a 3D matrix is thought to occur by two main cellular mechanisms: traction forces during cell migration and cell body contraction [1], both of which mechanisms benefit from larger cell spread. Furthermore, cell spread directly regulates RhoA and ROCK activation, two intracellular signalling molecules upstream of actin structure growth, migration, and cell traction forces [276]. Cell spread is coupled to other contraction related behaviours such as actin-myosin based contractility through the intracellular signalling pathway of focal adhesion kinase (FAK), arising from focal adhesion growth [277 278]. Focal adhesions are large integrin-based protein complexes at the cell-extracellular matrix (ECM) interface that act as regulatory centers upstream of cell spread, contractility, and smooth muscle actin expression [252 278 279]. Focal adhesions promote pathways such as actin polymerization, which are necessary for cell spread, migration, and importantly, contraction [280]. This therefore makes cell spread an easy primary functional readout suggesting focal adhesion formation and downstream contraction related signalling pathways.

The mechanical microenvironment is a known driver of focal adhesion formation, cell spread, and other contraction related cell behaviours. Cells are able to transduce their external mechanical environment into internal biochemical signals that direct downstream cellular responses. This is due to a variety of mechanosensitive elements within the cell [280]. Proteins at the cell-ECM interface are mechanosensitive, undergoing conformational changes under mechanical stress. Stress activated ion channels are able to sense membrane tension. Nuclear deformation as a result of mechanical stress transmission from the cytoskeleton to the nucleoskeleton may also influence gene expression directly [281]. Together, these mechanosensitive proteins allow the cell to sense and respond to mechanical stimuli such as matrix strain and microenvironment stiffness. Microenvironment stiffness and matrix strain are the two major cellular cues discussed here, to drive focal adhesion formation and downstream cell spread.

5.1.1 Matrix Stiffness

On a stiff 2D hydrogel surface, cells are typically well spread with stable focal adhesions and stress fiber formation, while the opposite is seen on soft substrates [277] [236] [259] [93] [53]. These studies began the notion that stiff substrates direct focal adhesion stability and downstream cell behaviours such as high cell spread.

The motor clutch model is a theoretical 1D model that well explains the mechanism for which substrate stiffness drives cell spread. Cells adhere to their surroundings through integrin based cell-to-ECM bonds (Figure 5.1), called the clutch [282] [283] (Handorf et al. 2015). These bonds connect the external environment to the cell's internal filamentous actin cytoskeleton, thereby anchoring the cell (Figure 5.1). The internal actin cytoskeleton is dynamic and as the cell anchors and pulls on its surroundings, tension is built at the cell-ECM interface, thereby generating force on the clutch [277] [282]. A soft external environment displaces easily during cell-induced force, leading to lower tension on the clutch. A stiff substrate on the other hand, resists movement, leading to high tension on the clutch. High enough tension engages the clutch by causing an intracellular mechanotranducing protein to unfold [284]. This unfolding reveals a binding site for another protein to enter, building the protein complex and promoting focal adhesion growth. This model therefore explains how high stiffness results in focal adhesion formation and cell spread, as a high enough material resistance is needed to engage the molecular clutch [283].

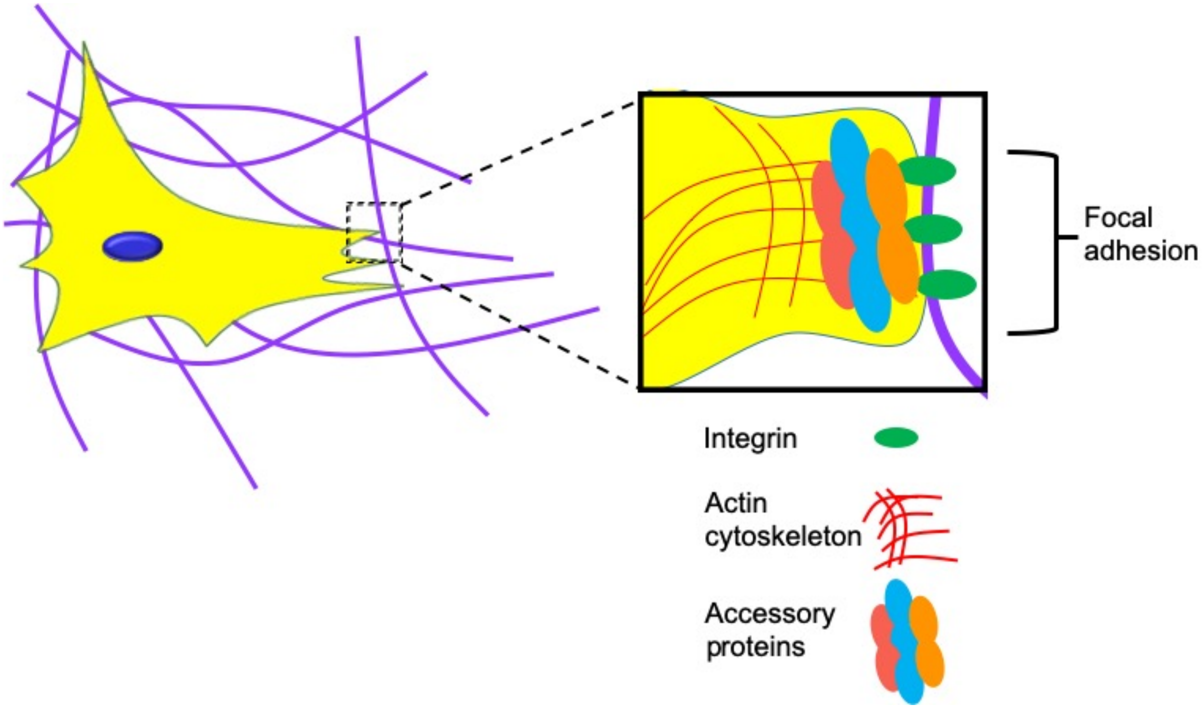

Figure 5.1 The focal adhesion. Focal adhesions are large protein complexes that result from integrin clustering, and further accessory protein recruitment at the cell-ECM interface. They provide stable anchorage to the external microenvironment and regulate important signalling cascades for downstream cellular contraction.

However, as mechanical culture models evolve to incorporate physiologically relevant extracellular matrix fibers, the relationship between stiffness and cell spread becomes less straightforward. Within a fibrous, stiffness tunable culture model, a stiff matrix limits focal adhesion formation, cell spread, and migration, while a soft matrix promotes these behaviours [53] [119] [107] [233], reversing the prior trend. Moreover, other contractile cell behaviours coupled to focal adhesion formation, such as YAP/TAZ signalling, and α-smooth muscle actin expression are also higher in soft, deformable matrices as opposed to stiff [120]. Together, this underscores the idea that stiffness is not the sole contributor to focal adhesion formation and contraction related behaviours. Instead, there must be another factor driving them.

5.1.2 Matrix Strain

Ligand recruitment to the cell interface as a result of matrix strain also drives focal adhesion formation and downstream contractile phenotypes. This includes engineered matrices with either a fast relaxation rate or permanent matrix deformation, that both allow fiber recruitment [172 174 179]. The suggested reason for this phenomenon is that matrix strain allows binding ligand clustering, and ligand density also drives focal adhesion formation, cell spread, and other contraction related cell behaviours. This is typically a positive relationship, where high ligand density drives these behaviours across various unique culture models [269 275 270 53 44 285]. Work has suggested a critical ligand spacing under 70 nm for focal adhesion formation [270], with increasing density further increasing cell spread and migration up to a plateau [269 275], with some studies demonstrating decreased spread past a threshold density [236 286].

The most fundamental and physical reason for these observations is contact guidance. Too sparse a binding ligand density would not allow cells to physically extend out and attach to a high number of ligands. However, this does not fully explain the 2D nanopatterned studies, particularly the necessity of >70 nm for focal adhesion formation, which is much smaller than the length of an extended cell [287]. Here, these observations demonstrate the necessity of integrin clustering for focal adhesion formation and downstream cell behaviours. Integrin clustering is tightly linked to focal adhesion formation and growth, thereby promoting the same signalling cascades discussed above that promote actin polymerization and spreading [252 278]. The impact of clustering is nicely demonstrated when RGD ligands were engineered at the end of tethers (Griffith and Lopina 1998). Longer tether lengths, allowing the clustering of RGD, contributed to larger spread. Moreover, RGD cluster size greatly influences migration speed, with ligand clustering a requirement to reach maximal speed [269]. This clustering process has also been modelled, where focal adhesion formation occurs as a result of densification of mobile cell surface receptors within a fluid membrane, to match static extracellular ligands at a set density [287].

To apply these ideas to culture models, hydrogel surfaces contain small enough pores that, depending on the density of functionalization, the distance between ligands is within the threshold for focal adhesion formation [100]. Cells can therefore cluster their integrins and spread across the surface. Here, ligand density is not a limiting factor and surface stiffness thus drives cell spread. A fibrous 2D or 3D network on the other hand, restricts cells to finite tracts, resulting in larger distances between adjacent proteins, as pores in fibrous structures are larger [233]. Since a threshold binding ligand density is crucial for focal adhesion formation [270 236 44], the ability of a cell to stably spread in a fibrous environment therefore depends on its ability to deform the fibers and recruit the ligands to the immediate cell surface [53] (Figure 5.2). In fibrous microenvironments, it is therefore strain of matrix fibers that allows ligand clustering, focal adhesion formation, and contraction related behaviours [174 172 177].

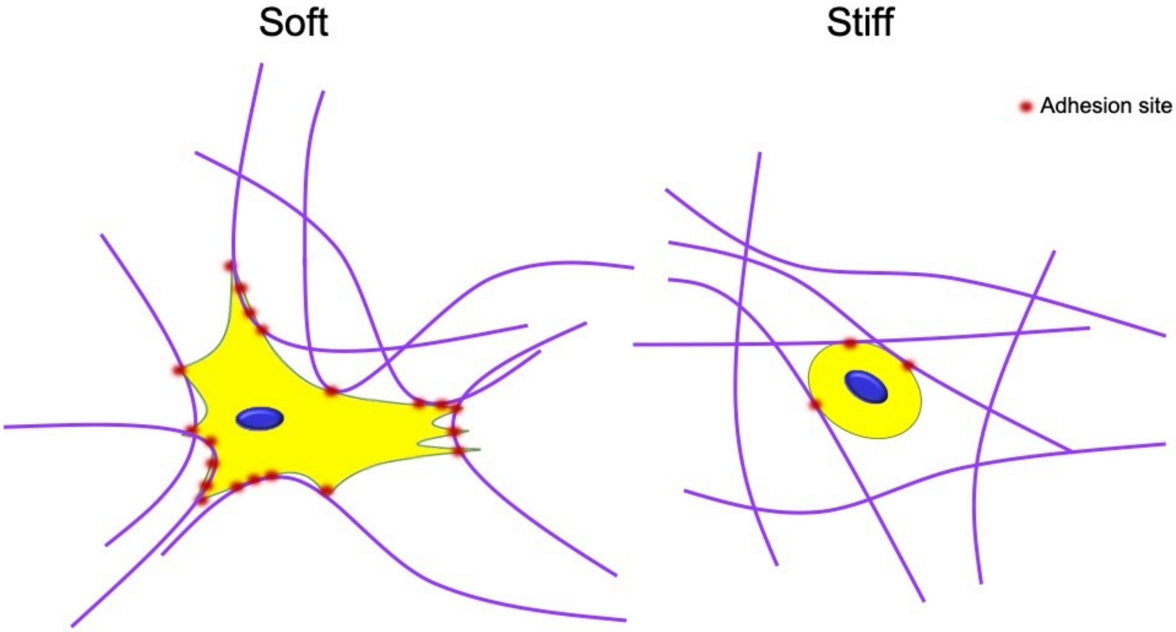

Figure 5.2 Fiber strain allows cell spreading. A soft fibrous microenvironment provides the necessary mechanical parameters for ligand recruitment to the cell surface, and therefore increased adhesion sites and cell spread, while a stiff fibrous microenvironment limits this process.

5.2 Matrix stiffness controls matrix strain and cohesively explains thesis chapters

To explain the contractile cell behaviours arising from unique mechanical microenvironments within my culture platform, both cellular cues must be considered: matrix stiffness and strain. Here, I suggest that these two signals work co-operatively to drive cell phenotypes within my tissue contraction models. This dynamic interplay between cell-induced forces on mechanical substrates and substrate remodelling has been computationally modelled, confirming this idea [288]. If both signals are considered together, cell spread in each unique mechanical setting can be explained.

In the biomaterials presented in this thesis, the softest matrix promoted the largest cell spread, while stiffening the matrix limited spreading (Figure 2.5). Here, although cells in a stiff fibrous environment are receiving the stiffness cue, stiff surroundings prevent matrix strain, limiting the cell to the finite number of adhesive ligands immediately surrounding it and minimizing ligand clustering. It is therefore likely that low focal adhesion formation is occurring in these stiffened cultures, and downstream cell spreading stability is jeopardized. Indeed, stiff fibrous cultures cause decreased focal adhesion formation and cell spread across other work [53] [119] [107] [233]. On the other hand, fibroblasts cultured in matrices stiffened by increased collagen density show larger spread [289]. In this case, the increased stiffness is likely balanced by an increased availability of ligands, allowing the cell to spread. Alternatively, it is also possible that differences between bulk and local stiffness may play a role in the ability to recruit local fibers. Synthetic methods to increase stiffness often involve covalent welding between polymers in the fibrous network, increasing both bulk and local stiffness, and severely limiting the cell's ability to recruit fibers. While increasing fiber density increases bulk matrix stiffness, fibers may be able to slide past each other as the cell pulls, and cellularly perceived local stiffness may still be soft enough to recruit fibers.

Within my biomaterials, F-actin intensity grew stronger as the IPN got stiffer (Figure 2.5, 2.10). This suggests that the mechanical cue of stiffness alone is sufficient to promote dense actin structure formation, and high matrix strain is not necessary to elicit this pathway. Contraction rates were highest in the softest IPNs, and decreased in stiffened matrices (Figure 2.11). This therefore suggests that cell spread is more important to tissue contraction than intracellular F-actin density.

Cell spread was organized circumferentially at the tissue periphery (Figure 3.7), likely resulting in the pronounced strain seen at the tissue edge (Figure 3.1). Fibroblasts are known to activate along tissue boundaries, demonstrating higher F-actin density and smooth muscle actin expression [248]. Matrix fiber tension is highest at this boundary, as a result of cellular contraction [248]. This higher tension at the tissue boundary, caused by matrix strain, likely results in the common phenomenon of biomaterial strain stiffening. Strain stiffening is the increase in stiffness of non-linearly elastic biomaterials under mechanical strain [290]. Due to this phenomenon, cells likely perceive an increased matrix stiffness at the tissue periphery within my microgels. Since matrix strain is occurring at this location, allowing fiber recruitment to the cell, and resulting in further matrix stiffening, a synergistic combination of both matrix strain and stiffness signalling cues may be occurring along the tissue perimeter. Enhanced focal adhesion formation, due to this combination of matrix signals is therefore possible. This may hence be why minimal increases in tissue free boundary area lead to the drastic increases in tissue contraction rates seen (Figure 3.5, 3.6).

Within contracting tissues, higher local forces correlated with local regions of increased strain (Figure 4.13). Moreover, when tissues were stiffened, local strains were lower than initially soft tissues, and local forces were correspondingly lower (Figure 4.13). This suggests that matrix strain is the dominant signal over matrix stiffness, in driving focal adhesion formation and downstream cell behaviours. This is also supported in a 2D culture model that demonstrated stem cell spread and differentiation to be independent of PDMS stiffness, but dependent on polyacrylamide stiffness [285]. This study suggested that ligand density as a result of polyacrylamide pore size is instead the dominant signalling cue, rather than stiffness.

Together, the results presented in this thesis suggest matrix strain as a dominant mechanical cue in driving cell spread, local cell-induced forces, and global contraction rates. This is likely a result of matrix strain allowing fiber recruitment to the cell body, focal adhesion growth, and downstream signalling cascades.

5.2.1 Future Directions

Presented here are biomaterials with both stiffness and free boundary area tunable properties; however, there are other recognized mechanical cues responsible for driving the fundamental cell behaviours seen in this thesis. Viscoelasticity refers to the ability of a material to dissipate internal mechanical stress over time and is often a driver of fundamental cell behaviours such as cell spread, proliferation, migration, and differentiation [172 176 174 177]. This mechanical property is highly tissue relevant, and the ability to tune viscoelastic properties such as stress relaxation rate or phase angle (discussed in chapter 1) in a high throughput manner could be beneficial to academic and industry settings. Mechanical plasticity is another tissue relevant mechanical cue responsible for driving cell spread and migration [183 179 291]. Adaptation of the platform for viscoelastic or plastic control may only require modification to biomaterial recipes, and implementation could be straightforward.

A specific and strong future direction for this increased throughput culture platform is its integration into high throughput drug discovery workflows. The drug discovery pipeline suffers inefficiencies due to early investments into drugs that ultimately fail clinical trials [12]. This reality is logical considering the standard initial screening protocols for drug efficacy and toxicity are conducted on stiff, 2D, tissue culture plastic [187] that does not contain the known fibrous, 3D, and physiological stiffness cues that drive disease dependent cell behaviours [38]. This platform may hence provide a potentially feasible solution to achieving higher accuracy in successful drug recognition, while simultaneously maintaining the rigorous speed, cost, and robustness necessary for high throughput screening.

Another future avenue for this culture platform is its use in *in vitro* mechanical models that contain high biological heterogeneity and would benefit from increased throughput for more reliable conclusions. A specific example is organoid culture models, many of which are mechanosensitive [223 222].

Finally, mechanical strain has been highlighted here as a potential dominant cellular cue contributing to the cellular phenotypes seen across each research chapter. It would be interesting to explore this further, controlling for the variable of strain independently. For example, the experiments conducted in this thesis cannot differentiate between externally applied matrix strain on a cell as a result of neighbouring contractile cells, versus matrix strain by a cell that allows binding ligand recruitment to that particular cell. Although contractile cells contribute to both processes, the cellular cue resulting from each scenario differs significantly. External matrix strain is strictly a mechanical signal, while ligand recruitment is a biochemical signal resulting from matrix mechanical properties. A possible experiment to dissect the independent role of external matrix strain may be to apply local strain within the matrix on day 0 by incorporating a high density of cell-sized magnetic beads and exposing the culture to a magnetic field for a designated period of time. Contraction rates could then be analyzed and the impact of local, external mechanical strain on contractile phenotypes could be determined.

Chapter 6

Concluding Remarks

The work presented herein successfully designed and characterized a robust 3D tissue contraction platform capable of tuning two independent mechanical cues: tissue geometry and initial tissue stiffness. The increased throughput culture platform design has the potential to improve mechanical cultures in many fields, including drug development where improved *in vitro* screening models are crucially needed.

Tissue free boundary area was discovered to drive global tissue contraction rates, a variable not currently considered for proper control in highly common tissue contraction assays. This work may hence lead to more robust and reliable contraction assays in the future.

The local mechanics within a dynamically contracting tissue were defined in this thesis, and initial tissue stiffness was found to control local matrix strain, with high matrix stiffness thereby decreasing local, cell-induced forces, while high matrix strain arose as the dominant mechanical cue for higher local force generation and faster contraction rates. This finding therefore begins shifting the focus from mechanical stiffness to mechanical strain as a leading mechanical cue in fibrous tissue culture, and therefore more physiologically relevant tissues.

Chapter 7

Complete References

(1) Grinnell, F.; Petroll, W. M. Cell Motility and Mechanics in Three-Dimensional Collagen Matrices. *Annu. Rev. Cell Dev. Biol.* **2010**, *26* (1), 335–361. https://doi.org/10.1146/annurev.cellbio.042308.113318.

(2) Loganathan, R.; Rongish, B. J.; Smith, C. M.; Filla, M. B.; Czirok, A.; Bénazéraf, B.; Little, C. D. Extracellular Matrix Motion and Early Morphogenesis. *Dev. Camb. Engl.* **2016**, *143* (12), 2056–2065. https://doi.org/10.1242/dev.127886.

(3) Hinz, B.; McCulloch, C. A.; Coelho, N. M. Mechanical Regulation of Myofibroblast Phenoconversion and Collagen Contraction. *Exp. Cell Res.* **2019**, *379* (1), 119–128. https://doi.org/10.1016/j.yexcr.2019.03.027.

(4) Mailand, E.; Li, B.; Eyckmans, J.; Bouklas, N.; Sakar, M. S. Surface and Bulk Stresses Drive Morphological Changes in Fibrous Microtissues. *Biophys. J.* **2019**, *117* (5), 975–986. https://doi.org/10.1016/j.bpj.2019.07.041.

(5) Wells, R. G. Tissue Mechanics and Fibrosis. *Fibros. Transl. Basic Res. Hum. Dis.* **2013**, *1832* (7), 884–890. https://doi.org/10.1016/j.bbadis.2013.02.007.

(6) Kalluri, R.; Zeisberg, M. Fibroblasts in Cancer. *Nat. Rev. Cancer* **2006**, *6* (5), 392–401. https://doi.org/10.1038/nrc1877.

(7) Li, L.; Eyckmans, J.; Chen, C. S. Designer Biomaterials for Mechanobiology. *Nat. Mater.* **2017**, *16* (12), 1164–1168. https://doi.org/10.1038/nmat5049.

(8) Boghaert, E.; Gleghorn, J. P.; Lee, K.; Gjorevski, N.; Radisky, D. C.; Nelson, C. M. Host Epithelial Geometry Regulates Breast Cancer Cell Invasiveness. *Proc. Natl. Acad. Sci. U. S. A.* **2012**, *109* (48), 19632–19637. https://doi.org/10.1073/pnas.1118872109.

(9) Balestrini, J. L.; Chaudhry, S.; Sarrazy, V.; Koehler, A.; Hinz, B. The Mechanical Memory of Lung Myofibroblasts. *Integr. Biol.* **2012**, *4* (4), 410–421. https://doi.org/10.1039/c2ib00149g.

(10) Gomez, E. W.; Chen, Q. K.; Gjorevski, N.; Nelson, C. M. Tissue Geometry Patterns Epithelial-Mesenchymal Transition via Intercellular Mechanotransduction. *J. Cell. Biochem.* **2010**, *110* (1), 44–51. https://doi.org/10.1002/jcb.22545.

(11) Prasad, V.; Mailankody, S. Research and Development Spending to Bring a Single Cancer Drug to Market and Revenues After Approval. *JAMA Intern. Med.* **2017**, *177* (11), 1569–1575. https://doi.org/10.1001/jamainternmed.2017.3601.

(12) Takebe, T.; Imai, R.; Ono, S. The Current Status of Drug Discovery and Development as Originated in United States Academia: The Influence of Industrial and Academic Collaboration on Drug Discovery and Development. *Clin. Transl. Sci.* **2018**, *11* (6), 597–606. https://doi.org/10.1111/cts.12577.

(13) Beachley, V. Z.; Wolf, M. T.; Sadtler, K.; Manda, S. S.; Jacobs, H.; Blatchley, M. R.; Bader, J. S.; Pandey, A.; Pardoll, D.; Elisseeff, J. H. Tissue Matrix Arrays for High-

Throughput Screening and Systems Analysis of Cell Function. *Nat. Methods* **2015**, *12* (12), 1197–1204. https://doi.org/10.1038/nmeth.3619.

(14) Kojima, T.; Moraes, C.; Cavnar, S. P.; Luker, G. D.; Takayama, S. Surface-Templated Hydrogel Patterns Prompt Matrix-Dependent Migration of Breast Cancer Cells towards Chemokine-Secreting Cells. *Acta Biomater.* **2015**, *13*, 68–77. https://doi.org/10.1016/j.actbio.2014.11.033.

(15) Jena, M. K.; Janjanam, J. Role of Extracellular Matrix in Breast Cancer Development: A Brief Update. *F1000Research* **2018**, *7*, 274–274. https://doi.org/10.12688/f1000research.14133.2.

(16) Muncie, J. M.; Weaver, V. M. Chapter One - The Physical and Biochemical Properties of the Extracellular Matrix Regulate Cell Fate. In *Current Topics in Developmental Biology*; Litscher, E. S., Wassarman, P. M., Eds.; Academic Press, 2018; Vol. 130, pp 1–37. https://doi.org/10.1016/bs.ctdb.2018.02.002.

(17) Lu, P.; Weaver, V. M.; Werb, Z. The Extracellular Matrix: A Dynamic Niche in Cancer Progression. *J. Cell Biol.* **2012**, *196* (4), 395–406. https://doi.org/10.1083/jcb.201102147.

(18) Theocharis, A. D.; Skandalis, S. S.; Gialeli, C.; Karamanos, N. K. Extracellular Matrix Structure. *Extracell. Matrix ECM ECM- Mater. Ther. Tools Targets Cancer Treat.* **2016**, *97*, 4–27. https://doi.org/10.1016/j.addr.2015.11.001.

(19) Baker, B. M.; Chen, C. S. Deconstructing the Third Dimension – How 3D Culture Microenvironments Alter Cellular Cues. *J. Cell Sci.* **2012**, *125*, 3015–3024. https://doi.org/10.1242/jcs.079509.

(20) Acerbi, I.; Cassereau, L.; Dean, I.; Shi, Q.; Au, A.; Park, C.; Chen, Y.; Liphardt, J.; Hwang, E.; Weaver, V. Human Breast Cancer Invasion and Aggression Correlates with ECM Stiffening and Immune Cell Infiltration. *Integr. Biol. Quant. Biosci. Nano Macro* **2015**, *7* (10), 1120–1134. https://doi.org/10.1039/c5ib00040h.

(21) Rockey, D. C.; Bell, P. D.; Hill, J. A. Fibrosis — A Common Pathway to Organ Injury and Failure. *N. Engl. J. Med.* **2015**, *372* (12), 1138–1149. https://doi.org/10.1056/NEJMra1300575.

(22) Peters, A. E.; Akhtar, R.; Comerford, E. J.; Bates, K. T. The Effect of Ageing and Osteoarthritis on the Mechanical Properties of Cartilage and Bone in the Human Knee Joint. *Sci. Rep.* **2018**, *8* (1), 5931. https://doi.org/10.1038/s41598-018-24258-6.

(23) Fong, E. L. S.; Harrington, D. A.; Farach-Carson, M. C.; Yu, H. Heralding a New Paradigm in 3D Tumor Modeling. *Biomaterials* **2016**, *108*, 197–213. https://doi.org/10.1016/j.biomaterials.2016.08.052.

(24) Fallica, B.; Maffei, J. S.; Villa, S.; Makin, G.; Zaman, M. Alteration of Cellular Behavior and Response to PI3K Pathway Inhibition by Culture in 3D Collagen Gels. *PLOS ONE* **2012**, *7* (10), e48024. https://doi.org/10.1371/journal.pone.0048024.

(25) Carvalho, M. R.; Lima, D.; Reis, R. L.; Oliveira, J. M.; Correlo, V. M. Anti-Cancer Drug Validation: The Contribution of Tissue Engineered Models. *Stem Cell Rev. Rep.* **2017**, 1–17. https://doi.org/10.1007/s12015-017-9720-x.

(26) Lovitt, C. J.; Shelper, T. B.; Avery, V. M. Miniaturized Three-Dimensional Cancer Model for Drug Evaluation. *ASSAY Drug Dev. Technol.* **2013**, *11* (7), 435–448. https://doi.org/10.1089/adt.2012.483.

(27) Lovitt, C. J.; Shelper, T. B.; Avery, V. M. Evaluation of Chemotherapeutics in a Three-Dimensional Breast Cancer Model. *J. Cancer Res. Clin. Oncol.* **2015**, *141* (5), 951–959. https://doi.org/10.1007/s00432-015-1950-1.

(28) Davidson, M. D.; Burdick, J. A.; Wells, R. G. Engineered Biomaterial Platforms to Study Fibrosis. *Adv. Healthc. Mater.* **2020**, *9* (8), 1901682. https://doi.org/10.1002/adhm.201901682.

(29) Tasdemir, N.; Bossart, E. A.; Li, Z.; Zhu, L.; Sikora, M. J.; Levine, K. M.; Jacobsen, B. M.; Tseng, G. C.; Davidson, N. E.; Oesterreich, S. Comprehensive Phenotypic Characterization of Human Invasive Lobular Carcinoma Cell Lines in 2D and 3D Cultures. *Cancer Res.* **2018**, *78* (21), 6209. https://doi.org/10.1158/0008-5472.CAN-18-1416.

(30) Miermont, A.; Lee, S. W. L.; Adriani, G.; Kamm, R. D. Quantitative Screening of the Effects of Hyper-Osmotic Stress on Cancer Cells Cultured in 2- or 3-Dimensional Settings. *Sci. Rep.* **2019**, *9* (1), 13782. https://doi.org/10.1038/s41598-019-50198-w.

(31) Edmondson, R.; Broglie, J. J.; Adcock, A. F.; Yang, L. Three-Dimensional Cell Culture Systems and Their Applications in Drug Discovery and Cell-Based Biosensors. *ASSAY Drug Dev. Technol.* **2014**, *12* (4), 207–218. https://doi.org/10.1089/adt.2014.573.

(32) Bischel, L. L.; Sung, K. E.; Jiménez-Torres, J. A.; Mader, B.; Keely, P. J.; Beebe, D. J. The Importance of Being a Lumen. *FASEB J.* **2014**, *28* (11), 4583–4590. https://doi.org/10.1096/fj.13-243733.

(33) Jiménez-Torres, J. A.; Peery, S. L.; Sung, K. E.; Beebe, D. J. LumeNEXT: A Practical Method to Pattern Luminal Structures in ECM Gels. *Adv. Healthc. Mater.* **2016**, *5* (2), 198–204. https://doi.org/10.1002/adhm.201500608.

(34) Baker, B. M.; Trappmann, B.; Stapleton, S. C.; Toro, E.; Chen, C. S. Microfluidics Embedded within Extracellular Matrix to Define Vascular Architectures and Pattern Diffusive Gradients. *Lab. Chip* **2013**, *13* (16), 3246–3252. https://doi.org/10.1039/c3lc50493j.

(35) Nelson, C. M.; VanDuijn, M. M.; Inman, J. L.; Fletcher, D. A.; Bissell, M. J. Tissue Geometry Determines Sites of Mammary Branching Morphogenesis in Organotypic Cultures. *Science* **2006**, *314* (5797), 298–300. https://doi.org/10.1126/science.1131000.

(36) Piotrowski-Daspit, A. S.; Nelson, C. M. Engineering Three-Dimensional Epithelial Tissues Embedded within Extracellular Matrix. **2016**, No. 113, e54283. https://doi.org/10.3791/54283.

(37) Pampaloni, F.; Stelzer, E.; Masotti, A. Three-Dimensional Tissue Models for Drug Discovery and Toxicology. *Recent Patents on Biotechnology* **2009**, *3* (2), 103–117. https://doi.org/10.2174/187220809788700201.

(38) Baker, B. M.; Chen, C. S. Deconstructing the Third Dimension – How 3D Culture Microenvironments Alter Cellular Cues. *J. Cell Sci.* **2012**, *125* (13), 3015. https://doi.org/10.1242/jcs.079509.

(39) Peck, Y.; Wang, D.-A. Three-Dimensionally Engineered Biomimetic Tissue Models for in Vitro Drug Evaluation: Delivery, Efficacy and Toxicity. *Expert Opin. Drug Deliv.* **2013**, *10* (3), 369–383. https://doi.org/10.1517/17425247.2013.751096.

(40) Kim, D.-H.; Lipke, E. A.; Kim, P.; Cheong, R.; Thompson, S.; Delannoy, M.; Suh, K.-Y.; Tung, L.; Levchenko, A. Nanoscale Cues Regulate the Structure and Function of Macroscopic Cardiac Tissue Constructs. *Proc. Natl. Acad. Sci.* **2010**, *107* (2), 565. https://doi.org/10.1073/pnas.0906504107.

(41) Brightman, A. O.; Rajwa, B. P.; Sturgis, J. E.; McCallister, M. E.; Robinson, J. P.; Voytik-Harbin, S. L. Time-Lapse Confocal Reflection Microscopy of Collagen Fibrillogenesis

and Extracellular Matrix Assembly in Vitro. *Biopolymers* **2000**, *54* (3), 222–234. https://doi.org/10.1002/1097-0282(200009)54:3<222::AID-BIP80>3.0.CO;2-K.

(42) Gillette, B. M.; Jensen, J. A.; Tang, B.; Yang, G. J.; Bazargan-Lari, A.; Zhong, M.; Sia, S. K. In Situ Collagen Assembly for Integrating Microfabricated Three-Dimensional Cell-Seeded Matrices. *Nat. Mater.* **2008**, *7* (8), 636–640. https://doi.org/10.1038/nmat2203.

(43) Wolf, K.; Alexander, S.; Schacht, V.; Coussens, L. M.; von Andrian, U. H.; van Rheenen, J.; Deryugina, E.; Friedl, P. Collagen-Based Cell Migration Models in Vitro and in Vivo. *Imaging Cell Dev. Biol.* **2009**, *20* (8), 931–941. https://doi.org/10.1016/j.semcdb.2009.08.005.

(44) Matera, D. L.; Wang, W. Y.; Smith, M. R.; Shikanov, A.; Baker, B. M. Fiber Density Modulates Cell Spreading in 3D Interstitial Matrix Mimetics. *ACS Biomater. Sci. Eng.* **2019**. https://doi.org/10.1021/acsbiomaterials.9b00141.

(45) Provenzano, P. P.; Inman, D. R.; Eliceiri, K. W.; Knittel, J. G.; Yan, L.; Rueden, C. T.; White, J. G.; Keely, P. J. Collagen Density Promotes Mammary Tumor Initiation and Progression. *BMC Med.* **2008**, *6*, 11–11. https://doi.org/10.1186/1741-7015-6-11.

(46) Han, W.; Chen, S.; Yuan, W.; Fan, Q.; Tian, J.; Wang, X.; Chen, L.; Zhang, X.; Wei, W.; Liu, R.; Qu, J.; Jiao, Y.; Austin, R. H.; Liu, L. Oriented Collagen Fibers Direct Tumor Cell Intravasation. *Proc. Natl. Acad. Sci.* **2016**, *113* (40), 11208. https://doi.org/10.1073/pnas.1610347113.

(47) Dickinson, R. B.; Guido, S.; Tranquillo, R. T. Biased Cell Migration of Fibroblasts Exhibiting Contact Guidance in Oriented Collagen Gels. *Annals of biomedical engineering* **1994**, *22* (4), 342–356. https://doi-org.proxy3.library.mcgill.ca/10.1007/BF02368241.

(48) Yang, Y.; Motte, S.; Kaufman, L. J. Pore Size Variable Type I Collagen Gels and Their Interaction with Glioma Cells. *Biomaterials* **2010**, *31* (21), 5678–5688. https://doi.org/10.1016/j.biomaterials.2010.03.039.

(49) Velez, D. O.; Ranamukhaarachchi, S. K.; Kumar, A.; Modi, R. N.; Lim, E. W.; Engler, A. J.; Metallo, C. M.; Fraley, S. I. 3D Collagen Architecture Regulates Cell Adhesion through Degradability, Thereby Controlling Metabolic and Oxidative Stress. *Integr. Biol.* **2019**, *11* (5), 221–234. https://doi.org/10.1093/intbio/zyz019.

(50) Velez, D. O.; Tsui, B.; Goshia, T.; Chute, C. L.; Han, A.; Carter, H.; Fraley, S. I. 3D Collagen Architecture Induces a Conserved Migratory and Transcriptional Response Linked to Vasculogenic Mimicry. *Nat. Commun.* **2017**, *8* (1), 1651. https://doi.org/10.1038/s41467-017-01556-7.

(51) Ranamukhaarachchi, S. K.; Modi, R. N.; Han, A.; Velez, D. O.; Kumar, A.; Engler, A. J.; Fraley, S. I. Macromolecular Crowding Tunes 3D Collagen Architecture and Cell Morphogenesis. *Biomater. Sci.* **2019**, *7* (2), 618–633. https://doi.org/10.1039/C8BM01188E.

(52) Berger, A. J.; Linsmeier, K. M.; Kreeger, P. K.; Masters, K. S. Decoupling the Effects of Stiffness and Fiber Density on Cellular Behaviors via an Interpenetrating Network of Gelatin-Methacrylate and Collagen. *Biomaterials* **2017**, *141*, 125–135. https://doi.org/10.1016/j.biomaterials.2017.06.039.

(53) Baker, B. M.; Trappmann, B.; Wang, W. Y.; Sakar, M. S.; Kim, I. L.; Shenoy, V. B.; Burdick, J. A.; Chen, C. S. Cell-Mediated Fibre Recruitment Drives Extracellular Matrix Mechanosensing in Engineered Fibrillar Microenvironments. *Nat. Mater.* **2015**, *14* (12), 1262–1268. https://doi.org/10.1038/nmat4444.

(54) Rose, J. C.; Gehlen, D. B.; Haraszti, T.; Köhler, J.; Licht, C. J.; De Laporte, L. Biofunctionalized Aligned Microgels Provide 3D Cell Guidance to Mimic Complex Tissue Matrices. *Biomaterials* **2018**, *163*, 128–141. https://doi.org/10.1016/j.biomaterials.2018.02.001.

(55) Nerger, B. A.; Brun, P. T.; Nelson, C. M. Marangoni Flows Drive the Alignment of Fibrillar Cell-Laden Hydrogels. *Science advances* **2020**, *6* (24), eaaz7748. https://doi-org.proxy3.library.mcgill.ca/10.1126/sciadv.aaz7748.

(56) Zeng, Y.-N.; Kang, Y.-L.; Rau, L.-R.; Hsu, F.-Y.; Tsai, S.-W. Construction of Cell-Containing, Anisotropic, Three-Dimensional Collagen Fibril Scaffolds Using External Vibration and Their Influence on Smooth Muscle Cell Phenotype Modulation. *Biomed. Mater.* **2017**, *12* (4), 045019. https://doi.org/10.1088/1748-605x/aa766d.

(57) Unadkat, H. V.; Hulsman, M.; Cornelissen, K.; Papenburg, B. J.; Truckenmüller, R. K.; Carpenter, A. E.; Wessling, M.; Post, G. F.; Uetz, M.; Reinders, M. J. T.; Stamatialis, D.; van Blitterswijk, C. A.; de Boer, J. An Algorithm-Based Topographical Biomaterials Library to Instruct Cell Fate. *Proc. Natl. Acad. Sci.* **2011**, *108* (40), 16565. https://doi.org/10.1073/pnas.1109861108.

(58) Ray, A.; Lee, O.; Win, Z.; Edwards, R. M.; Alford, P. W.; Kim, D.-H.; Provenzano, P. P. Anisotropic Forces from Spatially Constrained Focal Adhesions Mediate Contact Guidance Directed Cell Migration. *Nat. Commun.* **2017**, *8* (1), 14923. https://doi.org/10.1038/ncomms14923.

(59) Kim SJ; Tatman PD; Song DH; Gee AO; Kim DH; Kim SJ. Nanotopographic Cues and Stiffness Control of Tendon-Derived Stem Cells from Diverse Conditions. *Int J Nanomedicine* **2018**, *13*, 7217–7227. https://doi.org/10.2147/IJN.S181743.

(60) Doyle, A. D.; Wang, F. W.; Matsumoto, K.; Yamada, K. M. One-Dimensional Topography Underlies Three-Dimensional Fibrillar Cell Migration. *J. Cell Biol.* **2009**, *184* (4), 481–490. https://doi.org/10.1083/jcb.200810041.

(61) Dixon, A. R.; Moraes, C.; Csete, M. E.; Thouless, M. D.; Philbert, M. A.; Takayama, S. One-Dimensional Patterning of Cells in Silicone Wells via Compression-Induced Fracture. *J. Biomed. Mater. Res. A* **2014**, *102* (5), 1361–1369. https://doi.org/10.1002/jbm.a.34814.

(62) Zhu, X.; Mills, K. L.; Peters, P. R.; Bahng, J. H.; Liu, E. H.; Shim, J.; Naruse, K.; Csete, M. E.; Thouless, M. D.; Takayama, S. Fabrication of Reconfigurable Protein Matrices by Cracking. *Nature materials* **2005**, *4* (5), 403–406. https://doi.org/10.1038/nmat1365.

(63) Wang, W. Y.; Pearson, A. T.; Kutys, M. L.; Choi, C. K.; Wozniak, M. A.; Baker, B. M.; Chen, C. S. Extracellular Matrix Alignment Dictates the Organization of Focal Adhesions and Directs Uniaxial Cell Migration. *APL Bioeng.* **2018**, *2* (4), 046107. https://doi.org/10.1063/1.5052239.

(64) Changede, R.; Cai, H.; Wind, S. J.; Sheetz, M. P. Integrin Nanoclusters Can Bridge Thin Matrix Fibres to Form Cell–Matrix Adhesions. *Nat. Mater.* **2019**, *18* (12), 1366–1375. https://doi.org/10.1038/s41563-019-0460-y.

(65) Xue, N.; Li, X.; Bertulli, C.; Li, Z.; Patharagulpong, A.; Sadok, A.; Huang, Y. Y. S. Rapid Patterning of 1-D Collagenous Topography as an ECM Protein Fibril Platform for Image Cytometry. *PLOS ONE* **2014**, *9* (4), e93590. https://doi.org/10.1371/journal.pone.0093590.

(66) Moraes, C.; Kim, B. C.; Zhu, X.; Mills, K. L.; Dixon, A. R.; Thouless, M. D.; Takayama, S. Defined Topologically-Complex Protein Matrices to Manipulate Cell Shape via Three-

Dimensional Fiber-like Patterns. *Lab. Chip* **2014**, *14* (13), 2191–2201. https://doi.org/10.1039/C4LC00122B.

(67) Chen, C. S.; Mrksich, M.; Huang, S.; Whitesides, G. M.; Ingber, D. E. Geometric Control of Cell Life and Death. *Science* **1997**, *276* (5317), 1425. https://doi.org/10.1126/science.276.5317.1425.

(68) Bellas, E.; Chen, C. S. Forms, Forces, and Stem Cell Fate. *Cell Cycle Differ. Dis.* **2014**, *31*, 92–97. https://doi.org/10.1016/j.ceb.2014.09.006.

(69) Luxenburg, C.; Zaidel-Bar, R. From Cell Shape to Cell Fate via the Cytoskeleton — Insights from the Epidermis. *Exp. Cell Res.* **2019**, *378* (2), 232–237. https://doi.org/10.1016/j.yexcr.2019.03.016.

(70) Weaver, V. M.; Lelièvre, S.; Lakins, J. N.; Chrenek, M. A.; Jones, J. C.; Giancotti, F.; Werb, Z.; Bissell, M. J. Β4 Integrin-Dependent Formation of Polarized Three-Dimensional Architecture Confers Resistance to Apoptosis in Normal and Malignant Mammary Epithelium. *Cancer Cell* **2002**, *2* (3), 205–216.

(71) Rubashkin, M.; Cassereau, L.; Bainer, R.; DuFort, C.; Yui, Y.; Ou, G.; Paszek, M.; Davidson, M.; Chen, Y.; Weaver, V. Force Engages Vinculin and Promotes Tumor Progression by Enhancing PI3-Kinase Activation of Phosphatidylinositol (3,4,5)-Triphosphate. *Cancer Res.* **2014**, *74* (17), 4597–4611. https://doi.org/10.1158/0008-5472.CAN-13-3698.

(72) Lee, J.; Abdeen, A. A.; Zhang, D.; Kilian, K. A. Directing Stem Cell Fate on Hydrogel Substrates by Controlling Cell Geometry, Matrix Mechanics and Adhesion Ligand Composition. *Biomaterials* **2013**, *34* (33), 8140–8148. https://doi.org/10.1016/j.biomaterials.2013.07.074.

(73) Lee, J.; Abdeen, A. A.; Wycislo, K. L.; Fan, T. M.; Kilian, K. A. Interfacial Geometry Dictates Cancer Cell Tumorigenicity. *Nat. Mater.* **2016**, *15* (8), 856–862. https://doi.org/10.1038/nmat4610.

(74) Schutgens, F.; Clevers, H. Human Organoids: Tools for Understanding Biology and Treating Diseases. *Annu. Rev. Pathol. Mech. Dis.* **2020**, *15* (1), 211–234. https://doi.org/10.1146/annurev-pathmechdis-012419-032611.

(75) Haider, S.; Meinhardt, G.; Saleh, L.; Kunihs, V.; Gamperl, M.; Kaindl, U.; Ellinger, A.; Burkard, T. R.; Fiala, C.; Pollheimer, J.; Mendjan, S.; Latos, P. A.; Knöfler, M. Self-Renewing Trophoblast Organoids Recapitulate the Developmental Program of the Early Human Placenta. *Stem Cell Rep.* **2018**, *11* (2), 537–551. https://doi.org/10.1016/j.stemcr.2018.07.004.

(76) Wang, Z.; Lang, B.; Qu, Y.; Li, L.; Song, Z.; Wang, Z. Single-Cell Patterning Technology for Biological Applications. *Biomicrofluidics* **2019**, *13* (6), 061502. https://doi.org/doi:10.1063/1.5123518.

(77) Jing, P.; Wu, J.; Liu, G. W.; Keeler, E. G.; Pun, S. H.; Lin, L. Y. Photonic Crystal Optical Tweezers with High Efficiency for Live Biological Samples and Viability Characterization. *Sci. Rep.* **2016**, *6* (1), 19924. https://doi.org/10.1038/srep19924.

(78) Jing, P.; Liu, Y.; Keeler, E. G.; Cruz, N. M.; Freedman, B. S.; Lin, L. Y. Optical Tweezers System for Live Stem Cell Organization at the Single-Cell Level. *Biomedical optics express* **2018**, *9* (2), 771–779. https://doi.org/10.1364/BOE.9.000771.

(79) Tung, Y.-C.; Hsiao, A. Y.; Allen, S. G.; Torisawa, Y.; Ho, M.; Takayama, S. High-Throughput 3D Spheroid Culture and Drug Testing Using a 384 Hanging Drop Array. *Analyst* **2011**, *136* (3), 473–478. https://doi.org/10.1039/C0AN00609B.

(80) Han, C.; Takayama, S.; Park, J. Formation and Manipulation of Cell Spheroids Using a Density Adjusted PEG/DEX Aqueous Two Phase System. *Sci. Rep.* **2015**, *5* (1), 11891. https://doi.org/10.1038/srep11891.

(81) Zhao, L.; Mok, S.; Moraes, C. Micropocket Hydrogel Devices for All-in-One Formation, Assembly, and Analysis of Aggregate-Based Tissues. *Biofabrication* **2019**, *11* (4), 045013. https://doi.org/10.1088/1758-5090/ab30b4.

(82) Horman, S. R.; To, J.; Orth, A. P. An HTS-Compatible 3D Colony Formation Assay to Identify Tumor-Specific Chemotherapeutics. *J. Biomol. Screen.* **2013**, *18* (10), 1298–1308. https://doi.org/10.1177/1087057113499405.

(83) Ekert, J. E.; Johnson, K.; Strake, B.; Pardinas, J.; Jarantow, S.; Perkinson, R.; Colter, D. C. Three-Dimensional Lung Tumor Microenvironment Modulates Therapeutic Compound Responsiveness In Vitro – Implication for Drug Development. *PLOS ONE* **2014**, *9* (3), e92248. https://doi.org/10.1371/journal.pone.0092248.

(84) Brandenberg, N.; Hoehnel, S.; Kuttler, F.; Homicsko, K.; Ceroni, C.; Ringel, T.; Gjorevski, N.; Schwank, G.; Coukos, G.; Turcatti, G.; Lutolf, M. P. High-Throughput Automated Organoid Culture via Stem-Cell Aggregation in Microcavity Arrays. *Nat Biomed Eng.* **2020**, 10.1038/s41551-020-0565–2. https://doi.org/doi:10.1038/s41551-020-0565-2.

(85) Bischel, L. L.; Beebe, D. J.; Sung, K. E. Microfluidic Model of Ductal Carcinoma in Situ with 3D, Organotypic Structure. *BMC Cancer* **2015**, *15*, 12. https://doi.org/10.1186/s12885-015-1007-5.

(86) Bischel, L. L.; Lee, S.-H.; Beebe, D. J. A Practical Method for Patterning Lumens through ECM Hydrogels via Viscous Finger Patterning. *J. Lab. Autom.* **2012**, *17* (2), 96–103. https://doi.org/10.1177/2211068211426694.

(87) Xie, R.; Korolj, A.; Liu, C.; Song, X.; Lu, R. X. Z.; Zhang, B.; Ramachandran, A.; Liang, Q.; Radisic, M. H-FIBER: Microfluidic Topographical Hollow Fiber for Studies of Glomerular Filtration Barrier. *ACS Cent. Sci.* **2020**, *6* (6), 903–912. https://doi.org/10.1021/acscentsci.9b01097.

(88) Ayad, N. M. E.; Kaushik, S.; Weaver, V. M. Tissue Mechanics, an Important Regulator of Development and Disease. *Philos. Trans. R. Soc. B Biol. Sci.* **2019**, *374* (1779), 20180215. https://doi.org/10.1098/rstb.2018.0215.

(89) Guimarães, C. F.; Gasperini, L.; Marques, A. P.; Reis, R. L. The Stiffness of Living Tissues and Its Implications for Tissue Engineering. *Nat. Rev. Mater.* **2020**, *5* (5), 351–370. https://doi.org/10.1038/s41578-019-0169-1.

(90) Anlaş, A. A.; Nelson, C. M. Tissue Mechanics Regulates Form, Function, and Dysfunction. *Cell Dyn.* **2018**, *54*, 98–105. https://doi.org/10.1016/j.ceb.2018.05.012.

(91) Chang, T. T.; Thakar, D.; Weaver, V. M. Force-Dependent Breaching of the Basement Membrane. *Basement Membr. Health Dis.* **2017**, *57–58*, 178–189. https://doi.org/10.1016/j.matbio.2016.12.005.

(92) Engler, A.; Bacakova, L.; Newman, C.; Hategan, A.; Griffin, M.; Discher, D. Substrate Compliance versus Ligand Density in Cell on Gel Responses. *Biophys. J.* **2004**, *86* (1), 617–628. https://doi.org/10.1016/S0006-3495(04)74140-5.

(93) Engler, A. J.; Sen, S.; Sweeney, H. L.; Discher, D. E. Matrix Elasticity Directs Stem Cell Lineage Specification. *Cell* **2006**, *126* (4), 677–689. https://doi.org/10.1016/j.cell.2006.06.044.

(94) Chaudhuri, O. Viscoelastic Hydrogels for 3D Cell Culture. *Biomater. Sci.* **2017**, *5* (8), 1480–1490. https://doi.org/10.1039/C7BM00261K.

(95) Huang, D.; Huang, Y.; Xiao, Y.; Yang, X.; Lin, H.; Feng, G.; Zhu, X.; Zhang, X. Viscoelasticity in Natural Tissues and Engineered Scaffolds for Tissue Reconstruction. *Acta Biomater.* **2019**, *97*, 74–92. https://doi.org/10.1016/j.actbio.2019.08.013.

(96) Mueller, S.; Sandrin, L. Liver Stiffness: A Novel Parameter for the Diagnosis of Liver Disease. *Hepatic Med. Evid. Res.* **2010**, *2*, 49–67. https://doi.org/10.2147/hmer.s7394.

(97) Reiter, R.; Freise, C.; Jöhrens, K.; Kamphues, C.; Seehofer, D.; Stockmann, M.; Somasundaram, R.; Asbach, P.; Braun, J.; Samani, A.; Sack, I. Wideband MRE and Static Mechanical Indentation of Human Liver Specimen: Sensitivity of Viscoelastic Constants to the Alteration of Tissue Structure in Hepatic Fibrosis. *J. Biomech.* **2014**, *47* (7), 1665–1674. https://doi.org/10.1016/j.jbiomech.2014.02.034.

(98) Feldmann, A.; Langlois, C.; Dewailly, M.; Martinez, E. F.; Boulanger, L.; Kerdraon, O.; Faye, N. Shear Wave Elastography (SWE): An Analysis of Breast Lesion Characterization in 83 Breast Lesions. *Ultrasound Med. Biol.* **2015**, *41* (10), 2594–2604. https://doi.org/10.1016/j.ultrasmedbio.2015.05.019.

(99) Dobruch-Sobczak, K.; Nowicki, A. Role of Shear Wave Sonoelastography in Differentiation Between Focal Breast Lesions. *Ultrasound Med. Biol.* **2015**, *41* (2), 366–374. https://doi.org/10.1016/j.ultrasmedbio.2014.08.024.

(100) Denisin, A. K.; Pruitt, B. L. Tuning the Range of Polyacrylamide Gel Stiffness for Mechanobiology Applications. *ACS Appl. Mater. Interfaces* **2016**, *8* (34), 21893–21902. https://doi.org/10.1021/acsami.5b09344.

(101) Nghe, P.; Boulineau, S.; Gude, S.; Recouvreux, P.; van Zon, J. S.; Tans, S. J. Microfabricated Polyacrylamide Devices for the Controlled Culture of Growing Cells and Developing Organisms. *PLOS ONE* **2013**, *8* (9), e75537. https://doi.org/10.1371/journal.pone.0075537.

(102) Chandrasekaran, A.; Kouthouridis, S.; Lee, W.; Lin, N.; Ma, Z.; Turner, M. J.; Hanrahan, J. W.; Moraes, C. Magnetic Microboats for Floating, Stiffness Tunable, Air–Liquid Interface Epithelial Cultures. *Lab. Chip* **2019**, *19* (17), 2786–2798. https://doi.org/10.1039/C9LC00267G.

(103) Beningo, K. A.; Dembo, M.; Wang, Y. Responses of Fibroblasts to Anchorage of Dorsal Extracellular Matrix Receptors. *Proc. Natl. Acad. Sci.* **2004**, *101* (52), 18024. https://doi.org/10.1073/pnas.0405747102.

(104) Ballester-Beltrán, J.; Lebourg, M.; Rico, P.; Salmerón-Sánchez, M. Dorsal and Ventral Stimuli in Cell–Material Interactions: Effect on Cell Morphology. *Biointerphases* **2012**, *7* (1), 39. https://doi.org/10.1007/s13758-012-0039-5.

(105) Fischer, R. S.; Myers, K. A.; Gardel, M. L.; Waterman, C. M. Stiffness-Controlled Three-Dimensional Extracellular Matrices for High-Resolution Imaging of Cell Behavior. *Nat. Protoc.* **2012**, *7* (11), 2056–2066. https://doi.org/10.1038/nprot.2012.127.

(106) Ehrbar, M.; Sala, A.; Lienemann, P.; Ranga, A.; Mosiewicz, K.; Bittermann, A.; Rizzi, S. C.; Weber, F. E.; Lutolf, M. P. Elucidating the Role of Matrix Stiffness in 3D Cell Migration and Remodeling. *Biophys. J.* **2011**, *100* (2), 284–293. https://doi.org/10.1016/j.bpj.2010.11.082.

(107) Bott, K.; Upton, Z.; Schrobback, K.; Ehrbar, M.; Hubbell, J. A.; Lutolf, M. P.; Rizzi, S. C. The Effect of Matrix Characteristics on Fibroblast Proliferation in 3D Gels. *Biomaterials* **2010**, *31* (32), 8454–8464. https://doi.org/10.1016/j.biomaterials.2010.07.046.

(108) Rosales, A. M.; Rodell, C. B.; Chen, M. H.; Morrow, M. G.; Anseth, K. S.; Burdick, J. A. Reversible Control of Network Properties in Azobenzene-Containing Hyaluronic Acid-Based Hydrogels. *Bioconjug. Chem.* **2018**, *29* (4), 905–913. https://doi.org/10.1021/acs.bioconjchem.7b00802.

(109) Chiu, Y.-C.; Cheng, M.-H.; Engel, H.; Kao, S.-W.; Larson, J. C.; Gupta, S.; Brey, E. M. The Role of Pore Size on Vascularization and Tissue Remodeling in PEG Hydrogels. *Biomaterials* **2011**, *32* (26), 6045–6051. https://doi.org/10.1016/j.biomaterials.2011.04.066.

(110) Gill, B. J.; Gibbons, D. L.; Roudsari, L. C.; Saik, J. E.; Rizvi, Z. H.; Roybal, J. D.; Kurie, J. M.; West, J. L. A Synthetic Matrix with Independently Tunable Biochemistry and Mechanical Properties to Study Epithelial Morphogenesis and EMT in a Lung Adenocarcinoma Model. *Cancer Res.* **2012**, *72* (22), 6013. https://doi.org/10.1158/0008-5472.CAN-12-0895.

(111) Babaie, E.; Bhaduri, S. B. Fabrication Aspects of Porous Biomaterials in Orthopedic Applications: A Review. *ACS Biomater. Sci. Eng.* **2018**, *4* (1), 1–39. https://doi.org/10.1021/acsbiomaterials.7b00615.

(112) Xiao, S.; Zhao, T.; Wang, J.; Wang, C.; Du, J.; Ying, L.; Lin, J.; Zhang, C.; Hu, W.; Wang, L.; Xu, K. Gelatin Methacrylate (GelMA)-Based Hydrogels for Cell Transplantation: An Effective Strategy for Tissue Engineering. *Stem Cell Rev. Rep.* **2019**, *15* (5), 664–679. https://doi.org/10.1007/s12015-019-09893-4.

(113) Nichol, J. W.; Koshy, S. T.; Bae, H.; Hwang, C. M.; Yamanlar, S.; Khademhosseini, A. Cell-Laden Microengineered Gelatin Methacrylate Hydrogels. *Biomaterials* **2010**, *31* (21), 5536–5544. https://doi.org/10.1016/j.biomaterials.2010.03.064.

(114) Lin, C.-H.; Su, J. J.-M.; Lee, S.-Y.; Lin, Y.-M. Stiffness Modification of Photopolymerizable Gelatin-Methacrylate Hydrogels Influences Endothelial Differentiation of Human Mesenchymal Stem Cells. *J. Tissue Eng. Regen. Med.* **2018**, *12* (10), 2099–2111. https://doi.org/10.1002/term.2745.

(115) Shen, Y.-I.; Abaci, H. E.; Krupski, Y.; Weng, L.-C.; Burdick, J. A.; Gerecht, S. Hyaluronic Acid Hydrogel Stiffness and Oxygen Tension Affect Cancer Cell Fate and Endothelial Sprouting. *Biomater. Sci.* **2014**, *2* (5), 655–665. https://doi.org/10.1039/C3BM60274E.

(116) Suo, A.; Xu, W.; Wang, Y.; Sun, T.; Ji, L.; Qian, J. Dual-Degradable and Injectable Hyaluronic Acid Hydrogel Mimicking Extracellular Matrix for 3D Culture of Breast Cancer MCF-7 Cells. *Carbohydr. Polym.* **2019**, *211*, 336–348. https://doi.org/10.1016/j.carbpol.2019.01.115.

(117) Gwon, K.; Kim, E.; Tae, G. Heparin-Hyaluronic Acid Hydrogel in Support of Cellular Activities of 3D Encapsulated Adipose Derived Stem Cells. *Acta Biomater.* **2017**, *49*, 284–295. https://doi.org/10.1016/j.actbio.2016.12.001.

(118) Chaudhuri, O.; Koshy, S. T.; Branco da Cunha, C.; Shin, J.-W.; Verbeke, C. S.; Allison, K. H.; Mooney, D. J. Extracellular Matrix Stiffness and Composition Jointly Regulate the Induction of Malignant Phenotypes in Mammary Epithelium. *Nat Mater* **2014**, *13* (10), 970–978.

(119) Reynolds, D. S.; Bougher, K. M.; Letendre, J. H.; Fitzgerald, S. F.; Gisladottir, U. O.; Grinstaff, M. W.; Zaman, M. H. Mechanical Confinement via a PEG/Collagen Interpenetrating Network Inhibits Behavior Characteristic of Malignant Cells in the

Triple Negative Breast Cancer Cell Line MDA.MB.231. *Acta Biomater.* **2018**, *77*, 85–95. https://doi.org/10.1016/j.actbio.2018.07.032.

(120) Cao, H.; Lee, M. K. H.; Yang, H.; Sze, S. K.; Tan, N. S.; Tay, C. Y. Mechanoregulation of Cancer-Associated Fibroblast Phenotype in Three-Dimensional Interpenetrating Hydrogel Networks. *Langmuir* **2018**. https://doi.org/10.1021/acs.langmuir.8b02649.

(121) Ledo, A. M.; Vining, K. H.; Alonso, M. J.; Garcia-Fuentes, M.; Mooney, D. J. Extracellular Matrix Mechanics Regulate Transfection and SOX9-Directed Differentiation of Mesenchymal Stem Cells. *Acta Biomater.* **2020**, *110*, 153–163. https://doi.org/10.1016/j.actbio.2020.04.027.

(122) Ulrich, T. A.; Jain, A.; Tanner, K.; MacKay, J. L.; Kumar, S. Probing Cellular Mechanobiology in Three-Dimensional Culture with Collagen–Agarose Matrices. *Biomaterials* **2010**, *31* (7), 1875–1884. https://doi.org/10.1016/j.biomaterials.2009.10.047.

(123) Paszek, M. J.; Zahir, N.; Johnson, K. R.; Lakins, J. N.; Rozenberg, G. I.; Gefen, A.; Reinhart-King, C. A.; Margulies, S. S.; Dembo, M.; Boettiger, D.; Hammer, D. A.; Weaver, V. M. Tensional Homeostasis and the Malignant Phenotype. *Cancer Cell* **2005**, *8* (3), 241–254. https://doi.org/10.1016/j.ccr.2005.08.010.

(124) Levental, K. R.; Yu, H.; Kass, L.; Lakins, J. N.; Egeblad, M.; Erler, J. T.; Fong, S. F.; Csiszar, K.; Giaccia, A.; Weninger, W.; Yamauchi, M.; Gasser, D. L.; Weaver, V. M. Matrix Crosslinking Forces Tumor Progression by Enhancing Integrin Signaling. *Cell* **2009**, *139* (5), 891–906. https://doi.org/10.1016/j.cell.2009.10.027.

(125) Islam, A.; Cotey, S.; Younesi, M.; Akkus, O. *Tuning of Stiffness Anisotropy in Collagen Sheets by Planar Stretch*; 2014.

(126) Lee, K. Y.; Mooney, D. J. Hydrogels for Tissue Engineering. *Chem. Rev.* **2001**, *101* (7), 1869–1880. https://doi.org/10.1021/cr000108x.

(127) Trappmann, B.; Gautrot, J. E.; Connelly, J. T.; Strange, D. G. T.; Li, Y.; Oyen, M. L.; Cohen Stuart, M. A.; Boehm, H.; Li, B.; Vogel, V.; Spatz, J. P.; Watt, F. M.; Huck, W. T. S. Extracellular-Matrix Tethering Regulates Stem-Cell Fate. *Nat. Mater.* **2012**, *11* (7), 642–649. https://doi.org/10.1038/nmat3339.

(128) Wen, J. H.; Vincent, L. G.; Fuhrmann, A.; Choi, Y. S.; Hribar, K. C.; Taylor-Weiner, H.; Chen, S.; Engler, A. J. Interplay of Matrix Stiffness and Protein Tethering in Stem Cell Differentiation. *Nat. Mater.* **2014**, *13* (10), 979–987. https://doi.org/10.1038/nmat4051.

(129) Fu, J.; Wang, Y.-K.; Yang, M. T.; Desai, R. A.; Yu, X.; Liu, Z.; Chen, C. S. Mechanical Regulation of Cell Function with Geometrically Modulated Elastomeric Substrates. *Nat. Methods* **2010**, *7* (9), 733–736. https://doi.org/10.1038/nmeth.1487.

(130) Breckenridge, M. T.; Desai, R. A.; Yang, M. T.; Fu, J.; Chen, C. S. Substrates with Engineered Step Changes in Rigidity Induce Traction Force Polarity and Durotaxis. *Cell. Mol. Bioeng.* **2014**, *7* (1), 26–34. https://doi.org/10.1007/s12195-013-0307-6.

(131) Davidson, C. D.; Jayco, D. K. P.; Matera, D. L.; DePalma, S. J.; Hiraki, H. L.; Wang, W. Y.; Baker, B. M. Myofibroblast Activation in Synthetic Fibrous Matrices Composed of Dextran Vinyl Sulfone. *Acta Biomater.* **2020**, *105*, 78–86. https://doi.org/10.1016/j.actbio.2020.01.009.

(132) Mabry, K. M.; Lawrence, R. L.; Anseth, K. S. Dynamic Stiffening of Poly(Ethylene Glycol)-Based Hydrogels to Direct Valvular Interstitial Cell Phenotype in a Three-Dimensional Environment. *Biomaterials* **2015**, *49*, 47–56. https://doi.org/10.1016/j.biomaterials.2015.01.047.

(133) Taubenberger, A. V.; Girardo, S.; Träber, N.; Fischer-Friedrich, E.; Kräter, M.; Wagner, K.; Kurth, T.; Richter, I.; Haller, B.; Binner, M.; Hahn, D.; Freudenberg, U.; Werner, C.; Guck, J. 3D Microenvironment Stiffness Regulates Tumor Spheroid Growth and Mechanics via P21 and ROCK. *bioRxiv* **2019**, 586784. https://doi.org/10.1101/586784.

(134) Kostic, A.; Lynch, C. D.; Sheetz, M. P. Differential Matrix Rigidity Response in Breast Cancer Cell Lines Correlates with the Tissue Tropism. *PLOS ONE* **2009**, *4* (7), e6361. https://doi.org/10.1371/journal.pone.0006361.

(135) Tilghman, R. W.; Cowan, C. R.; Mih, J. D.; Koryakina, Y.; Gioeli, D.; Slack-Davis, J. K.; Blackman, B. R.; Tschumperlin, D. J.; Parsons, J. T. Matrix Rigidity Regulates Cancer Cell Growth and Cellular Phenotype. *PLOS ONE* **2010**, *5* (9), e12905. https://doi.org/10.1371/journal.pone.0012905.

(136) Tassieri, M.; Giudice, F. D.; Robertson, E. J.; Jain, N.; Fries, B.; Wilson, R.; Glidle, A.; Greco, F.; Netti, P. A.; Maffettone, P. L.; Bicanic, T.; Cooper, J. M. Microrheology with Optical Tweezers: Measuring the Relative Viscosity of Solutions 'at a Glance.' *Sci. Rep.* **2015**, *5* (1), 8831. https://doi.org/10.1038/srep08831.

(137) Braunsmann, C.; Seifert, J.; Rheinlaender, J.; Schäffer, T. E. High-Speed Force Mapping on Living Cells with a Small Cantilever Atomic Force Microscope. *Rev. Sci. Instrum.* **2014**, *85* (7), 073703. https://doi.org/10.1063/1.4885464.

(138) Deptuła, P.; Łysik, D.; Pogoda, K.; Cieśluk, M.; Namiot, A.; Mystkowska, J.; Król, G.; Głuszek, S.; Janmey, P. A.; Bucki, R. Tissue Rheology as a Possible Complementary Procedure to Advance Histological Diagnosis of Colon Cancer. *ACS Biomater. Sci. Eng.* **2020**, *6* (10), 5620–5631. https://doi.org/10.1021/acsbiomaterials.0c00975.

(139) Insana, M. F.; Pellot-Barakat, C.; Sridhar, M.; Lindfors, K. K. Viscoelastic Imaging of Breast Tumor Microenvironment With Ultrasound. *J. Mammary Gland Biol. Neoplasia* **2004**, *9* (4), 393–404. https://doi.org/10.1007/s10911-004-1409-5.

(140) Sinkus, R.; Siegmann, K.; Xydeas, T.; Tanter, M.; Claussen, C.; Fink, M. MR Elastography of Breast Lesions: Understanding the Solid/Liquid Duality Can Improve the Specificity of Contrast-Enhanced MR Mammography. *Magn. Reson. Med.* **2007**, *58* (6), 1135–1144. https://doi.org/10.1002/mrm.21404.

(141) González-Bermúdez, B.; Guinea, G. V.; Plaza, G. R. Advances in Micropipette Aspiration: Applications in Cell Biomechanics, Models, and Extended Studies. *Biophys. J.* **2019**, *116* (4), 587–594. https://doi.org/10.1016/j.bpj.2019.01.004.

(142) Puig-De-Morales, M.; Grabulosa, M.; Alcaraz, J.; Mullol, J.; Maksym, G. N.; Fredberg, J. J.; Navajas, D. Measurement of Cell Microrheology by Magnetic Twisting Cytometry with Frequency Domain Demodulation. *J. Appl. Physiol.* **2001**, *91* (3), 1152–1159. https://doi.org/10.1152/jappl.2001.91.3.1152.

(143) Serwane, F.; Mongera, A.; Rowghanian, P.; Kealhofer, D. A.; Lucio, A. A.; Hockenbery, Z. M.; Campàs, O. In Vivo Quantification of Spatially Varying Mechanical Properties in Developing Tissues. *Nat. Methods* **2017**, *14* (2), 181–186. https://doi.org/10.1038/nmeth.4101.

(144) Mok, S.; Al Habyan, S.; Ledoux, C.; Lee, W.; MacDonald, K. N.; McCaffrey, L.; Moraes, C. Mapping Cellular-Scale Internal Mechanics in 3D Tissues with Thermally Responsive Hydrogel Probes. *Nat. Commun.* **2020**, *11* (1), 4757. https://doi.org/10.1038/s41467-020-18469-7.

(145) Nakamura. Changes in Viscoelastic Properties of Articular Cartilage in Early Stage of Osteoarthritis, as Determined by Optical Coherence Tomography-Based Strain Rate Tomography. **2019**.

(146) Fortis, A.; Kostopoulos, V.; Panagiotopoulos, E.; Tsantzalis, S.; Kokkinos, A. Viscoelastic Properties of Cartilage-Subchondral Bone Complex in Osteoarthritis. *J. Med. Eng. Technol.* **2004**, *28* (5), 223–226. https://doi.org/10.1080/03091900410001676003.

(147) Wong, B.; Bae, W.; Gratz, K.; Sah, R. Shear Deformation Kinematics during Cartilage Articulation: Effect of Lubrication, Degeneration, and Stress Relaxation. *Mol Cell Biomech* **2008**, *5* (3), 197-206.

(148) Perepelyuk, M.; Chin, L.; Cao, X.; van Oosten, A.; Shenoy, V. B.; Janmey, P. A.; Wells, R. G. Normal and Fibrotic Rat Livers Demonstrate Shear Strain Softening and Compression Stiffening: A Model for Soft Tissue Mechanics. *PLOS ONE* **2016**, *11* (1), e0146588. https://doi.org/10.1371/journal.pone.0146588.

(149) Corr, D. T.; Gallant-Behm, C. L.; Shrive, N. G.; Hart, D. A. Biomechanical Behavior of Scar Tissue and Uninjured Skin in a Porcine Model. *Wound Repair Regen.* **2009**, *17* (2), 250–259. https://doi.org/10.1111/j.1524-475X.2009.00463.x.

(150) Asbach, P.; Klatt, D.; Hamhaber, U.; Braun, J.; Somasundaram, R.; Hamm, B.; Sack, I. Assessment of Liver Viscoelasticity Using Multifrequency MR Elastography. *Magn. Reson. Med.* **2008**, *60* (2), 373–379. https://doi.org/10.1002/mrm.21636.

(151) Baghban, M.; Mojra, A. Early Relaxation Time Assessment for Characterization of Breast Tissue and Diagnosis of Breast Tumors. *J. Mech. Behav. Biomed. Mater.* **2018**, *87*, 325–335. https://doi.org/10.1016/j.jmbbm.2018.07.037.

(152) Kumar, V.; Denis, M.; Gregory, A.; Bayat, M.; Mehrmohammadi, M.; Fazzio, R.; Fatemi, M.; Alizad, A. Viscoelastic Parameters as Discriminators of Breast Masses: Initial Human Study Results. *PLOS ONE* **2018**, *13* (10), e0205717. https://doi.org/10.1371/journal.pone.0205717.

(153) Qiu, Y.; Sridhar, M.; Tsou, J. K.; Lindfors, K. K.; Insana, M. F. Ultrasonic Viscoelasticity Imaging of Nonpalpable Breast Tumors: Preliminary Results. *Acad. Radiol.* **2008**, *15* (12), 1526–1533. https://doi.org/10.1016/j.acra.2008.05.023.

(154) Sinkus, R.; Tanter, M.; Catheline, S.; Lorenzen, J.; Kuhl, C.; Sondermann, E.; Fink, M. Imaging Anisotropic and Viscous Properties of Breast Tissue by Magnetic Resonance-Elastography. *Magn. Reson. Med.* **2005**, *53* (2), 372–387. https://doi.org/10.1002/mrm.20355.

(155) Sinkus, R.; Tanter, M.; Xydeas, T.; Catheline, S.; Bercoff, J.; Fink, M. Viscoelastic Shear Properties of in Vivo Breast Lesions Measured by MR Elastography. *Proc. Seventh Int. Conf. Recent Adv. MR Appl. Porous Media* **2005**, *23* (2), 159–165. https://doi.org/10.1016/j.mri.2004.11.060.

(156) Balleyguier, C.; Lakhdar, A. B.; Dunant, A.; Mathieu, M.-C.; Delaloge, S.; Sinkus, R. Value of Whole Breast Magnetic Resonance Elastography Added to MRI for Lesion Characterization. *NMR Biomed.* **2018**, *31* (1), e3795. https://doi.org/10.1002/nbm.3795.

(157) Nabavizadeh, A.; Bayat, M.; Kumar, V.; Gregory, A.; Webb, J.; Alizad, A.; Fatemi, M. Viscoelastic Biomarker for Differentiation of Benign and Malignant Breast Lesion in Ultra- Low Frequency Range. *Sci. Rep.* **2019**, *9* (1), 5737. https://doi.org/10.1038/s41598-019-41885-9.

(158) Zhang, H.; Guo, Y.; Zhou, Y.; Zhu, H.; Wu, P.; Wang, K.; Ruan, L.; Wan, M.; Insana, M. F. Fluidity and Elasticity Form a Concise Set of Viscoelastic Biomarkers for Breast

Cancer Diagnosis Based on Kelvin–Voigt Fractional Derivative Modeling. *Biomech. Model. Mechanobiol.* **2020**. https://doi.org/10.1007/s10237-020-01330-7.

(159) Du, C.; Hill, R. J. Linear Viscoelasticity of Weakly Cross-Linked Hydrogels. *J. Rheol.* **2018**, *63* (1), 109–124. https://doi.org/10.1122/1.5052160.

(160) Cameron, Andrew. R.; Frith, Jessica. E.; Cooper-White, Justin. J. The Influence of Substrate Creep on Mesenchymal Stem Cell Behaviour and Phenotype. *Biomaterials* **2011**, *32* (26), 5979–5993. https://doi.org/10.1016/j.biomaterials.2011.04.003.

(161) Cameron, A. R.; Frith, J. E.; Gomez, G. A.; Yap, A. S.; Cooper-White, J. J. The Effect of Time-Dependent Deformation of Viscoelastic Hydrogels on Myogenic Induction and Rac1 Activity in Mesenchymal Stem Cells. *Biomaterials* **2014**, *35* (6), 1857–1868. https://doi.org/10.1016/j.biomaterials.2013.11.023.

(162) Mattei, G.; Cacopardo, L.; Ahluwalia, A. Micro-Mechanical Viscoelastic Properties of Crosslinked Hydrogels Using the Nano-Epsilon Dot Method. *Mater. Basel Switz.* **2017**, *10* (8), 889. https://doi.org/10.3390/ma10080889.

(163) Mattei, G.; Cacopardo, L.; Ahluwalia, A. A. Engineering Gels with Time-Evolving Viscoelasticity. *Mater. Basel Switz.* **2020**, *13* (2), 438. https://doi.org/10.3390/ma13020438.

(164) Murrell, M.; Kamm, R.; Matsudaira, P. Substrate Viscosity Enhances Correlation in Epithelial Sheet Movement. *Biophys. J.* **2011**, *101* (2), 297–306. https://doi.org/10.1016/j.bpj.2011.05.048.

(165) Cacopardo, L.; Guazzelli, N.; Nossa, R.; Mattei, G.; Ahluwalia, A. Engineering Hydrogel Viscoelasticity. *J. Mech. Behav. Biomed. Mater.* **2019**, *89*, 162–167. https://doi.org/10.1016/j.jmbbm.2018.09.031.

(166) Charrier, E. E.; Pogoda, K.; Wells, R. G.; Janmey, P. A. Control of Cell Morphology and Differentiation by Substrates with Independently Tunable Elasticity and Viscous Dissipation. *Nat. Commun.* **2018**, *9* (1), 449. https://doi.org/10.1038/s41467-018-02906-9.

(167) Charrier, E. E.; Pogoda, K.; Li, R.; Park, C. Y.; Fredberg, J. J.; Janmey, P. A. A Novel Method to Make Viscoelastic Polyacrylamide Gels for Cell Culture and Traction Force Microscopy. *APL Bioeng.* **2020**, *4* (3), 036104. https://doi.org/10.1063/5.0002750.

(168) Marozas, I. A.; Cooper-White, J. J.; Anseth, K. S. Photo-Induced Viscoelasticity in Cytocompatible Hydrogel Substrates. *New J. Phys.* **2019**, *21* (4), 045004. https://doi.org/10.1088/1367-2630/ab1309.

(169) Hui, E.; Gimeno, K. I.; Guan, G.; Caliari, S. R. Spatiotemporal Control of Viscoelasticity in Phototunable Hyaluronic Acid Hydrogels. *Biomacromolecules* **2019**, *20* (11), 4126–4134. https://doi.org/10.1021/acs.biomac.9b00965.

(170) Bauer, A.; Gu, L.; Kwee, B.; Li, W. A.; Dellacherie, M.; Celiz, A. D.; Mooney, D. J. Hydrogel Substrate Stress-Relaxation Regulates the Spreading and Proliferation of Mouse Myoblasts. *Acta Biomater.* **2017**, *62*, 82–90. https://doi.org/10.1016/j.actbio.2017.08.041.

(171) Chaudhuri, O.; Gu, L.; Darnell, M.; Klumpers, D.; Bencherif, S. A.; Weaver, J. C.; Huebsch, N.; Mooney, D. J. Substrate Stress Relaxation Regulates Cell Spreading. *Nat. Commun.* **2015**, *6* (1), 6365. https://doi.org/10.1038/ncomms7365.

(172) Chaudhuri, O.; Gu, L.; Klumpers, D.; Darnell, M.; Bencherif, S. A.; Weaver, J. C.; Huebsch, N.; Lee, H.-P.; Lippens, E.; Duda, G. N.; Mooney, D. J. Hydrogels with

Tunable Stress Relaxation Regulate Stem Cell Fate and Activity. *Nat. Mater.* **2016**, *15* (3), 326–334. https://doi.org/10.1038/nmat4489.

(173) Rodell, C. B.; MacArthur Jr., J. W.; Dorsey, S. M.; Wade, R. J.; Wang, L. L.; Woo, Y. J.; Burdick, J. A. Shear-Thinning Supramolecular Hydrogels with Secondary Autonomous Covalent Crosslinking to Modulate Viscoelastic Properties In Vivo. *Adv. Funct. Mater.* **2015**, *25* (4), 636–644. https://doi.org/10.1002/adfm.201403550.

(174) Lou, J.; Stowers, R.; Nam, S.; Xia, Y.; Chaudhuri, O. Stress Relaxing Hyaluronic Acid-Collagen Hydrogels Promote Cell Spreading, Fiber Remodeling, and Focal Adhesion Formation in 3D Cell Culture. *Biomaterials* **2018**, *154*, 213–222. https://doi.org/10.1016/j.biomaterials.2017.11.004.

(175) McKinnon, D. D.; Domaille, D. W.; Cha, J. N.; Anseth, K. S. Biophysically Defined and Cytocompatible Covalently Adaptable Networks as Viscoelastic 3D Cell Culture Systems. *Adv. Mater.* **2014**, *26* (6), 865–872. https://doi.org/10.1002/adma.201303680.

(176) Brown, T. E.; Carberry, B. J.; Worrell, B. T.; Dudaryeva, O. Y.; McBride, M. K.; Bowman, C. N.; Anseth, K. S. Photopolymerized Dynamic Hydrogels with Tunable Viscoelastic Properties through Thioester Exchange. *Biomaterials* **2018**, *178*, 496–503. https://doi.org/10.1016/j.biomaterials.2018.03.060.

(177) Nam, S.; Stowers, R.; Lou, J.; Xia, Y.; Chaudhuri, O. Varying PEG Density to Control Stress Relaxation in Alginate-PEG Hydrogels for 3D Cell Culture Studies. *Biomaterials* **2019**, *200*, 15–24. https://doi.org/10.1016/j.biomaterials.2019.02.004.

(178) Vining, K. H.; Stafford, A.; Mooney, D. J. Sequential Modes of Crosslinking Tune Viscoelasticity of Cell-Instructive Hydrogels. *Biomaterials* **2019**, *188*, 187–197. https://doi.org/10.1016/j.biomaterials.2018.10.013.

(179) Wisdom, K. M.; Adebowale, K.; Chang, J.; Lee, J. Y.; Nam, S.; Desai, R.; Rossen, N. S.; Rafat, M.; West, R. B.; Hodgson, L.; Chaudhuri, O. Matrix Mechanical Plasticity Regulates Cancer Cell Migration through Confining Microenvironments. *Nat. Commun.* **2018**, *9* (1), 4144–4144. https://doi.org/10.1038/s41467-018-06641-z.

(180) Kim, J.; Feng, J.; Jones, C. A. R.; Mao, X.; Sander, L. M.; Levine, H.; Sun, B. Stress-Induced Plasticity of Dynamic Collagen Networks. *Nat. Commun.* **2017**, *8* (1), 842. https://doi.org/10.1038/s41467-017-01011-7.

(181) Ban, E.; Franklin, J. M.; Nam, S.; Smith, L. R.; Wang, H.; Wells, R. G.; Chaudhuri, O.; Liphardt, J. T.; Shenoy, V. B. Mechanisms of Plastic Deformation in Collagen Networks Induced by Cellular Forces. *Biophys. J.* **2018**, *114* (2), 450–461. https://doi.org/10.1016/j.bpj.2017.11.3739.

(182) Liu, A. S.; Wang, H.; Copeland, C. R.; Chen, C. S.; Shenoy, V. B.; Reich, D. H. Matrix Viscoplasticity and Its Shielding by Active Mechanics in Microtissue Models: Experiments and Mathematical Modeling. *Sci. Rep.* **2016**, *6* (1), 33919. https://doi.org/10.1038/srep33919.

(183) Wisdom, K. M.; Indana, D.; Chou, P.-E.; Desai, R.; Kim, T.; Chaudhuri, O. Covalent Cross-Linking of Basement Membrane-like Matrices Physically Restricts Invasive Protrusions in Breast Cancer Cells. *Matrix Biomech.* **2020**, *85–86*, 94–111. https://doi.org/10.1016/j.matbio.2019.05.006.

(184) Beca, B. M.; Sun, Y.; Wong, E.; Moraes, C.; Simmons, C. A. Dynamic Bioreactors with Integrated Microfabricated Devices for Mechanobiological Screening. *Tissue Eng. Part C Methods* **2019**, *25* (10), 581–592. https://doi.org/10.1089/ten.tec.2019.0121.

(185) Gupta, V.; Grande-Allen, K. J. Effects of Static and Cyclic Loading in Regulating Extracellular Matrix Synthesis by Cardiovascular Cells. *Cardiovasc. Res.* **2006**, *72* (3), 375–383. https://doi.org/10.1016/j.cardiores.2006.08.017.

(186) Hur, S. S.; Jeong, J. H.; Ban, M. J.; Park, J. H.; Yoon, J. K.; Hwang, Y. Traction Force Microscopy for Understanding Cellular Mechanotransduction. *BMB Rep.* **2020**, *53* (2), 74–81. https://doi.org/10.5483/BMBRep.2020.53.2.308.

(187) Horning, J. L.; Sahoo, S. K.; Vijayaraghavalu, S.; Dimitrijevic, S.; Vasir, J. K.; Jain, T. K.; Panda, A. K.; Labhasetwar, V. 3-D Tumor Model for In Vitro Evaluation of Anticancer Drugs. *Mol. Pharm.* **2008**, *5* (5), 849–862. https://doi.org/10.1021/mp800047v.

(188) Legant, W. R.; Miller, J. S.; Blakely, B. L.; Cohen, D. M.; Genin, G. M.; Chen, C. S. Measurement of Mechanical Tractions Exerted by Cells in Three-Dimensional Matrices. *Nat. Methods* **2010**, *7* (12), 969–971. https://doi.org/10.1038/nmeth.1531.

(189) LaCroix, A. S.; Lynch, A. D.; Berginski, M. E.; Hoffman, B. D. Tunable Molecular Tension Sensors Reveal Extension-Based Control of Vinculin Loading. *eLife* **2018**, *7*, e33927. https://doi.org/10.7554/eLife.33927.

(190) Fu, J.; Wang, Y.-K.; Yang, M. T.; Desai, R. A.; Yu, X.; Liu, Z.; Chen, C. S. Mechanical Regulation of Cell Function with Geometrically Modulated Elastomeric Substrates. *Nat. Methods* **2010**, *7* (9), 733–736. https://doi.org/10.1038/nmeth.1487.

(191) Legant, W. R.; Pathak, A.; Yang, M. T.; Deshpande, V. S.; McMeeking, R. M.; Chen, C. S. Microfabricated Tissue Gauges to Measure and Manipulate Forces from 3D Microtissues. *Proc. Natl. Acad. Sci.* **2009**, *106* (25), 10097. https://doi.org/10.1073/pnas.0900174106.

(192) Eastwood, M.; McGrouther, D. A.; Brown, R. A. A Culture Force Monitor for Measurement of Contraction Forces Generated in Human Dermal Fibroblast Cultures: Evidence for Cell-Matrix Mechanical Signalling. *Biochim. Biophys. Acta BBA - Gen. Subj.* **1994**, *1201* (2), 186–192. https://doi.org/10.1016/0304-4165(94)90040-X.

(193) Wang, X.; Gao, Q.; Han, X.; Bu, B.; Wang, L.; Li, A.; Deng, L. Sensitive Detection of Cell-Derived Force and Collagen Matrix Tension in Microtissues Undergoing Large-Scale Densification. *Proc. Natl. Acad. Sci.* **2021**, *118* (36), e2106061118. https://doi.org/10.1073/pnas.2106061118.

(194) Campàs, O.; Mammoto, T.; Hasso, S.; Sperling, R. A.; O'Connell, D.; Bischof, A. G.; Maas, R.; Weitz, D. A.; Mahadevan, L.; Ingber, D. E. Quantifying Cell-Generated Mechanical Forces within Living Embryonic Tissues. *Nat. Methods* **2014**, *11* (2), 183–189. https://doi.org/10.1038/nmeth.2761.

(195) Mohagheghian, E.; Luo, J.; Chen, J.; Chaudhary, G.; Chen, J.; Sun, J.; Ewoldt, R. H.; Wang, N. Quantifying Compressive Forces between Living Cell Layers and within Tissues Using Elastic Round Microgels. *Nat. Commun.* **2018**, *9* (1), 1878. https://doi.org/10.1038/s41467-018-04245-1.

(196) Dolega, M. E.; Delarue, M.; Ingremeau, F.; Prost, J.; Delon, A.; Cappello, G. Cell-like Pressure Sensors Reveal Increase of Mechanical Stress towards the Core of Multicellular Spheroids under Compression. *Nat. Commun.* **2017**, *8* (1), 14056. https://doi.org/10.1038/ncomms14056.

(197) Ingremeau, F.; Dolega, M. E.; Gallagher, J.; Wang, I.; Cappello, G.; Delon, A. Optical Sensing of Mechanical Pressure Based on Diffusion Measurement in Polyacrylamide Cell-like Barometers. *Soft Matter* **2017**, *13* (23), 4210–4213. https://doi.org/10.1039/C6SM02887J.

(198) Lee, W.; Kalashnikov, N.; Mok, S.; Halaoui, R.; Kuzmin, E.; Putnam, A. J.; Takayama, S.; Park, M.; McCaffrey, L.; Zhao, R.; Leask, R. L.; Moraes, C. Dispersible Hydrogel Force Sensors Reveal Patterns of Solid Mechanical Stress in Multicellular Spheroid Cultures. *Nat. Commun.* **2019**, *10* (1), 144. https://doi.org/10.1038/s41467-018-07967-4.

(199) Cancer Facts & Figures. American Cancer Society 2020.

(200) Lin, C.-H.; Pelissier, F. A.; Zhang, H.; Lakins, J.; Weaver, V. M.; Park, C.; LaBarge, M. A. Microenvironment Rigidity Modulates Responses to the HER2 Receptor Tyrosine Kinase Inhibitor Lapatinib via YAP and TAZ Transcription Factors. *Mol. Biol. Cell* **2015**, *26* (22), 3946–3953. https://doi.org/10.1091/mbc.E15-07-0456.

(201) Dhiman, H. K.; Ray, A. R.; Panda, A. K. Three-Dimensional Chitosan Scaffold-Based MCF-7 Cell Culture for the Determination of the Cytotoxicity of Tamoxifen. *Biomaterials* **2005**, *26* (9), 979–986. https://doi.org/10.1016/j.biomaterials.2004.04.012.

(202) Leung, B. M.; Moraes, C.; Cavnar, S. P.; Luker, K. E.; Luker, G. D.; Takayama, S. Microscale 3D Collagen Cell Culture Assays in Conventional Flat-Bottom 384-Well Plates. *J. Lab. Autom.* **2014**, *20* (2), 138–145. https://doi.org/10.1177/2211068214563793.

(203) Ho, W. J.; Pham, E. A.; Kim, J. W.; Ng, C. W.; Kim, J. H.; Kamei, D. T.; Wu, B. M. Incorporation of Multicellular Spheroids into 3-D Polymeric Scaffolds Provides an Improved Tumor Model for Screening Anticancer Drugs. *Cancer Sci.* **2010**, *101* (12), 2637–2643. https://doi.org/10.1111/j.1349-7006.2010.01723.x.

(204) Li, J.; Mooney, D. J. Designing Hydrogels for Controlled Drug Delivery. *Nature reviews. Materials* **2016**, *1* (12), 16071. https://doi-org.proxy3.library.mcgill.ca/10.1038/natrevmats.2016.71.

(205) Joyce, M. H.; Lu, C.; James, E. R.; Hegab, R.; Allen, S. C.; Suggs, L. J.; Brock, A. Phenotypic Basis for Matrix Stiffness-Dependent Chemoresistance of Breast Cancer Cells to Doxorubicin. *Front. Oncol.* **2018**, *8*, 337–337. https://doi.org/10.3389/fonc.2018.00337.

(206) Malandrino, A.; Trepat, X.; Kamm, R. D.; Mak, M. Dynamic Filopodial Forces Induce Accumulation, Damage, and Plastic Remodeling of 3D Extracellular Matrices. *PLOS Comput. Biol.* **2019**, *15* (4), e1006684. https://doi.org/10.1371/journal.pcbi.1006684.

(207) Campàs, O.; Mammoto, T.; Hasso, S.; Sperling, R. A.; O'Connell, D.; Bischof, A. G.; Maas, R.; Weitz, D. A.; Mahadevan, L.; Ingber, D. E. Quantifying Cell-Generated Mechanical Forces within Living Embryonic Tissues. *Nat. Methods* **2014**, *11* (2), 183–189. https://doi.org/10.1038/nmeth.2761.

(208) Mongera, A.; Rowghanian, P.; Gustafson, H. J.; Shelton, E.; Kealhofer, D. A.; Carn, E. K.; Serwane, F.; Lucio, A. A.; Giammona, J.; Campàs, O. A Fluid-to-Solid Jamming Transition Underlies Vertebrate Body Axis Elongation. *Nature* **2018**, *561* (7723), 401–405. https://doi.org/10.1038/s41586-018-0479-2.

(209) Mohagheghian, E.; Luo, J.; Chen, J.; Chaudhary, G.; Chen, J.; Sun, J.; Ewoldt, R. H.; Wang, N. Quantifying Compressive Forces between Living Cell Layers and within Tissues Using Elastic Round Microgels. *Nat. Commun.* **2018**, *9* (1), 1878. https://doi.org/10.1038/s41467-018-04245-1.

(210) Mok, S.; Al Habyan, S.; Ledoux, C.; Lee, W.; MacDonald, K.; McCaffrey, L.; Moraes, C. Mapping Cellular-Scale Internal Stiffness in 3D Tissues with Smart Material Hydrogel Probes. *bioRxiv* **2019**, 840736. https://doi.org/10.1101/840736.

(211) Proestaki, M.; Ogren, A.; Burkel, B.; Notbohm, J. Modulus of Fibrous Collagen at the Length Scale of a Cell. *Experimental mechanics* **2019**, *59* (9), 1323–1334. https://doi-org.proxy3.library.mcgill.ca/10.1007/s11340-018-00453-4.

(212) Serwane, F.; Mongera, A.; Rowghanian, P.; Kealhofer, D. A.; Lucio, A. A.; Hockenbery, Z. M.; Campàs, O. In Vivo Quantification of Spatially Varying Mechanical Properties in Developing Tissues. *Nat. Methods* **2017**, *14* (2), 181–186. https://doi.org/10.1038/nmeth.4101.

(213) Li, X.; Zhang, X.; Zhao, S.; Wang, J.; Liu, G.; Du, Y. Micro-Scaffold Array Chip for Upgrading Cell-Based High-Throughput Drug Testing to 3D Using Benchtop Equipment. *Lab. Chip* **2014**, *14* (3), 471–481. https://doi.org/10.1039/C3LC51103K.

(214) Yan, X.; Zhou, L.; Wu, Z.; Wang, X.; Chen, X.; Yang, F.; Guo, Y.; Wu, M.; Chen, Y.; Li, W.; Wang, J.; Du, Y. High Throughput Scaffold-Based 3D Micro-Tumor Array for Efficient Drug Screening and Chemosensitivity Testing. *Organoids Ex Vivo Tissue -Chip Technol.* **2019**, *198*, 167–179. https://doi.org/10.1016/j.biomaterials.2018.05.020.

(215) Moraes, C.; Simon, A. B.; Putnam, A. J.; Takayama, S. Aqueous Two-Phase Printing of Cell-Containing Contractile Collagen Microgels. *Biomaterials* **2013**, *34* (37), 10.1016/j.biomaterials.2013.08.046. https://doi.org/10.1016/j.biomaterials.2013.08.046.

(216) Gungor-Ozkerim, P. S.; Inci, I.; Zhang, Y. S.; Khademhosseini, A.; Dokmeci, M. R. Bioinks for 3D Bioprinting: An Overview. *Biomater. Sci.* **2018**, *6* (5), 915–946. https://doi.org/10.1039/C7BM00765E.

(217) Azizipour, N.; Avazpour, R.; Rosenzweig, D. H.; Sawan, M.; Ajji, A. Evolution of Biochip Technology: A Review from Lab-on-a-Chip to Organ-on-a-Chip. *Micromachines* **2020**, *11* (6). https://doi.org/10.3390/mi11060599.

(218) Khavari, A.; Nydén, M.; Weitz, D. A.; Ehrlicher, A. J. Composite Alginate Gels for Tunable Cellular Microenvironment Mechanics. *Sci. Rep.* **2016**, *6* (1), 30854. https://doi.org/10.1038/srep30854.

(219) Yeung, T.; Georges, P. C.; Flanagan, L. A.; Marg, B.; Ortiz, M.; Funaki, M.; Zahir, N.; Ming, W.; Weaver, V.; Janmey, P. A. Effects of Substrate Stiffness on Cell Morphology, Cytoskeletal Structure, and Adhesion. *Cell Motil.* **2005**, *60* (1), 24–34. https://doi.org/10.1002/cm.20041.

(220) Ort, C.; Lee, W.; Kalashnikov, N.; Moraes, C. Disentangling the Fibrous Microenvironment: Designer Culture Models for Improved Drug Discovery. *Expert Opin. Drug Discov.* **2020**, 1–13. https://doi.org/10.1080/17460441.2020.1822815.

(221) Zustiak, S.; Nossal, R.; Sackett, D. L. Multiwell Stiffness Assay for the Study of Cell Responsiveness to Cytotoxic Drugs. *Biotechnol. Bioeng.* **2014**, *111* (2), 396–403. https://doi.org/10.1002/bit.25097.

(222) Cruz-Acuña, R.; Quirós, M.; Huang, S.; Siuda, D.; Spence, J. R.; Nusrat, A.; García, A. J. PEG-4MAL Hydrogels for Human Organoid Generation, Culture, and in Vivo Delivery. *Nat. Protoc.* **2018**, *13* (9), 2102–2119. https://doi.org/10.1038/s41596-018-0036-3.

(223) Gjorevski, N.; Sachs, N.; Manfrin, A.; Giger, S.; Bragina, M. E.; Ordóñez-Morán, P.; Clevers, H.; Lutolf, M. P. Designer Matrices for Intestinal Stem Cell and Organoid Culture. *Nature* **2016**, *539* (7630), 560–564. https://doi.org/10.1038/nature20168.

(224) Capeling, M. M.; Czerwinski, M.; Huang, S.; Tsai, Y.-H.; Wu, A.; Nagy, M. S.; Juliar, B.; Sundaram, N.; Song, Y.; Han, W. M.; Takayama, S.; Alsberg, E.; Garcia, A. J.; Helmrath, M.; Putnam, A. J.; Spence, J. R. Nonadhesive Alginate Hydrogels Support

Growth of Pluripotent Stem Cell-Derived Intestinal Organoids. *Stem Cell Rep.* **2019**, *12* (2), 381–394. https://doi.org/10.1016/j.stemcr.2018.12.001.

(225) Ranga, A.; Girgin, M.; Meinhardt, A.; Eberle, D.; Caiazzo, M.; Tanaka, E. M.; Lutolf, M. P. Neural Tube Morphogenesis in Synthetic 3D Microenvironments. *Proc. Natl. Acad. Sci.* **2016**, *113* (44), E6831. https://doi.org/10.1073/pnas.1603529113.

(226) Ouyang, L.; Armstrong, J. P. K.; Lin, Y.; Wojciechowski, J. P.; Lee-Reeves, C.; Hachim, D.; Zhou, K.; Burdick, J. A.; Stevens, M. M. Expanding and Optimizing 3D Bioprinting Capabilities Using Complementary Network Bioinks. *Sci. Adv.* **2020**, *6* (38), eabc5529. https://doi.org/10.1126/sciadv.abc5529.

(227) Brassard, J. A.; Nikolaev, M.; Hübscher, T.; Hofer, M.; Lutolf, M. P. Recapitulating Macro-Scale Tissue Self-Organization through Organoid Bioprinting. *Nat. Mater.* **2020**. https://doi.org/10.1038/s41563-020-00803-5.

(228) Yang, X.; Lu, Z.; Wu, H.; Li, W.; Zheng, L.; Zhao, J. Collagen-Alginate as Bioink for Three-Dimensional (3D) Cell Printing Based Cartilage Tissue Engineering. *Mater. Sci. Eng. C* **2018**, *83*, 195–201. https://doi.org/10.1016/j.msec.2017.09.002.

(229) Datta, P.; Dey, M.; Ataie, Z.; Unutmaz, D.; Ozbolat, I. T. 3D Bioprinting for Reconstituting the Cancer Microenvironment. *Npj Precis. Oncol.* **2020**, *4* (1), 18. https://doi.org/10.1038/s41698-020-0121-2.

(230) Jiang, T.; Munguia-Lopez, J. G.; Gu, K.; Bavoux, M. M.; Flores-Torres, S.; Kort-Mascort, J.; Grant, J.; Vijayakumar, S.; De Leon-Rodriguez, A.; Ehrlicher, A. J.; Kinsella, J. M. Engineering Bioprintable Alginate/Gelatin Composite Hydrogels with Tunable Mechanical and Cell Adhesive Properties to Modulate Tumor Spheroid Growth Kinetics. *Biofabrication* **2019**, *12* (1), 015024. https://doi.org/10.1088/1758-5090/ab3a5c.

(231) Gillette, B. M.; Jensen, J. A.; Wang, M.; Tchao, J.; Sia, S. K. Dynamic Hydrogels: Switching of 3D Microenvironments Using Two-Component Naturally Derived Extracellular Matrices. *Adv. Mater.* **2010**, *22* (6), 686–691. https://doi.org/10.1002/adma.200902265.

(232) Cavo, M.; Caria, M.; Pulsoni, I.; Beltrame, F.; Fato, M.; Scaglione, S. A New Cell-Laden 3D Alginate-Matrigel Hydrogel Resembles Human Breast Cancer Cell Malignant Morphology, Spread and Invasion Capability Observed “in Vivo.” *Sci. Rep.* **2018**, *8* (1), 5333. https://doi.org/10.1038/s41598-018-23250-4.

(233) Branco da Cunha, C.; Klumpers, D. D.; Li, W. A.; Koshy, S. T.; Weaver, J. C.; Chaudhuri, O.; Granja, P. L.; Mooney, D. J. Influence of the Stiffness of Three-Dimensional Alginate/Collagen-I Interpenetrating Networks on Fibroblast Biology. *Biomaterials* **2014**, *35* (32), 8927–8936. https://doi.org/10.1016/j.biomaterials.2014.06.047.

(234) Lee, K. Y.; Mooney, D. J. Alginate: Properties and Biomedical Applications. *Prog. Polym. Sci.* **2012**, *37* (1), 106–126. https://doi.org/10.1016/j.progpolymsci.2011.06.003.

(235) Giancotti, F. G.; Ruoslahti, E. Integrin Signaling. *Science* **1999**, *285* (5430), 1028. https://doi.org/10.1126/science.285.5430.1028.

(236) Engler, A.; Bacakova, L.; Newman, C.; Hategan, A.; Griffin, M.; Discher, D. Substrate Compliance versus Ligand Density in Cell on Gel Responses. *Biophys. J.* **2004**, *86* (1), 617–628. https://doi.org/10.1016/S0006-3495(04)74140-5.

(237) Clapham, D. E. Calcium Signaling. *Cell* **2007**, *131* (6), 1047–1058. https://doi.org/10.1016/j.cell.2007.11.028.

(238) Han, Y. L.; Ronceray, P.; Xu, G.; Malandrino, A.; Kamm, R. D.; Lenz, M.; Broedersz, C. P.; Guo, M. Cell Contraction Induces Long-Ranged Stress Stiffening in the Extracellular

Matrix. *Proc. Natl. Acad. Sci. U. S. A.* **2018**, *115* (16), 4075–4080. https://doi.org/10.1073/pnas.1722619115.

(239) Joyce, M. H.; Lu, C.; James, E. R.; Hegab, R.; Allen, S. C.; Suggs, L. J.; Brock, A. Phenotypic Basis for Matrix Stiffness-Dependent Chemoresistance of Breast Cancer Cells to Doxorubicin. *Front. Oncol.* **2018**, *8*, 337–337. https://doi.org/10.3389/fonc.2018.00337.

(240) Shin, J.-W.; Mooney, D. J. Extracellular Matrix Stiffness Causes Systematic Variations in Proliferation and Chemosensitivity in Myeloid Leukemias. *Proc. Natl. Acad. Sci. U. S. A.* **2016**, *113* (43), 12126–12131. https://doi.org/10.1073/pnas.1611338113.

(241) Jing, H.; Cheng, W.; Li, Z.-Y.; Ying, L.; Wang, Q.-C.; Wu, T.; Tian, J.-W. Early Evaluation of Relative Changes in Tumor Stiffness by Shear Wave Elastography Predicts the Response to Neoadjuvant Chemotherapy in Patients With Breast Cancer. *J. Ultrasound Med.* **2016**, *35* (8), 1619–1627. https://doi.org/10.7863/ultra.15.08052.

(242) Weaver, B. A. How Taxol/Paclitaxel Kills Cancer Cells. *Mol. Biol. Cell* **2014**, *25* (18), 2677–2681. https://doi.org/10.1091/mbc.E14-04-0916.

(243) Asmani, M.; Velumani, S.; Li, Y.; Wawrzyniak, N.; Hsia, I.; Chen, Z.; Hinz, B.; Zhao, R. Fibrotic Microtissue Array to Predict Anti-Fibrosis Drug Efficacy. *Nat. Commun.* **2018**, *9* (1), 2066. https://doi.org/10.1038/s41467-018-04336-z.

(244) Calvo, F.; Ege, N.; Grande-Garcia, A.; Hooper, S.; Jenkins, R. P.; Chaudhry, S. I.; Harrington, K.; Williamson, P.; Moeendarbary, E.; Charras, G.; Sahai, E. Mechanotransduction and YAP-Dependent Matrix Remodelling Is Required for the Generation and Maintenance of Cancer-Associated Fibroblasts. *Nat. Cell Biol.* **2013**, *15* (6), 637–646. https://doi.org/10.1038/ncb2756.

(245) Khavari, A.; Ehrlicher, A. J. Nuclei Deformation Reveals Pressure Distributions in 3D Cell Clusters. *PLOS ONE* **2019**, *14* (9), e0221753. https://doi.org/10.1371/journal.pone.0221753.

(246) Stamenović, D.; Smith, M. L. Tensional Homeostasis at Different Length Scales. *Soft Matter* **2020**, *16* (30), 6946–6963. https://doi.org/10.1039/D0SM00763C.

(247) Sakar, M. S.; Eyckmans, J.; Pieters, R.; Eberli, D.; Nelson, B. J.; Chen, C. S. Cellular Forces and Matrix Assembly Coordinate Fibrous Tissue Repair. *Nat. Commun.* **2016**, *7* (1), 11036. https://doi.org/10.1038/ncomms11036.

(248) Kollmannsberger, P.; Bidan, C. M.; Dunlop, J. W. C.; Fratzl, P.; Vogel, V. Tensile Forces Drive a Reversible Fibroblast-to-Myofibroblast Transition during Tissue Growth in Engineered Clefts. *Sci. Adv.* **2018**, *4* (1), eaao4881. https://doi.org/10.1126/sciadv.aao4881.

(249) Ort, C.; Chen, Y.; Ghagre, A.; Ehrlicher, A.; Moraes, C. Bioprintable, Stiffness-Tunable Collagen-Alginate Microgels for Increased Throughput 3D Cell Culture Studies. *ACS Biomater. Sci. Eng.* **2021**. https://doi.org/10.1021/acsbiomaterials.1c00129.

(250) Dubois, S. J.; Kalashnikov, N.; Moraes, C. Robust and Precise Wounding and Analysis of Engineered Contractile Tissues. *Tissue Eng. Part C Methods* **2019**, *25* (11), 677–686. https://doi.org/10.1089/ten.tec.2019.0123.

(251) Boekema, B. K. H. L.; Vlig, M.; Olde Damink, L.; Middelkoop, E.; Eummelen, L.; Bühren, A. V.; Ulrich, M. M. W. Effect of Pore Size and Cross-Linking of a Novel Collagen-Elastin Dermal Substitute on Wound Healing. *J. Mater. Sci. Mater. Med.* **2014**, *25* (2), 423–433. https://doi.org/10.1007/s10856-013-5075-2.

(252) Handorf, A. M.; Zhou, Y.; Halanski, M. A.; Li, W.-J. Tissue Stiffness Dictates Development, Homeostasis, and Disease Progression. *Organogenesis* **2015**, *11* (1), 1–15. https://doi.org/10.1080/15476278.2015.1019687.

(253) Talman, V.; Ruskoaho, H. Cardiac Fibrosis in Myocardial Infarction—from Repair and Remodeling to Regeneration. *Cell Tissue Res.* **2016**, *365* (3), 563–581. https://doi.org/10.1007/s00441-016-2431-9.

(254) Kim, B.-S.; Nikolovski, J.; Bonadio, J.; Mooney, D. J. Cyclic Mechanical Strain Regulates the Development of Engineered Smooth Muscle Tissue. *Nat. Biotechnol.* **1999**, *17* (10), 979–983. https://doi.org/10.1038/13671.

(255) Webb, K.; Hitchcock, R. W.; Smeal, R. M.; Li, W.; Gray, S. D.; Tresco, P. A. Cyclic Strain Increases Fibroblast Proliferation, Matrix Accumulation, and Elastic Modulus of Fibroblast-Seeded Polyurethane Constructs. *J. Biomech.* **2006**, *39* (6), 1136–1144. https://doi.org/10.1016/j.jbiomech.2004.08.026.

(256) Zhao, R.; Chen, C. S.; Reich, D. H. Force-Driven Evolution of Mesoscale Structure in Engineered 3D Microtissues and the Modulation of Tissue Stiffening. *Biomaterials* **2014**, *35* (19), 5056–5064. https://doi.org/10.1016/j.biomaterials.2014.02.020.

(257) Kural, M. H.; Billiar, K. L. Myofibroblast Persistence with Real-Time Changes in Boundary Stiffness. *Acta Biomater.* **2016**, *32*, 223–230. https://doi.org/10.1016/j.actbio.2015.12.031.

(258) Goffin, J. M.; Pittet, P.; Csucs, G.; Lussi, J. W.; Meister, J.-J.; Hinz, B. Focal Adhesion Size Controls Tension-Dependent Recruitment of α-Smooth Muscle Actin to Stress Fibers. *J. Cell Biol.* **2006**, *172* (2), 259–268. https://doi.org/10.1083/jcb.200506179.

(259) Yeung, T.; Georges, P. C.; Flanagan, L. A.; Marg, B.; Ortiz, M.; Funaki, M.; Zahir, N.; Ming, W.; Weaver, V.; Janmey, P. A. Effects of Substrate Stiffness on Cell Morphology, Cytoskeletal Structure, and Adhesion. *Cell Motil.* **2005**, *60* (1), 24–34. https://doi.org/10.1002/cm.20041.

(260) Caliari, S. R.; Perepelyuk, M.; Cosgrove, B. D.; Tsai, S. J.; Lee, G. Y.; Mauck, R. L.; Wells, R. G.; Burdick, J. A. Stiffening Hydrogels for Investigating the Dynamics of Hepatic Stellate Cell Mechanotransduction during Myofibroblast Activation. *Sci. Rep.* **2016**, *6*, 21387. https://doi.org/10.1038/srep21387.

(261) Roy, P.; Petroll, W. M.; Cavanagh, H. D.; Chuong, C. J.; Jester, J. V. Anin VitroForce Measurement Assay to Study the Early Mechanical Interaction between Corneal Fibroblasts and Collagen Matrix. *Exp. Cell Res.* **1997**, *232* (1), 106–117. https://doi.org/10.1006/excr.1997.3511.

(262) Kolodney, M.; Wysolmerski, R. Isometric Contraction by Fibroblasts and Endothelial Cells in Tissue Culture: A Quantitative Study. *J. Cell Biol.* **1992**, *117* (1), 73–82. https://doi.org/10.1083/jcb.117.1.73.

(263) Delvoye, Pierre.; Wiliquet, Philippe.; Levêque, J.-Luc.; Nusgens, B. V.; Lapière, C. M. Measurement of Mechanical Forces Generated by Skin Fibroblasts Embedded in a Three-Dimensional Collagen Gel. *J. Invest. Dermatol.* **1991**, *97* (5), 898–902. https://doi.org/10.1111/1523-1747.ep12491651.

(264) Georges, P. C.; Hui, J.-J.; Gombos, Z.; McCormick, M. E.; Wang, A. Y.; Uemura, M.; Mick, R.; Janmey, P. A.; Furth, E. E.; Wells, R. G. Increased Stiffness of the Rat Liver Precedes Matrix Deposition: Implications for Fibrosis. *Am. J. Physiol.-Gastrointest. Liver Physiol.* **2007**, *293* (6), G1147–G1154. https://doi.org/10.1152/ajpgi.00032.2007.

(265) Brown, R. A.; Prajapati, R.; McGrouther, D. A.; Yannas, I. V.; Eastwood, M. Tensional Homeostasis in Dermal Fibroblasts: Mechanical Responses to Mechanical Loading in Three-Dimensional Substrates. *J. Cell. Physiol.* **1998**, *175* (3), 323–332. https://doi.org/10.1002/(SICI)1097-4652(199806)175:3<323::AID-JCP10>3.0.CO;2-6.

(266) Mohagheghian, E.; Luo, J.; Chen, J.; Chaudhary, G.; Chen, J.; Sun, J.; Ewoldt, R. H.; Wang, N. Quantifying Compressive Forces between Living Cell Layers and within Tissues Using Elastic Round Microgels. *Nat. Commun.* **2018**, *9* (1), 1878. https://doi.org/10.1038/s41467-018-04245-1.

(267) Galbraith, C. G.; Sheetz, M. P. A Micromachined Device Provides a New Bend on Fibroblast Traction Forces. *Proc. Natl. Acad. Sci.* **1997**, *94* (17), 9114. https://doi.org/10.1073/pnas.94.17.9114.

(268) Squier, C. A. The Effect of Stretching on Formation of Myofibroblasts in Mouse Skin. *Cell Tissue Res.* **1981**, *220* (2), 325–335. https://doi.org/10.1007/BF00210512.

(269) Maheshwari, G.; Brown, G.; Lauffenburger, D. A.; Wells, A.; Griffith, L. G. Cell Adhesion and Motility Depend on Nanoscale RGD Clustering. *J. Cell Sci.* **2000**, *113* (10), 1677–1686. https://doi.org/10.1242/jcs.113.10.1677.

(270) Cavalcanti-Adam, E. A.; Volberg, T.; Micoulet, A.; Kessler, H.; Geiger, B.; Spatz, J. P. Cell Spreading and Focal Adhesion Dynamics Are Regulated by Spacing of Integrin Ligands. *Biophys. J.* **2007**, *92* (8), 2964–2974. https://doi.org/10.1529/biophysj.106.089730.

(271) Geiger, F.; Rüdiger, D.; Zahler, S.; Engelke, H. Fiber Stiffness, Pore Size and Adhesion Control Migratory Phenotype of MDA-MB-231 Cells in Collagen Gels. *PLOS ONE* **2019**, *14* (11), e0225215. https://doi.org/10.1371/journal.pone.0225215.

(272) Solon, J.; Levental, I.; Sengupta, K.; Georges, P. C.; Janmey, P. A. Fibroblast Adaptation and Stiffness Matching to Soft Elastic Substrates. *Biophys. J.* **2007**, *93* (12), 4453–4461. https://doi.org/10.1529/biophysj.106.101386.

(273) Feld, L.; Kellerman, L.; Mukherjee, A.; Livne, A.; Bouchbinder, E.; Wolfenson, H. Cellular Contractile Forces Are Nonmechanosensitive. *Sci. Adv.* **2020**, *6* (17), eaaz6997. https://doi.org/10.1126/sciadv.aaz6997.

(274) Pakshir, P.; Alizadehgiashi, M.; Wong, B.; Coelho, N. M.; Chen, X.; Gong, Z.; Shenoy, V. B.; McCulloch, C. A.; Hinz, B. Dynamic Fibroblast Contractions Attract Remote Macrophages in Fibrillar Collagen Matrix. *Nat. Commun.* **2019**, *10* (1), 1850. https://doi.org/10.1038/s41467-019-09709-6.

(275) Griffith, L. G.; Lopina, S. Microdistribution of Substratum-Bound Ligands Affects Cell Function: Hepatocyte Spreading on PEO-Tethered Galactose. *Biomaterials* **1998**, *19* (11), 979–986. https://doi.org/10.1016/S0142-9612(97)00185-3.

(276) McBeath, R.; Pirone, D. M.; Nelson, C. M.; Bhadriraju, K.; Chen, C. S. Cell Shape, Cytoskeletal Tension, and RhoA Regulate Stem Cell Lineage Commitment. *Dev. Cell* **2004**, *6* (4), 483–495. https://doi.org/10.1016/S1534-5807(04)00075-9.

(277) Pelham, R. J.; Wang, Y. L. Cell Locomotion and Focal Adhesions Are Regulated by the Mechanical Properties of the Substrate. *Biol. Bull.* **1998**, *194* (3), 348–350. https://doi.org/10.2307/1543109.

(278) Mitra, S. K.; Hanson, D. A.; Schlaepfer, D. D. Focal Adhesion Kinase: In Command and Control of Cell Motility. *Nat. Rev. Mol. Cell Biol.* **2005**, *6* (1), 56–68. https://doi.org/10.1038/nrm1549.

(279) Humphrey, J. D.; Dufresne, E. R.; Schwartz, M. A. Mechanotransduction and Extracellular Matrix Homeostasis. *Nat. Rev. Mol. Cell Biol.* **2014**, *15* (12), 802–812. https://doi.org/10.1038/nrm3896.

(280) Ingber, D. E. Cellular Mechanotransduction: Putting All the Pieces Together Again. *FASEB J.* **2006**, *20* (7), 811–827. https://doi.org/10.1096/fj.05-5424rev.

(281) Cheng, B.; Lin, M.; Huang, G.; Li, Y.; Ji, B.; Genin, G. M.; Deshpande, V. S.; Lu, T. J.; Xu, F. Cellular Mechanosensing of the Biophysical Microenvironment: A Review of Mathematical Models of Biophysical Regulation of Cell Responses. *Phys. Life Rev.* **2017**, *22–23*, 88–119. https://doi.org/10.1016/j.plrev.2017.06.016.

(282) Chan, C. E.; Odde, D. J. Traction Dynamics of Filopodia on Compliant Substrates. *Science* **2008**, *322* (5908), 1687. https://doi.org/10.1126/science.1163595.

(283) Gong, Z.; Szczesny, S. E.; Caliari, S. R.; Charrier, E. E.; Chaudhuri, O.; Cao, X.; Lin, Y.; Mauck, R. L.; Janmey, P. A.; Burdick, J. A.; Shenoy, V. B. Matching Material and Cellular Timescales Maximizes Cell Spreading on Viscoelastic Substrates. *Proc. Natl. Acad. Sci. U. S. A.* **2018**, *115* (12), E2686–E2695. https://doi.org/10.1073/pnas.1716620115.

(284) Elosegui-Artola, A.; Oria, R.; Chen, Y.; Kosmalska, A.; Pérez-González, C.; Castro, N.; Zhu, C.; Trepat, X.; Roca-Cusachs, P. Mechanical Regulation of a Molecular Clutch Defines Force Transmission and Transduction in Response to Matrix Rigidity. *Nat. Cell Biol.* **2016**, *18* (5), 540–548. https://doi.org/10.1038/ncb3336.

(285) Trappmann, B.; Gautrot, J. E.; Connelly, J. T.; Strange, D. G. T.; Li, Y.; Oyen, M. L.; Cohen Stuart, M. A.; Boehm, H.; Li, B.; Vogel, V.; Spatz, J. P.; Watt, F. M.; Huck, W. T. S. Extracellular-Matrix Tethering Regulates Stem-Cell Fate. *Nat. Mater.* **2012**, *11* (7), 642–649. https://doi.org/10.1038/nmat3339.

(286) DiMilla, P.; Stone, J.; Quinn, J.; Albelda, S.; Lauffenburger, D. Maximal Migration of Human Smooth Muscle Cells on Fibronectin and Type IV Collagen Occurs at an Intermediate Attachment Strength. *J. Cell Biol.* **1993**, *122* (3), 729–737. https://doi.org/10.1083/jcb.122.3.729.

(287) Shenoy, V. B.; Freund, L. B. Growth and Shape Stability of a Biological Membrane Adhesion Complex in the Diffusion-Mediated Regime. *Proc. Natl. Acad. Sci. U. S. A.* **2005**, *102* (9), 3213. https://doi.org/10.1073/pnas.0500368102.

(288) Cao, X.; Ban, E.; Baker, B. M.; Lin, Y.; Burdick, J. A.; Chen, C. S.; Shenoy, V. B. Multiscale Model Predicts Increasing Focal Adhesion Size with Decreasing Stiffness in Fibrous Matrices. *Proc. Natl. Acad. Sci.* **2017**, *114* (23), E4549. https://doi.org/10.1073/pnas.1620486114.

(289) Miron-Mendoza, M.; Seemann, J.; Grinnell, F. The Differential Regulation of Cell Motile Activity through Matrix Stiffness and Porosity in Three Dimensional Collagen Matrices. *Biomaterials* **2010**, *31* (25), 6425–6435. https://doi.org/10.1016/j.biomaterials.2010.04.064.

(290) Erk, K. A.; Henderson, K. J.; Shull, K. R. Strain Stiffening in Synthetic and Biopolymer Networks. *Biomacromolecules* **2010**, *11* (5), 1358–1363. https://doi.org/10.1021/bm100136y.

(291) Grolman, J. M.; Weinand, P.; Mooney, D. J. Extracellular Matrix Plasticity as a Driver of Cell Spreading. *Proc. Natl. Acad. Sci.* **2020**, *117* (42), 25999. https://doi.org/10.1073/pnas.2008801117.